Slow Light in a SPS Photorefractive Crystal

Nacera Bouldja

NNT : **2020CSUP0005**

CentraleSupélec

Ecole Doctorale C2MP

« Chimie Mécanique. Matériaux Physique » - n° 606

Laboratoire Matériaux, Optique, Photonique et Système LMOPS EA-4423
Chaire Photonique

THÈSE DE DOCTORAT

Spécialité de doctorat : Physique

Soutenue le 03 décembre 2020

par :

Nacera Bouldja

Ralentissement de la lumière dans un cristal photoréfractif SPS

Composition du jury :

Directeur de thèse :	Delphine Wolfersberger	Professeur (CentraleSupélec)
Co-directeur de thèse :	Marc Sciamanna	Professeur (CentraleSupélec)
Président du jury :	Prénom NOM	Fonction (et lieu d'exercice)
Rapporteurs :	Cornelia Denz	Professeur (Institut für Angewandte Physik Westfälische Wilhelms)
	Stefania Residori	Directrice de recherche (Institut de Physique de Nice CNRS)
Examinateurs :	Luc Thevenaz	Professeur (EPFL, SCI-STI-LT)

CentraleSupélec

C2MP

Slow light in a SPS photorefractive crystal

CentraleSupélec

Ecole Doctorale C2MP

Chimie Mécanique Matériaux Physique

Chaire Photonique

Laboratoire MOPS

Matériaux Optique Photonique et Systèmes

Philosophiæ Doctor Thesis

Specialisation : Physics

Nacera Bouldja

Jury members

Ph. D. supervisor:	Pr. Dr. Delphine Wolfersberger	CentraleSupélec
Ph. D. co-supervisor:	Pr. Dr. Marc Sciamanna	CentraleSupélec
Rapporteur:	Pr. Dr. Cornelia Denz	Institut für Angewandte Physik Westfälische Wilhelms
Rapporteur:	Director of research CNRS. Stefania Residori	Institut de Physique de Nice CNRS
Examiner:	Pr. Dr. Luc Thevenaz	EPFL, SCI-STI-LT

defended the : 03/12/2020

Acknowledgements

Should I describe my thesis I would say that it looks like a train journey. It is a journey that is sometimes full of joy and hope, but also of difficult moments and obstacles that one may meet along the way. On this train, I boarded with people I didn't necessarily know but who made me feel that I am not alone during this journey. So, I would like to thank all these people who boarded this train, who have accompanied and supported me along these three years.

This thesis work was realized at the LMOPS Laboratory, inside the Photonics Chair and under the supervision of Mrs. Delphine Wolfersberger and Mr. Marc Sciamanna, Professors at CentraleSupelec. They find here my sincere gratitude for their implications, their sense of responsibility and their seriousness. I would particularly like to thank them because they are always shown to be attentive and very available throughout the realization of this work, as well as for the inspiration, the help and the time they devoted to me and especially to have granted me all their confidence. I also thank them for the courage that they gave me through their words and the joy they offered me for my daughter.

I would like to thank all the members of the jury who agreed to report and review my thesis work. Thank you to the thesis reviewers: Mrs. Cornelia DENZ, Professor of Physics at the Institut für Angewandte Physik Westfälische Wilhelms-Universität Münster Corrensstr, Germany and Mrs. Stefania Residori, Research Director at the Institut de Physique de Nice CNRS, France. Thank you to the examiner Mr. Luc Thevenaz, Professor and Head of the Fiber Optics Group at EPFL, SCI-STI-LT in Switzerland.

I thank my father, my mother, my grandmother, my sister, my brothers, and all the members of my family for the love and all the beautiful things they have given me throughout my life, my studies and my PhD and without whom all this would not have been possible. I thank my husband for his patience and encouragement which has been a great help to me. Thanks to Ilina, my daughter, the light of my life. I thank you and I am sorry if sometimes I couldn't find time to spend more time with you.

Finally, I would like to thank all those who have contributed, in one way or another, to the realization of this work. A very big thank you to all the researchers, PhD students, post-docs and colleagues and all the staff with whom I have had a great time inside and outside the laboratory.

Abstract

Slow light is the science domain that focuses on the physical nonlinear processes that can reduce the group velocity of a light pulse as it propagates in the medium. This discovery has been a great deal of recent interest for a wide range of applications such as optical buffering, nonlinear photonics and various types of spectroscopic.

The slow light performance is typically measured through two key parameters: the value of the delay or the group delay and the bandwidth of the output light pulse. This last one is generally defined by the so-called fractional delay, which is the ratio between the optical delay and the width of the output pulse. It is important to know that the optical telecommunication needs a slow light system that is able to slowdown short input light pulses with therefore a large value of the fractional delay (FD).

In the last years, numerous studies of slow light have been performed in several dispersive materials at different wavelengths. In 1999, group velocities smaller than 17 m/s [1] have been experimentally measured by Hau et al. in an ultra-cold gas using Electromagnetically Induced Transparency. More recently, the deceleration of the light pulses has been also successfully observed in solid-state materials such as in optical fibers [2] and in photonic crystals [3]. On the other hand, several studies have shown that photorefractive (PR) crystals can also be used to reduce the light propagation velocity at room temperature. As a matter of fact, the smallest group velocity of 0.025 cm/s has been achieved using the recording of refractive index gratings in a $BaTiO_3$ photorefractive crystal [4]. This method consists of the coupling of a continuous pump beam and a probe signal to increase the refractive index dispersion and leads the generation of a photorefractive gain. However, this small group velocity is often accompanied by the output pulse distortion which reduces the value of the fractional delay (FD of the order of 0.4 in [4]).

This thesis focuses on the study of the methods which allow in addition to the deceleration group velocity, the limitation of the distortion of the pulse in a photorefractive (PR) media. First, using the two-wave mixing (TWM) method, the PR crystal with a response time of 10 ms can slow down bright or dark pulses with duration of the order of ms. It is shown that the value of the time delay and the width of the transmitted pulse can be controlled by the photorefractive gain and the input pulse duration. By improving the TWM setup, we measure a fractional delay of 0.79 and 1 respectively, for the bright and the dark pulses with a duration close to the response time of the crystal. The beam fanning in a PR

crystal has also been used to slow down a single light pulse. The coupling between the beam fanning and the input beam leads both to the modulation of the noisy refractive index gratings and to the slowing down of the output pulse. The use of beam fanning for light slow down is new and significantly simplifies the slow light setup.

Slow light with the TWM and the beam fanning can be observed for long pulses, typically for a pulse of the order of the milliseconds and the seconds. In other words, only pulses with durations around the crystal response time are slowed down. In this thesis, we show for the first time that the use of the TWM at the nanosecond regime and a high laser intensity can reduce the photorefractive response time of the crystal and the slowdown of a shorter pulse (with a width of ns). The results achieved in a PR crystal with a thickness of 1 cm are similar to those achieved in slow light systems using a km-long optical fiber and for the same pulse durations.

Résumé

La lumière lente est le domaine scientifique qui s'intéresse aux processus non linéaires qui peuvent réduire la vitesse du groupe d'une impulsion lumineuse lorsqu'elle se propage dans un milieu. Cette technologie a récemment suscité un grand intérêt pour ses larges domaines d'application tels que le router optique, la photonique non linéaire et la spectroscopie.

L'efficacité des systèmes à lumière lente est généralement mesurée par deux paramètres clés : le retard ou la vitesse du groupe et la bande passante de l'impulsion lumineuse de sortie. Ce dernier est défini par le retard dit fractionnel qui est le rapport entre le retard et la largeur de l'impulsion de sortie. Un système de lumière lente dit efficace lorsqu'il est capable de ralentir les courtes impulsions lumineuses, tout en maintenant une valeur importante du retard fractionnel (FD).

Au cours des dernières années, de nombreuses études du ralentissement de la lumière ont été réalisées dans plusieurs matériaux dispersifs à différentes longueurs d'onde. En fait, des vitesses de groupe inférieures à 17 m/s[1] ont été mesurées expérimentalement par Hau et al. dans un gaz atomique en utilisant la Transparence Induite Electromagnétiquement. Plus récemment, la décélération de la vitesse de groupe a été également observée avec succès dans des matériaux à l'état solide tels que les fibres optiques [2], les cristaux photoniques [3]. D'autre part, plusieurs études ont montré que les cristaux photoréfractifs peuvent également réduire la vitesse de propagation de la lumière à température ambiante. En effet, la plus petite vitesse du groupe de $0,025$ cm/s a été obtenue en utilisant l'enregistrement des réseaux d'indice de réfraction dans le cristal photoréfractif $BaTiO_3$[4]. Cette méthode consiste à coupler un faisceau pompe continu et une sonde pour augmenter la dispersion de l'indice de réfraction et générer un gain photoréfractif ainsi le ralentissement de la sonde à la sortie du cristal. Cependant, cette petite vitesse est souvent accompagnée d'une distorsion de l'impulsion de sortie, ce qui réduit la valeur du retard fractionnel (par exemple, un FD de l'ordre de $0,4$ a été mesuré dans [4]).

Cette thèse porte sur l'étude de différentes méthodes qui permettent, en plus du ralentissement de la lumière, de limiter la distorsion de l'impulsion dans les milieux photoréfractifs. Tout d'abord, en utilisant la méthode TWM, le cristal SPS avec un temps de réponse de 10 ms peut ralentir les impulsions lumineuses ou sombres de l'ordre de ms. Il est démontré que la valeur du retard et la largeur de l'impulsion transmise peuvent être contrôlées par le gain photoréfractif et la durée de l'impulsion d'entrée. En améliorant la configuration

du TWM, nous mesurons un retard fractionnaire de $0,79$ et 1 respectivement pour les impulsions lumineuses et sombres de durées proches du temps de réponse du cristal. Le coma photoréfractive ou le « beam fanning » a également été utilisé pour ralentir la lumière dans le cristal photoréfractif. Le couplage du fanning avec l'impulsion d'entrée entraîne à la fois la modulation des réseaux d'indice de réfraction et le ralentissement de l'impulsion de sortie à différentes longueurs d'onde.

La lumière lente avec le TWM et le fanning peut être observée pour des impulsions longues, typiquement pour des impulsions de l'ordre de la ms à la seconde. En d'autres termes, seules les impulsions dont les durées sont proches du temps de réponse du cristal qui sont ralenties. Dans cette thèse, nous montrons pour la première fois que l'utilisation du TWM en régime impulsionnel et un laser à haute intensité peut réduire le temps de réponse photoréfractif du cristal et le ralentissement d'une impulsion plus courte (d'une largeur de ns). Les résultats obtenus dans un cristal PR d'épaisseur 1 cm sont comparables à ceux réalisés dans un 1 km de fibre optique pour les mêmes durées d'impulsions.

Contents

List of Figures

1

General introduction

Slow light is an interesting phenomenon that refers to the propagation of a modulated signal (e.g. pulse) through a medium with a very low group velocity v_g, smaller than the celerity of light in the vacuum ($v_g \ll c$). The deceleration of this velocity is usually achieved by nonlinear interactions between the light pulse and the matter that induce a strong material (refractive index) dispersion. Therefore, the light pulse will be delayed during its propagation through the material with strong dispersion. The basic principle behind the slow light method is illustrated in figure 1.1. The group delay is the time it takes for a pulse to pass through the material, which is given by $\Delta\tau = L/v_g$, where L is the length of the medium. For the experimental characterizations, it is defined as the shift in time between the output pulse and the reference (input pulse) maximums.

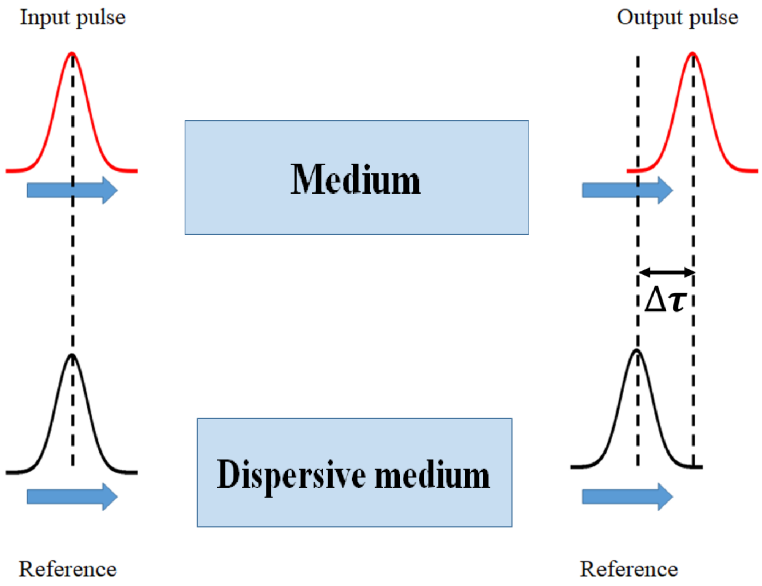

Figure 1.1: Slow light propagation in a dispersion medium, $\Delta\tau$ is the group delay.

Since the last decade, the deceleration of the light is a popular research field in photonics and nonlinear optics, especially with the development of new techniques to control the effective group velocity of laser pulses in an optical medium. Besides its fundamental interest, slow light is thought to find applications in future optical communication systems, such as, for example, the control of optical delay lines, optical buffering, optical storage and memories, data synchronization, high sensitivity interferometry, and signal processing.

The field of slow light emerged when a group of Steve Harris at Stanford University demonstrated that the so-called Induced Electromagnetic Transparency (IET) effect [5, 6]

can reduce drastically the propagation speed of a light pulse in an atomic vapor much below the speed of light in vacuum. The principle of IET consists of generating a narrow transparency window in an absorption profile that induces a rapid variation of the refractive index and therefore a very low group velocity of the light. Thereafter, the experiments of Hau, Harris et al (1999) showed that the speed of light could be reduced to 17 m/s [1] in ultracold atom. Other processes have been proposed in order to slow down the velocity of light operating at room temperature and in solid-state materials, which are more suited for telecommunication applications. Light deceleration has been demonstrated in optical fibers using optical parametric amplification (OPA) [7]. Using the Brillouin scattering in optical fibers [2], they have shown the slowdown of 40 ns width light pulse with a group delay up to 150 ns. One year later, B. Sturman et al. [4] showed theoretically and experimentally that the coupling of two photorefractive waves can slow down the speed of light pulses to a value of 0.025 cm/s in a $BaTiO_3$ crystal and 40 cm/s in a $Sn_2P_2S_6$ crystal. The slowdown of the light pulses using the wave mixing has been studied in many other materials such as in liquid crystals (LCLV) [8] and SBN crystal [9]. Subsequently, other studies were investigated to slow down light pulses by four-wave mixing [10]. In that case, both the signal and its conjugated beam will be delayed at the output of the crystal.

To study the efficiency of a slow light system, two parameters should be taken into account: the group delay and the bandwidth of the transmitted pulse. These parameters can be combined to etermine the fractional delay (that is, the ratio between the optical delay and the output pulse duration). On the other hand, applications such as optical telecommunications require slow light systems that are able to slow down short input light pulses while maintaining a small group velocity and a large fractional delay (FD). Unfortunately, the material dispersion that leads to a reduction of the group velocity also significantly broadens the output pulse, hence, limiting the FD value.

This thesis focuses on the slow light process induced in photorefractive Tin Hypothiodiphosphate ($Sn_2P_2S_6$, SPS) crystals at room temperature. Compared to other systems such as optical fibers, these crystals offer the possibility to generate very important optical delays over a large range of wavelengths, from the visible to the infrared. The objective of this thesis focuses on the use of such photorefractive crystals to allow both slowing down short pulses and realizing a large fractional delay. In this work, we perform both analytical and experimental studies of delay and fractional delay undergone by a pulse

propagating in a photorefractive crystal. Most importantly, we use different nonlinear methods to slow down pulses of different durations and we analyze the performances of the slow light as a function of several experimental parameters: propagation length, coupling force (photorefractive gain), crystal response time, type and duration of the input pulse.

Outline

This thesis has been organized into five chapters. We will present in the first chapter, the physical notions of optical pulse propagation in a medium. In particular, we will discuss the group velocity and how we can control its value at the output of the material. We will introduce the performances of slow light by defining specific parameters such as the optical delay and the fractional delay. We will then present the physical phenomena and media used to slowdown an optical pulse. Then, we will discuss some application domains of slow light such as telecommunication, spectroscopy, and nonlinear optics. Based on the limitations of the systems already developed, we will give the objectives and motivations behind the use of a photorefractive crystal to slow down the light pulse. At the end of the chapter, we will present a state of the art on the photorefractive effect, and its fields of application, and the characteristics of the crystals used in this thesis.

In the second chapter, we will present the work of the slowdown of Gaussian light pulses achieved with the two-wave mixing process (TWM) in a photorefractive crystal at room temperature. We will discuss the state of the art and the results obtained with this method in different crystals. The analytical model allowing to deduce the optical delay and the output pulse duration will be presented in detail. In the second part of the chapter, we will experimentally study the dependence of slow light performances on the TWM gain and the input pulse duration and we will give the best performances obtained in terms of the group velocity, and fractional delay.

In the third chapter, we will propose a study of the slowing down of dark pulses in the photorefractive crystal using the TWM process. First, the numerical results of the delay will be presented and analyzed. Then, we will present the experimental results and the parameters allowing to have a delay larger than the duration of the dark input pulses. Finally, the performances obtained in this chapter will be compared to those achieved with bright pulses.

The fourth chapter will focus on another photorefractive slow light system at room temperature. We will study the photorefractive beam fanning and its ability to slowdown

a single light pulse at both visible and infrared wavelengths. The theoretical results will show that the slow light performances depend on the fanning intensity or the depletion of the input beam. Next, the experimental results will be discussed in terms of the strength of the fanning, the input pulse duration and the wavelength. Then some results of the fast light using the beam fanning will be presented at the end of the chapter.

The deceleration of nanosecond pulse studies in the SPS crystal will be presented in the last chapter. At the beginning of the chapter, we will give the conditions that allow the slowdown of shorter pulses in the photorefractive crystal. Then, we will describe for the first time the experimental method used in these studies. At the end of the chapter, we will discuss and analyze the results as a function of the input parameters.

Finally, we will give the conclusions and perspectives of this work.

Publications and proceedings

This thesis has been the subject of scientific publications and various international conference proceedings listed below:

N. Bouldja, M. Sciamanna, and D. Wolfersberger, "Ultraslow Light Pulse in a SPS Photorefractive Crystal at Room Temperature," 2018 European Conference on Optical Communication (ieeexplore.ieee.org 2018);*https* : *//doi.org*/10.1109/*ECOC*.2018.8535306[11]

N. Bouldja, M. Sciamanna, and D. Wolfersberger,"Improved slow light performances using photorefractive two-wave mixing," Opt. Lett. 44, 1496-1499 (2019); *https* : *//doi.org*/10.1364/*OL*.44.001496 [12]

N. Bouldja, M. Sciamanna, and D. Wolfersberger,"Slow light using photorefractive beam fanning," 2019 Conference on Lasers and Electro-Optics Europe and European Quantum Electronics Conference, OSA Technical Digest (Optical Society of America, 2019)[13]

N. Bouldja, M. Sciamanna, and D. Wolfersberger," Slow light with photorefractive beam fanning," Opt.Express,28,5860-5865 (2020) *https* : *//doi.org*/10.1364/*OE*.386254[14].

Nacera Bouldja, Marc Sciamanna, and Delphine Wolfersberger, "Slow light using photorefractive nonlinear optics," Proc. SPIE 11358, Nonlinear Optics and its Applications 2020, 113580I (2020); *https* : *//doi.org*/10.1117/12.2559258[15]

Nacera Bouldja, Alexander Grabar, Marc Sciamanna, and Delphine Wolfersberger,"Slow light of dark pulses in a photorefractive crystal,"Phys. Rev. Research 2, 032022(R) (2020); *https* : *//doi.org*/10.1103/*PhysRevResearch*.2.032022[16]

Conferences

-44th European Conference on Optical Communication (ECOC), 23-27, September, 2018, Rome, Italy.

-CLEO/Europe-EQEC 2019, 23 – 27 June 2019, Munich, Germany.

-PR'19, Photorefractive Photonics and beyond, 18-21 june 2019, Gérardmer, France.

-SPIE Photonics Europe, 29/March - 2 April 2020, Strasbourg, France.

2

How to control the light velocity in a photorefractive nonlinear material?

Faster is not always better, as the fable of the hare and the tortoise demonstrates. The same is true in photonics, where slow light can outperform fast light in many aspects.

Contents

This chapter reviews the methods of slowing down of light pulses and the nonlinear photorefractive effect. First, we will shortly introduce more specific notions of propagation velocity (phase and group velocities) of an optical wave. We will then present in a very general way how to control the group velocity of a light pulse propagating in dispersive mediums. Some early physical processes used to reduce the speed of a light pulse in different materials will be presented. We will give some application fields and the limitations of the slow light systems. Then the objective of our thesis will be presented. Finally, we will describe the photorefractive effect that we have used to slow light.

2.1 Propagation of a light pulse

Before discussing the different phenomena inducing slow light in a dispersive medium [17], especially in photorefractive materials, we explain the difference between the phase velocity and the group velocity of a light pulse propagating in a medium (figure 2.1). We consider a monochromatic wave at angular frequency ω propagating in the z-direction through a medium with refractive index n. The complex electric field is given as:

$$E(z,t) = E_0 exp(ik_0 z - i\omega t) \tag{2.1}$$

where E_0 is the electric field amplitude, k_0 is the wave number and t is the time. The electric field E is characterized by a phase $\Phi(z,t) = kz - \omega t$ and a phase front defined by a plane on which the phase is constant, $\Phi(z,t) = \Phi_0$.

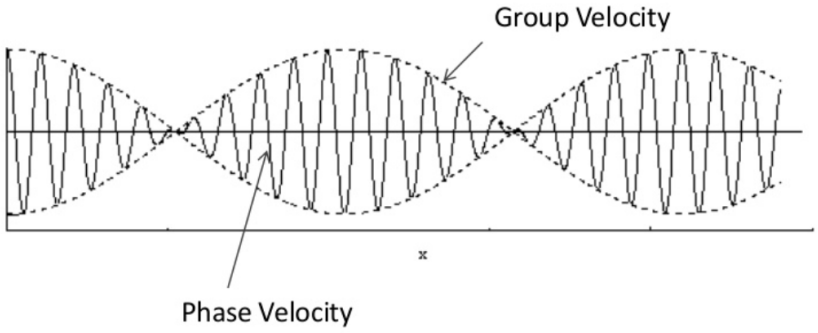

Figure 2.1: Difference between the phase velocity and the group velocity of a light pulse propagating in a medium.

2.1.1 Phase velocity

The phase velocity v_p is the speed with which the phase fronts of a monochromatic propagating wave propagate in a medium. The phase velocity is defined by the relationship [18]:

$$v_p = \frac{dz}{dt} = \frac{\omega}{k(\omega)} = \frac{\omega}{n(\omega)k_0} = \frac{c}{n(\omega)} \tag{2.2}$$

with c is the vacuum velocity, k_0 and $n(\omega)$ are respectively the wave number and the refractive index of the medium at angular frequency ω.

2.1.2 Group velocity

Slowing down or accelerating light requires the control of the group velocity v_p at which the light pulse peak moves through a dispersive material. The concept of this velocity was first enunciated by Hamilton in 1839 (published in 1841) [19]. Consider a pulse propagating in the z-direction, the complex electric field at $z = 0$ is given by:

$$E(z = 0, t) = E_0 exp(-i\omega_0 t) \tag{2.3}$$

where E_0 and ω_0 are respectively the envelope and frequency of the pulse. In the case of a pulse whose spectrum has a width around the central frequency $\omega_0/2\pi$, the group velocity is then defined by the equation:

$$v_g = \left(\frac{d\omega}{dk}\right)_{\omega_0} = \frac{c}{n_g} \tag{2.4}$$

Here, n_g is the group index that depends on the phase refractive index and the dispersion characteristic of the medium $dn/d\omega$:

$$n_g = n + \omega\frac{dn}{d\omega} \tag{2.5}$$

2.2 How to slow light in dispersive material?

Slow light is a physical effect where the light pulse propagates in a medium with a lower group velocity than the velocity in the vacuum ($v_g << c$). According to Gehring et al. [20], the group delay is often the parameter used to measure slow light performance for telecommunication applications. However, in order to provide a more complete analysis, the delay time measurement is often combined with a measurement of the bandwidth or the bit rate of the transmitted pulse.

From equations. 2.4 and 2.5, we note that to reduce the light pulse propagation velocity, it is sufficient to increase either the phase refractive index n or the dispersion of the medium $dn/d\omega$. Therefore, a solution for obtaining a delay in the transmitted pulse is to find physical processes that provide spectral resonance in the material. This resonance causes a rapid change in the refractive group index that can be induced by a gain or absorption resonance, as required by the Kramers-Kronig relations. This situation is graphically illustrated in figure 2.2.

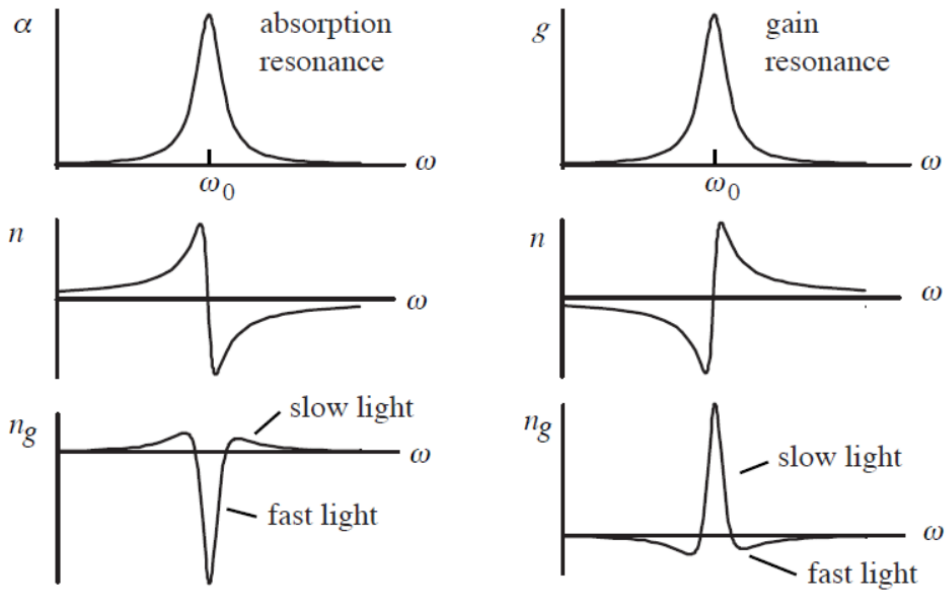

Figure 2.2: Relationship between absorption resonance (a) or gain resonance (b) and refractive index using Kramers-Kronig relations, extracted from [21]. A strong dispersion around the gain peak induces a slowing down of the light, according to the reference [17].

For characterizing slow light performances, it is important to measure the optical delay and the fractional delay defined below.

2.2.1 Optical delay

The group velocity v_g characterizes the distance dl performed in a given time dt. Thus, the time dt is given by the following relation:

$$dt = \frac{dl}{v_g} = \frac{n_g dl}{c} \tag{2.6}$$

The group delay taken by a light pulse to travel the distance L between points A and B is then given by:

$$\Delta\tau = \int_A^B \frac{n_g}{c} dl = \frac{n_g L}{c} = \frac{L}{v_g} \tag{2.7}$$

The time delay τ_s experienced upon propagation through the material without any dispersion phenomenon is given by:

$$\tau_s = \frac{Ln}{c} \tag{2.8}$$

So the material contribution to the group delay τ_d is:

$$\tau_d = \Delta\tau - \tau_s = \frac{L}{v_g} - \frac{Ln}{c} = \frac{n_g L}{c} - \frac{n}{c} \tag{2.9}$$

Equation. (2.9) shows that the delay value is controlled by the group index value n_g and by the propagation distance L. There are several ways to measure this group delay. For single pulses, the method is to simply measure the time delay between the maximum of the optical signal and the reference as shown in figure (2.3).

2.2.2 Fractional delay

When we observe the slowing down of a pulse in a dispersive material, it broadens and deforms the pulse, hence the interest of the measurement of the bandwidth of the output light pulse. In other terms, to give a more accurate representation of slow light performances, it is important to measure both the delay and duration of the transmitted pulse. The ratio between $\Delta\tau$ and the output pulse full width at half-maximum (FWHM) t_1 determines the fractional delay FD which is a practical figure of merit for optical delay

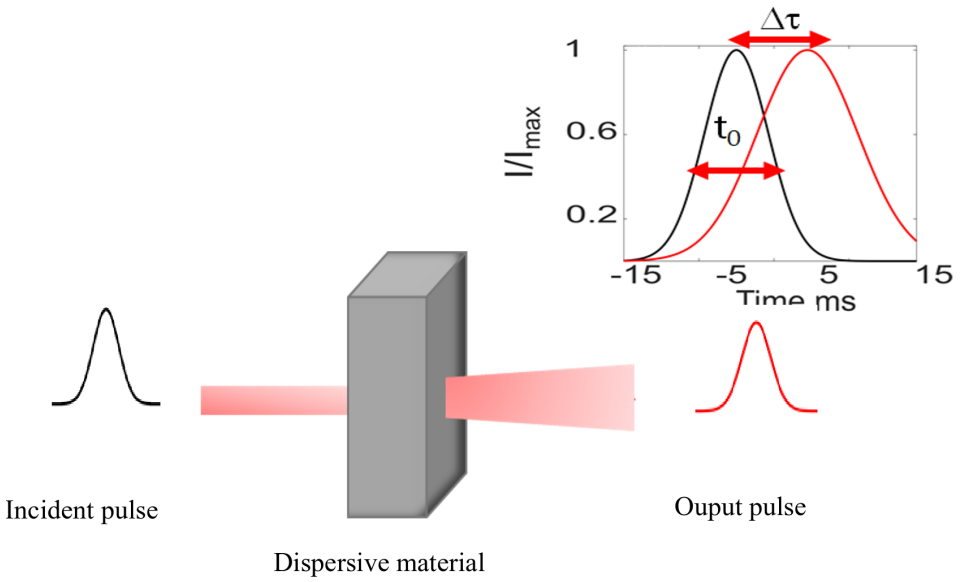

Figure 2.3: Experimental delay time measurement between the input (black line) and output (red line) pulses. $\Delta\tau$ is the delay time, t_0 is defined as the full input pulse width at half maximum.

line applications:

$$FD = \frac{\Delta\tau}{t_1} \tag{2.10}$$

The fractional delay is limited by the group velocity dispersion and the spectral reshaping or the distortion of the incident pulse due to the frequency dependence of the absorption coefficient of the material [22].

As now we know how to characterize the slow light process. Let us review the different technologies used in the literature.

2.3 Slow light technologies

In general, there are two standard approaches for slowing down the group velocity of light. The first makes use of the dispersive properties associated with the resonance structure of a material medium. The second makes use of structural resonances, such as those that occur in photonic crystals [23]. two standard methods for controlling the group velocity of light. One makes use of the dispersive properties associated with the resonance structure of a material medium. The other makes use of structural resonances, such as those that occur in photonic crystals.

Since the first experimental demonstration of slow light using Electromagnetically Induced Transparency in an ultra-cold atomic gas [1], other methods are performed to slow down the light group velocity in solid-state materials at room temperature, which are more suited for many practical applications. Those include photonic crystal [24–26], coherent population oscillation [27], stimulated Brillouin [28], and Raman [29] scattering in optical fiber.

2.3.1 Slow light in atomic vapors

Slow light experiments in atomic vapors using EIT (Electromagnetically Induced Transparency) process have initiated and motivated slow light research. The EIT process generates a narrow window of transparency in an absorption profile in a medium [30]. The resulting window of transparency induces a dispersion responsible for the sow light effect in atomic vapors [31], in solid crystals [32], and in optical fibers [33]. In 1999 [1], Hau et al. proposed this technique to studying slow light in atomic vapor. There, the experiment is performed with a gas of sodium atoms cooled by laser and evaporative cooling. At Nano Kelvin temperatures near that of the transition to a Bose-Einstein condensation, they demonstrate pulse propagation velocity slowed down to 17 m/s. However, the potential for practical application of the EIT is limited because the experiment requires hard conditions and does not occur at room temperature. It is also worth noting that the pulse being delayed is μs long, which is still much longer than typical pulses used in telecommunications.

2.3.2 Slow light in photonic crystal

More recently, the slow light has also been demonstrated in medium with a spectral transmission bandgap. Such bandgap can be artificially created in structures with periodic patterns, such as Bragg gratings, coupled resonators, or photonic crystals [24]. In the case of photonic crystals, the deceleration of light results from constructive interference between reflected and transmitted waves in a highly dispersive medium. The small shift in the phase between these waves creates a wave whose envelope propagates slowly. The periodic photonic structures have a number of advantages compared to the other mechanisms. Those are able to generate significant delays of arbitrary wavelength. Many slow light experiments have been performed in a simple [34] or dynamic [35, 36] photonic crystal coupled waveguide and in 25 m high nonlinearity photonic crystal fiber [37]. On the

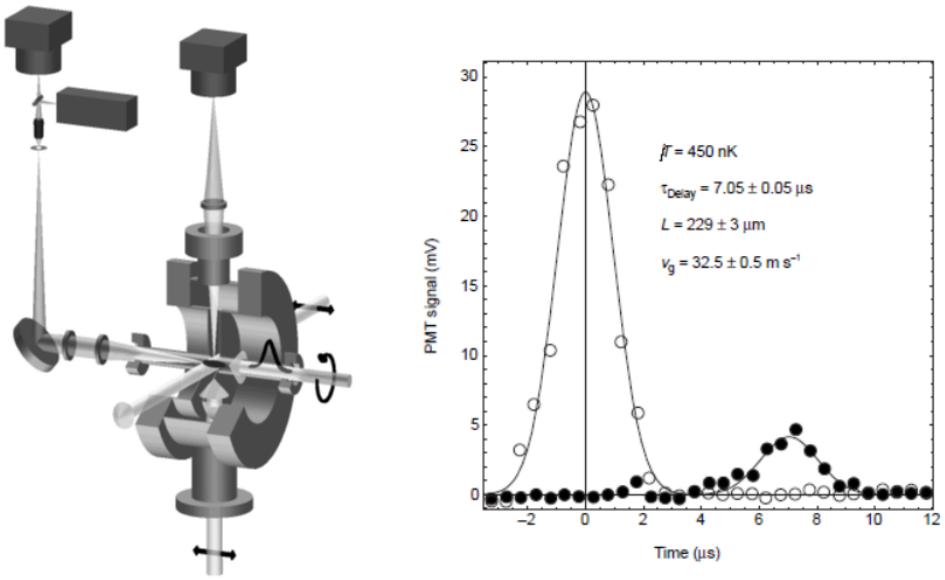

Figure 2.4: Experimental set-up and experimental result of slow light in atomic vapor. A light pulse is delayed by 7.05 μs in a 229-mm-long atom cloud [1], corresponding to $v_g = 32.5\ m/s$.

other hand, photonic crystals have allowed achieving a large bandwidth [38] and better fractional delays [3]. For example, Baba et al. [3] measured, to the best of our knowledge, the highest value of fractional delay in the order of 57. Using the modulation phase-shift method, they demonstrate that the delay can vary with the wavelengths. As shown in figure 2.5, for $\lambda = 1.547$ to $1.548\ \mu m$, the delay increases from 10 to 40 ps. In that case, the group index increase from 10 to 60 and the group velocity varies from 30000 km/s to 5000 km/s.

2.3.3 Slow light in optical fiber

Several approaches have been proposed to reduce the light group velocity directly in optical fiber [39, 40], for its potential application in optical buffering and optical signal processing. Slowdown of light pulses was first demonstrated using stimulated Brillouin scattering (SBS) by Song et al. [41] and Okawachi et al [2]. This method takes place when a counterpropagating pump and probe beams with angular frequencies ω_p and ω_s respectively interact through their mutual interaction with a longitudinal acoustic wave with frequency Ω [42]. When both the energy and momentum are conserved, the acoustic wave causes a modulation of the refracted index, which results in the amplification and

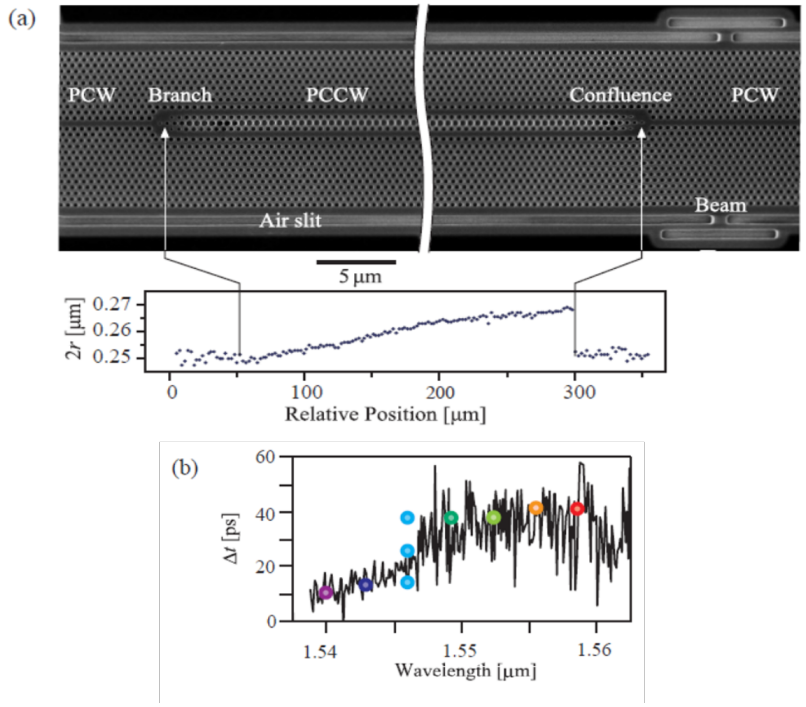

Figure 2.5: (a) Chirped photonic crystal coupled waveguide (PCCW).(b) Delay measured using the modulation phase shift method at different wavelengths [3] in a chirped PCCW. The delay values vary from 10 to 40 *ps*.

the deceleration of the probe beam. In [41], Song et al. delayed a 100 *ns* pulse by 30 *ns* and a 40 *ns* pulse by 150 *ns* in optical fiber and fiber grating respectively (figure 2.6). They also demonstrated that the delay performances are limited by the gain bandwidth. By increasing the gain bandwidth, it has been shown the possibility to slow down even shorter light pulses. For SBS slow light bandwidth of 12.6 GHz, a pulse duration of 75 *ps* is delayed by 47 *ps* [43].

Stimulated Raman scattering (SRS) has also been used to achieve tunable delays in optical fibers [7, 29]. This process arises when the pump beam induces lattice vibrations, as optical phonons which have very short lifetimes of the order of picoseconds. This has the effect of increasing the gain bandwidth and slowing down shorter pulses than in the case of Brillouin scattering. In 2005 Sharping et al. [29] delayed a 430 fs pulse by 85% of its pulse duration by using SRS process in a 1 km long optical fiber.

As will be presented in the next chapters, the so-called wave-mixing process can also be used to reduce the propagation velocity of a light pulse in the solid materials, particularly in photorefractive crystals. We will then give the performances and limitations reported

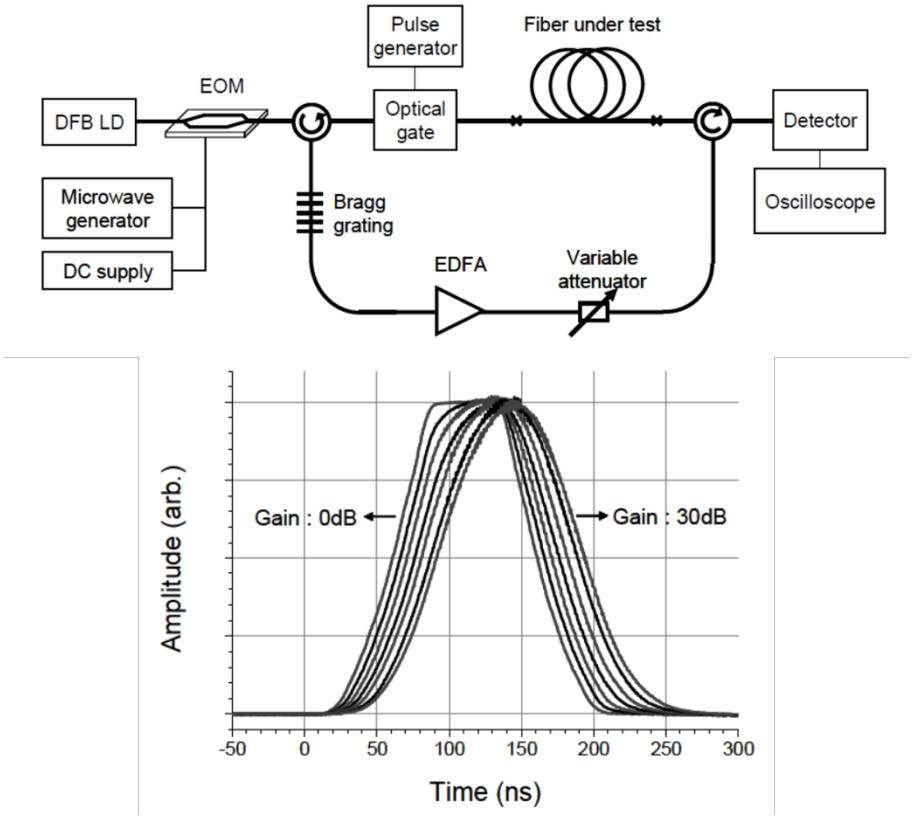

Figure 2.6: Slowdown of light pulses using stimulated Brillouin scattering. Output pulse delays for different Brillouin gains [41].

by previous slow light studies [4] in these photorefractive materials.

2.3.4 Applications of slow light

Since the last decade, slow light pulse propagation through a material has attracted great interest for its promise in several applications. It has recently been studied in a wide range of materials, such as optical fiber, photonic crystals, and other nonlinear materials for applications. It can greatly enhance the performance of optical buffers, nonlinear photonics, interferometry, laser radars, spectroscopic interferometers, and SLIDAR systems.

Optical telecommunications: Slow light has many potential applications in telecommunications, including controllable optical delay lines and optical buffers. This temporal control of the information can substantially improve the efficiency of optical transmission networks by performing all-optical routing. However, this functionality is currently provided via electronic signal processing involving costly and slow double optical-electronic conversion. The ambition of the researchers was to be able to replace them with a faster and more efficient all-optical version [44].

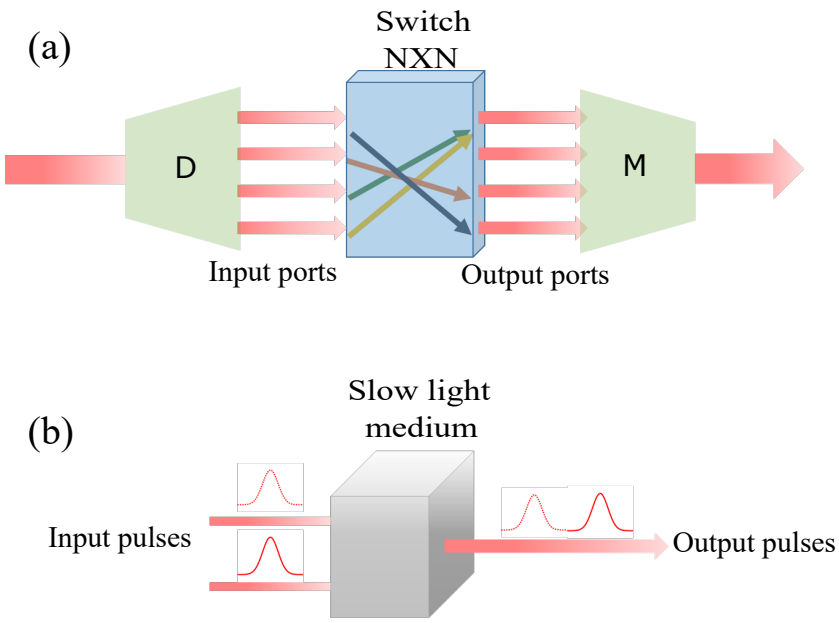

Figure 2.7: (a) An NxN optical switch, D and M are demultiplexer and multiplexer respectively. (b) An optical buffer based on slow light medium [45].

In principle, optical memories or buffers operate independently of the data rate and are therefore more efficient since the data remains in the optical domain. Optical buffering has emerged as key component for future optical communications. Figure 2.7 shows the layout of a basic optical buffer memory [46]. As shown in figure 2.7(a), if several data packets

arrive simultaneously at an optical switch, this one can not handle the same time the data packets which are intended for the same destination port. Optical buffering provides contention resolution and ensures low packet booking probability (figure 2.7(b)) [45].

Nonlinear optics: Slow light can be used for improving the light and matter interaction and the efficiency of the nonlinear process with lower power and smaller, cheaper lasers [47]. The zero- dispersion in photonic crystal waveguides is used to enhance the nonlinear self-phase modulation [48]. Indeed, the output pulse broadening induced by self-phase modulation was strongly enhanced for slower waveguides. In addition to the slow improvement in material non-linear loss, the slow light propagation in the waveguide allows the increase of the efficiency of the nonlinear third harmonic-generation (THR) [49]. As shown in figure 2.8, the output power of the green light obtained by THR is enhanced in a photonic crystal that operates in the slow light region.

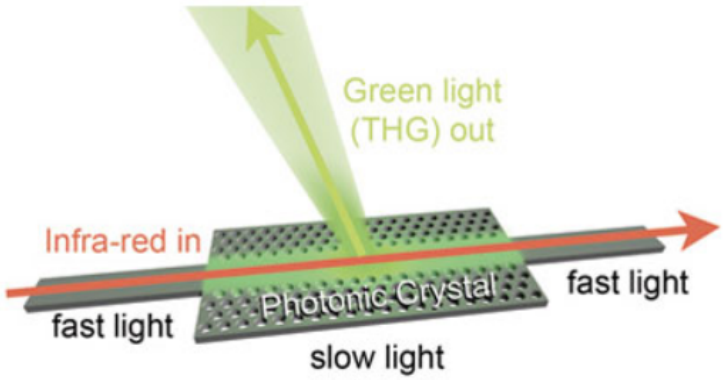

Figure 2.8: Enhancement of third-harmonic generation using slow-light in a photonic crystal [50]

Interferometry: Interferometers with high sensitivities are able to improve the performances of a wide range of applications, such as metrology [51], quantum information and optical sensing. This sensitivity can be greatly increased by introducing a slow light medium into the interferometer. Currently, a number of interferometers designs have been proposed [52–55]. It is shown that the spectral sensitivity is proportional to the group index n_g of the medium that is inside the interferometer [56]. By changing n_g, Shi et al. increased the sensitivity by a factor of 2 in an interferometer based on semiconductor materials. In other work, the sensitivity of a Fourier transform interferometer (figure 2.9) was improved by a factor equal to 100 [57].

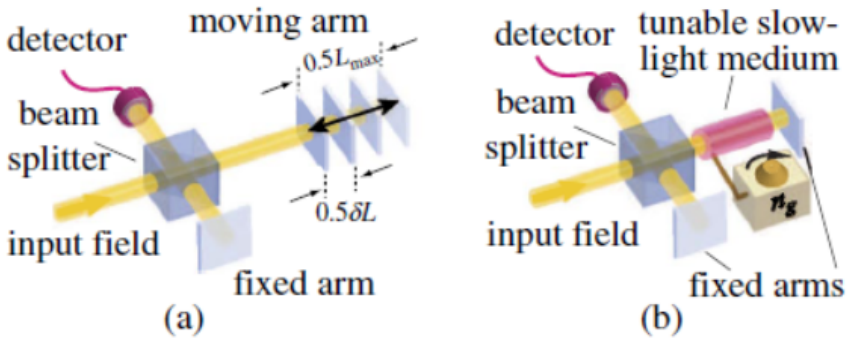

Figure 2.9: (a) Conventional Fourier Transform (FT) interferometer (b) a FT interferometer with a tunable slow-light medium [57].

2.3.5 Slow light limitations

Some applications such as telecommunications require a large fractional delay which defines the information storage capacity of the slow light system. In the major slow-light technologies, this storage capacity can be limited by short delay times or pulse distortion which is caused by the dispersion of the group velocity and the frequency-dependent absorption [1]. Indeed, the essential condition for creating slow light is the material's dispersion. The larger is the dispersion, the better is the light slowed down. If a light pulse is slowed down more than its duration, it broadens so much that it becomes useless. This fundamental limitation has dashed the hopes of being able to build optical routers.

Before presenting our objectives, we give in the following table the performances and the limitations of some slow light systems.

system	Propagation length	Input bandwidth or duration	Delay	Group velocity	FD
EIT in cold vapor [1, 58] at 45 nK	230 μm	300 kHz	10 μsm	17 m/s	2.1
photonic crystal at room temperature [3]	250 μm	1.4 THz	40 ps		57
SBS in fiber at room temperature [2]	1 km	63 ns	25 ns		0.4
Photorefractive crystal at room temperature [4]	2 mm	1.5 s	8 s	0.025 cm/s	0.4

2.4 Objective of the thesis

According to a recent publication [4], it appears that the best performance in terms of group velocity has been achieved through the two-wave mixing in photorefractive crystals. The velocity of a 1.6 s long pulse was slowed down to 0.025 m/s in a $BaTiO_3$ crystal at room temperature [4]. Even if this speed is very small, this system is unfortunately limited by two factors:

1) The result is obtained at a visible wavelength,

2) The delayed pulse duration which is very large of the order of one second and the pulse is significantly broadened which reduces the value of the fractional delay.

For future applications in telecommunications based on slow light systems, what is important is not only to slow down the light as much as possible but to slow it down while the output pulse short enough to keep a large transmission bit rate.

The motivations of our researches are driven by these ambitions: we plan to optimize slow light in photorefractive crystal while satisfying an important fractional delay or large bandwidth.

In this thesis, we propose to slow light in a photorefractive crystal at room temperature using different physical mechanisms. First, we study the parameters which can improve the slow light performances both at the visible and infrared wavelengths range using

continuous lasers, such as the PR gain, crystal doping, pulse profile, and duration. Then, a more intense pulsed laser will be used to demonstrate the deceleration of nanosecond pulses.

2.5 Physical concepts: Photorefractive effect and TWM

2.5.1 Definition and mechanisms

The photorefractive effect was discovered at Bell Laboratories in 1966 during a second harmonic generation experiment in an electro-optical crystal [59]. Initially discovered as optical damage in nonlinear crystals, it is now used and studied for several applications: the realization of holographic memories [60], phase conjugation [60, 61], and slowing down of light [4].

Figure 2.10 illustrates the principle of the photorefractive effect. The light excites charge carriers from donor levels located in the illuminated areas of the material. Under the influence of different mechanisms [62, 63] including diffusion, drift, and photovoltaic effect, these charge carriers will migrate into dark areas of the material leaving ionized donor levels in the illuminated areas. The migration of the charge carriers induces a non-uniform distribution and creates an electric field called a "space charge field". This field is shifted with respect to the initial illumination figure. The value of this phase shift depends on the competition between the different transport mechanisms mentioned above. By the end, it causes a local modification of the refractive index of the medium n through the linear electro-optic effect also called "Pockels effect". This effect is mathematically expressed as follows [64, 65]:

$$\Delta\left(\frac{1}{n^2}\right)_{ij} = \sum_k r_{ijk} E_k \tag{2.11}$$

where r_{ijk} [66] are the third-rank electro-optical tensor and E_k are the space-charge field components.

As all physical phenomena, the photorefractive effect has its own characteristics:

1. The photorefractive effect is sensitive to the received energy, which allows inducing index variations both with low-power continuous laser beams and with shorter, more powerful pulsed laser beams.

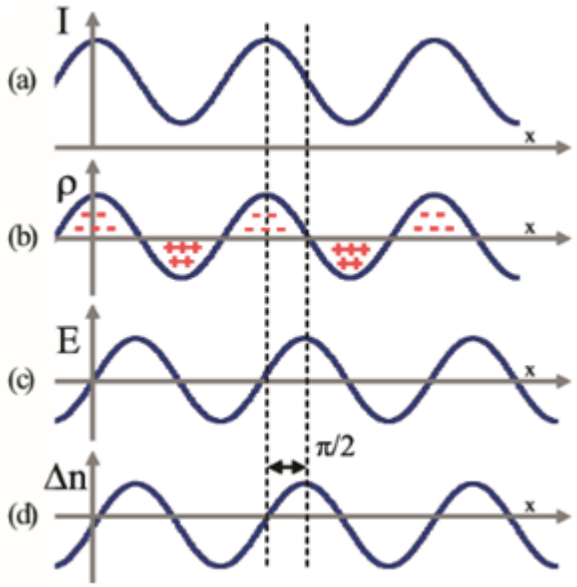

Figure 2.10: Mechanisms of the photorefractive effect (the x-axis represents the space coordinate that is perpendicular to the fringes). (a) Non-uniform illumination pattern resulting from the interference of two coherent laser beams. (b) Charge carrier distribution which is generated by photoconduction. (c) Space charge field modulation induced by charge migration and recombination. (d) Creation of a refractive index grating versus x through the electro-optic effect.

2. The time required to build the space-charge field (and thus the refractive index variation) depends on the efficiency of the charge transfer mechanism and the duration with which the optical energy is delivered. For example, after the propagation of a light pulse in the material, it takes a certain time for the index variation to build up, the time needed for the exciting charges to move significantly.

3. Photorefractive materials have a broadband sensitivity that extends from the visible to the infrared wavelengths.

4. Photorefractive crystals have a memory effect that can be eliminated using a uniform illumination, for example, a white light.

5. The phenomenon is totally reversible. Any local variation in the index is eliminated using a uniform illumination that redistributes the loads in the material. Thermal excitation also redistributes these loads uniformly, which also erases the refractive index variation. Heating the material can also accelerate this redistribution.

2.5.1.1 Band transport model

Proposed in 1979 by Kukhtarev et al. [67], the band transport model shown in figure 2.11 is the most common model used to describe the photorefractive effect. In this model, we consider that there is only one type of free charge carriers, for example, electrons arising from density donor centers N_D issued from crystalline impurities in the bandgap. Those donors are all at the same energy level in the bandgap of the material. Under illumination, these electrons are excited in the bright fringes areas to the conduction band and move via the transport mechanisms to the dark areas where they will be trapped by ionized donors of density N_D^+. The excitation of the neutral donor centers increases the density of ionized donors which in turn decreases due to their recombination with the electrons. This situation is expressed by the following equation [68]:

$$\frac{N_D^+}{\partial t} = (sI - \beta)\left(N_D - N_D^+\right) - \xi n_e N_D^+ \tag{2.12}$$

where s is the photo-excitation coefficient, I is the incident intensity, β is the thermal excitation coefficient, ξ is the electron recombination rate and n_e is the density of free electrons.

The migration of the charge carriers occurs due to different transport mechanisms that create a current density j in the materials [68]

$$j = e\mu n_e E + \mu k_B T \nabla n_e + \beta_{ph}\left(N_D - N_D^+\right) cI \tag{2.13}$$

- $e\mu n_e E$ represents the drift effect where e is the charge of the electrons, μ is the mobility of the charge carriers, n_e is the density of the electrons and E is the electric field.

- $\mu k_B T \nabla n_e$ describes the diffusion effect where k_B is the Boltzmann constant and T is the temperature.

- $\beta_{ph}\left(N_D - N_D^+\right) cI$ represents the photovoltaic effect where β_{ph} is the effective photovoltaic coefficient and c is the velocity of light in a vacuum.

The continuity of free electrons in photorefractive materials is given as a function of the

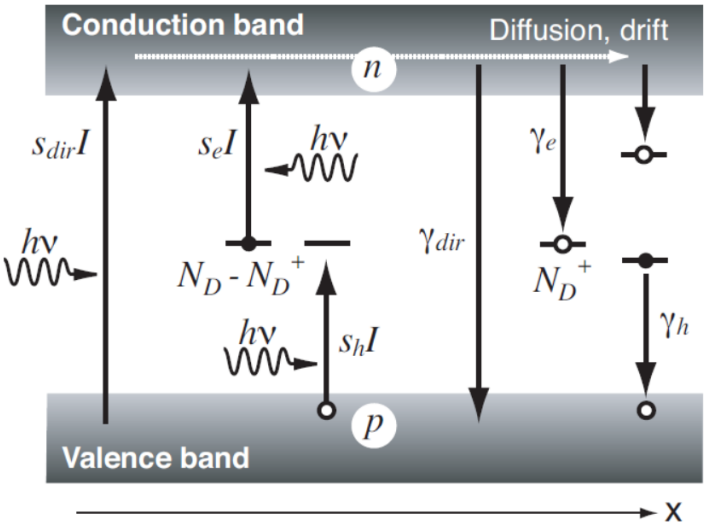

Figure 2.11: Mechanisms of the band transport model [68]

current densities of the ionized donors as follows:

$$\frac{\partial n_e}{\partial t} = \frac{divj}{e} + \frac{\partial N_D^+}{\partial t} \tag{2.14}$$

The Poisson equation describing the migration of electrons is given by:

$$div(D) = -e(n_e + N_A - N_D^+) \tag{2.15}$$

2.5.1.2 Refractive index gratings

The inhomogeneous illumination of a photorefractive crystal produces the local redistribution of charges and the generation of the space charge field. The sinusoidal intensity patterns $I(r)$ [68] due to the interference between two coherent laser beams with wave vectors k_p and k_s and amplitudes A_1 and A_2 respectively is given as:

$$I(r) = I_0\,(1 + m\ cosK_r) \tag{2.16}$$

where r is the position vector, I_0 is the average intensity given by equation (2.17) , $m = 2\frac{|A_1||A_2|}{|A_1|^2+|A_1|^2}$ is the modulation depth and $K_r = k_p - k_s$ is the grating vector. For a small modulation $m \ll 1$, the intensity distribution induces a periodic space charge field

E_{sc} which is always parallel to the grating vector $K_r = \frac{2\pi}{\Lambda}$:

$$I_0 = \frac{1}{2}\sqrt{\varepsilon_0/\mu_0}\left(|A_1|^2 + |A_2|^2\right) \tag{2.17}$$

Note that the response time of a PR crystal τ which is an important parameter for PR slow light systems is inversely proportional to I_0.

2.5.2 Photorefractive materials and applications

2.5.2.1 Photorefractive materials

There are three different families of photorefractive crystals and the research focused on there three well-defined categories [69, 70]: the ferroelectric [59], the sillenites, and the semiconductors. The photorefractive effect has also been demonstrated in polymers [71, 72], and liquid crystals [73]. Each material has its own characteristics (diffraction efficiency, response time, spectral sensitivity...) and none of them is optimal for all applications involving the photorefractive effect.

Ferroelectric crystals have high electro-optic coefficients r_{ijk} and large sensitivity, making them good candidates for photorefractive applications such as second harmonic generation [59]. This family includes several crystals such as Barium Titanate ($BaTiO_3$), Lithium Niobate ($LiNbO_3$), Lithium Tantalate ($LiTaO_3$), and Tin Hypothiodiphosphate ($Sn_2\ P_2\ S_6$). The ferroelectric materials have broadband sensitivity, which varies from 350 nm to 4 μm.

Sillenites are known for their high photoconductivity and lower electro-optic coefficients r_{ijk} and dielectric coefficients compared to those of the ferroelectrics. Among these materials, we find the $Bi_{12}SiO_{20}$, $Bi_{12}TiO_{20}$ and $Bi_{12}GeO_{20}$ which are quite (have a short response time), sensitive in the visible range.

Semiconductors type III-V (GaP, GaAs, InP) or II-VI (CdS, ZnTe, CdTe) have a smaller sensitivity range than the previous materials but they are better candidates in the near-infrared. They also have extremely short response times because their carrier mobility is 100 to 1000 times higher than the ferroelectric and sillenite materials. Their electro-optic coefficients is more like that of sillenites.

In the following table [69], we will briefly present the properties of photorefractive materials. This table allows the comparison among three materials: $BaTiO_3$, $Bi_{12}SiO_{20}$ (BSO), and GaAs , which are representative of the three photorefractive material families.

Material class	Ferroelectric oxide	Sillenite	Compound semiconductor
Material	$BaTiO_3$	BSO	GaAs
Wavelength range (μm)	0.4–1.1	0.45–0.65	0.9–1.3
Electro-optic coefficient e_{eff} (pm/V)	**100** (r_{33}) **1640** (r_{42})	4 (r_{41})	1.4 (r_{41})
Dielectric constant	135 (r_{33}) 3700 (r_{11})	56	13.2
$n_b^3 r_{eff}/\varepsilon$ (pm/V)	10 (r_{33}) 6 (r_{42})	1.4	3.3
Mobility μ (cm^2/V-s)	0.01	0.1	**6000**
Recombination time τ_r (s)	10^{-8}	$\mathbf{10^{-6}}$	3×10^{-8}
Diffusion length L_d (μm)	0.01	0.5	20
Photoconductivity $\mu\tau_r$ (cm^2/V)	10^{-10}	10^{-7}	1.8×10^{-4}

Figure 2.12: Materials Parameters for $BaTiO_3$, $Bi_{12}SiO_{20}$ (BSO) and GaAs[69].

2.5.2.2 Applications

Photorefractive phenomena have been studied in different electro-optic materials. These materials have been used in a wide variety of applications such as phase conjugations, holographic memories, two-wave mixing.

Optical phase conjugation: it was first demonstrated in 1983 by Fisher et al [74]. Phase conjugation involving photorefractive crystals is an optical process that plays an important role in several application schemes, such as optical processing. This process behaves as a mirror with specific image processing (figure2.13). Indeed, it can reverse both the propagation direction and the overall phase factor of an incident electromagnetic wave [75]. Phase conjugation systems were demonstrated in photorefractive crystals with high gain such as $BaTiO_3$ and BSO [76].

Holographic storage: it has historically been the first application of the photorefractive effect. The hologram storage was studied in several photorefractive materials such as $BaTiO_3$, $LiNbO_3$, or SBN [77]. It was shown that a single crystal can store several holograms and, therefore, a large information quantity. Today, hologram finds many original applications such as information storage, holographic microscopies, and networks.

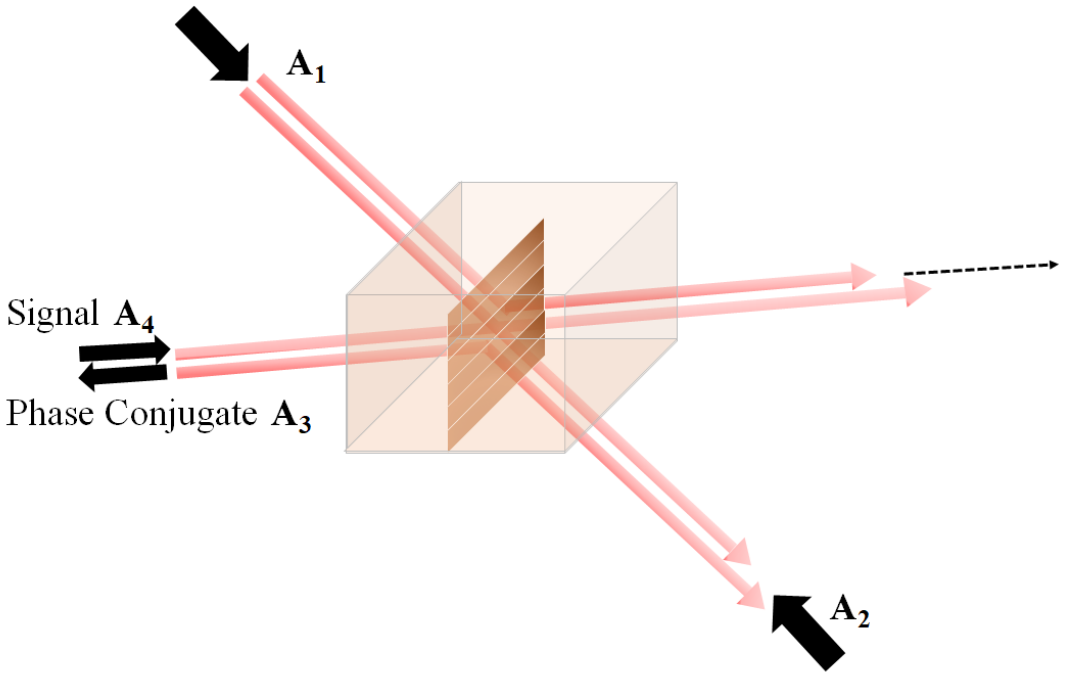

Figure 2.13: Optical phase conjugations mirror; A_1 and A_2 are pump beams, A_4 is the signal, and beam A_3 is the phase conjugate. A_1 interferes with A_4 interferes with beam 3 to write the transmission grating, A_2 interferes with beam A_4 and A_1 interferes with A_3 to write the reflection grating. A_1 interferes with A_2 to write a counterpropagating beam grating.

As shown in figure 2.14, the writing and reading of the hologram are done through the interference of two coherent beams, the signal and the pump reference. Once an index grating is induced in the material by the photorefractive effect, the hologram is written. Then the conjugated wave of the reference beam can read the grating, diffracting only in the direction of the signal.

Two-wave mixing: it will present in the next section, because of its interest in nonlinear optics. For a long time, experiments measuring energy transfer between the two beams TWM were the characteristic test used to prove that a new material type had a photorefractive effect. This energy transfer can be observed in several photorefractive materials ($LiNbO_3$[49], $BaTiO_3$ [78, 79] InP [80], $Sn_2P_2S_6$ [68, 81]) with a "non-local" index grating, i.e. in which the index grating is shifted with respect to the illumination modulation. The direction of the energy transfer depends only on the direction of the created refractive index grating, which only depends on the orientation of the crystal (signs of the electro-optic coefficients) and on the sign of the free carriers that are mostly

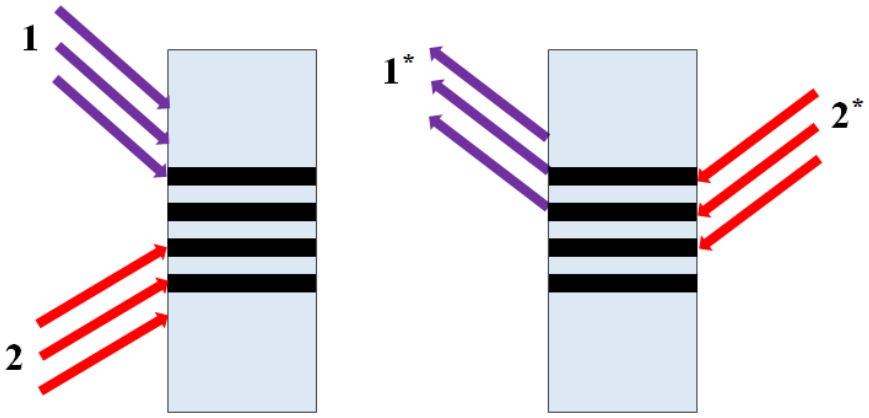

Figure 2.14: Writing and reading of the hologram by the interference of two coherent beams.

involved in the charge transport. It is possible to transfer energy from a weak beam to a strong beam as well as vice versa, and this transfer is reversed by simply rotating by 180° the photorefractive crystal.

2.5.3 Two wave mixing

2.5.3.1 Principe

The two-wave mixing process (TWM) consists of interfering two coherent laser beams emitted from the same laser called probe (with intensity I_s) and pump (with intensity I_P) respectively in a photorefractive crystal (figure 2.15). The constructive interference between the two beams inside the photorefractive medium forms an illumination grating. The linear electro-optic effect (Pockels effect) then induces a refractive index grating which is shifted by Φ with respect to the illumination modulation. The pump beam with high power transfers energy to the signal beam which is amplified at the output of the photorefractive crystal.

2.5.3.2 Diffraction of grating

The diffraction of the pump beam on the refractive index grating in the photorefractive crystal allows the transfer of one part of its energy to the direction of the signal beam. The diffraction laws for the signal and pump beams of amplitudes A_s and A_p respectively

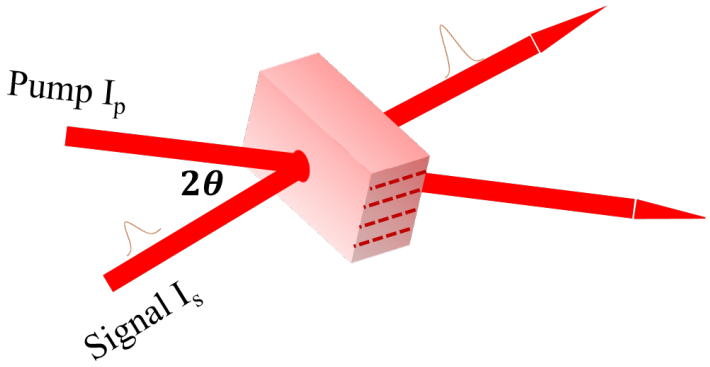

Figure 2.15: Co-directional two-wave mixing in a photorefractive crystal. Two monochromatic waves with intensities I_p and I_s interfere in a photorefractive medium and write a diffraction grating.

are controlled by the following coupling waves equations:

$$\begin{cases} \frac{\partial A_s}{\partial z} = -i\frac{\pi n^3 r_{eff}}{2\lambda cos\theta} E A_p \\ \\ \frac{\partial A_p}{\partial z} = -i\frac{\pi n^3 r^*_{eff}}{2\lambda cos\theta} E^* A_s \end{cases} \tag{2.18}$$

where z is the direction of propagation of the light waves, λ is the wavelength of the incident beams, n is the average refractive index of the crystal, r_{eff} is the effective electro-optic coefficient which depends on the orientation of the crystal and the polarization of the beams, and E is the complex amplitude of the index grating characterizing the space-charge field.

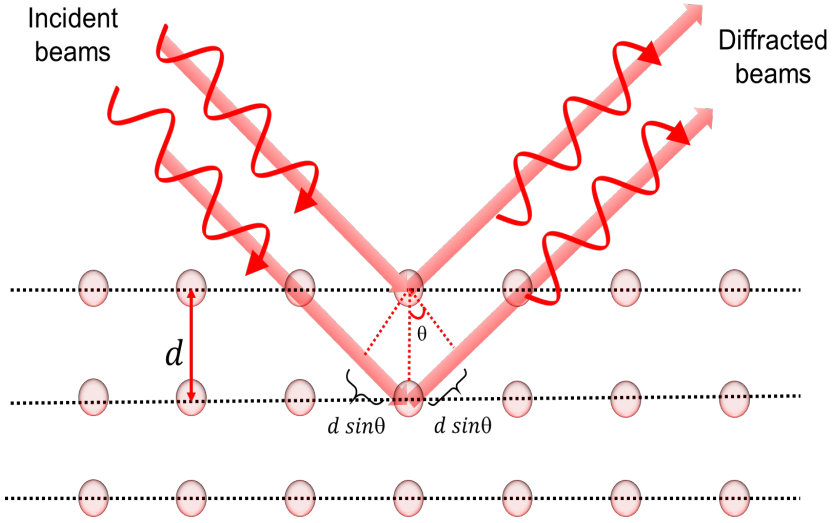

Figure 2.16: Geometry explaining beam diffraction, Bragg's law.

To ensure maximum coupling by the two-wave mixing, the angle of incidence 2θ of the beams must be properly adjusted, taking into account the Bragg condition as shown in figure 2.16. This angle is related to the grating period Λ and satisfies the known Bragg's law as follows [82]:

$$\Lambda = \frac{\lambda}{2sin\,(\theta)} \tag{2.19}$$

2.5.3.3 Photorefractive gain

The measurement of the energy transfer from one beam to the other in a photorefractive medium allows the determination of an amplification gain Γ. It is known as one of the main parameters characterizing the performance of photorefractive crystals. The photorefractive gain is usually expressed in cm^{-1} and can be very high in materials with large electro-optic coefficients such as $BaTiO_3$ [82] and SBN [83]. It can be determined from the following of the differential equations system describing the energy transfer between the beams:

$$\begin{cases} \frac{\partial I_s}{\partial z} = \Gamma \frac{I_p I_s}{I_p + I_s} \\ \\ \frac{\partial I_p}{\partial z} = -\Gamma \frac{I_p I_s}{I_p + I_s} \end{cases} \tag{2.20}$$

These equations involve only the real part of the amplitude photorefractive gain, i.e. only the non-local part of the index grating. This system can be easily solved [67]:

$$\begin{cases} I_p(d) = I_p(0) \frac{[I_s(0)+I_p(0)]e^{-\Gamma d}}{I_p(0)e^{-\Gamma d}+I_s(0)} \\ \\ I_s(d) = I_s(0) \frac{[I_s(0)+I_p(0)]e^{\Gamma d}}{I_s(0)e^{\Gamma d}+I_p(0)} \end{cases} \tag{2.21}$$

These formulas are valid whatever is the power of the incident beams. It also takes into account the saturation of the gain observed when the two laser beams have an equivalent intensity. The intensity of the amplified beam cannot be higher than the total incident intensity, because it is related to an energy exchange from one beam to the other without any external energy contribution.

When one laser beam is weaker than the other (for example $I_S \ll I_p$) over the entire thickness of the crystal d, this is called the undepleted pump case. In this configuration,

the transmitted beam intensities $I_p(d)$ and $I_s(d)$ are given by:

$$\begin{cases} I_p(d) = I_p(0) \\ \\ I_s(d) = I_s(0)e^{\Gamma d} \end{cases} \tag{2.22}$$

From these equations, we can see that the pump beam intensity does not change at the photorefractive material output while the signal amplifies or attenuates exponentially depending on the PR gain sign. The amplification coefficient γ can now be defined by the following formula:

$$\gamma = \frac{I_s(d)}{I_s(0)} = e^{\Gamma d} \tag{2.23}$$

The photorefractive gain Γ in the case of the two-wave mixing process is then given by:

$$\Gamma = \frac{1}{d} ln(\gamma) = \frac{1}{d} ln\left(\frac{I_s(d)}{I_s(0)}\right) \tag{2.24}$$

Generally speaking, the phenomena that occur in photorefractive materials are not so simple. Indeed, the photorefractive crystal is characterized by an absorption coefficient α, which may also depend on the incident intensity.

Considering the absorption, the formula that gives $I_p(d)$ and $I_s(d)$ of equation 2.22 are now given by:

$$\begin{cases} I_p(d) = I_p(0)e^{\alpha d} \\ \\ I_s(d) = I_s(0)e^{(\Gamma-\alpha)d} \end{cases} \tag{2.25}$$

2.6 PR crystal choice for slow light applications: $Sn_2P_2S_6$ crystal

2.6.1 PR crystal choice

In our thesis, we will investigate the slow light process in PR crystals and more specifically in nonlinear Tin Hypothiodiphosphate $Sn_2P_2S_6$ (SPS) which shows very promising properties at the applications telecommunication wavelengths [81]. Indeed, **1)** the SPS crystal has a large photorefractive gain and a fast response time in the visible (633 nm) and infrared

(1064 and 1550 nm) ranges wavelength [84–86]. **2)** It is known to have a transparency region that spreads from 530 nm to 8000 nm [87] and a low absorption coefficient α below 0.5 cm^{-1}. **3)** It is characterized by a narrower bandgap 2.3 eV and a high sensitivity.

Thanks to these excellent performances, the SPS is a very good candidate for many nonlinear optical applications in the red and near-infrared wavelength ranges.

Growth: the photorefractivity was first observed in the tin hypothiodiphosphate crystal by Grabar et al [88]. This crystal belongs to the metal-phosphorous-sulfur compounds $Me_2P_2S_6$ (Me = Sn, Fe, Cd) [87] obtained by the vapor transport technique using pure iodine. This method was first reported by Carpentier and Nitsche [89]. The crystals grown using this technique have good optical properties.

Crystallographic structure: at room temperature, $Sn_2P_2S_6$ has a monoclinic ferroelectric structure with monoclinic point group symmetry m [89]. At a temperature $T = 338\ K$, the SPS undergoes a second-order phase transition to the centrosymmetric para-electric phase belonging to the group $\frac{2}{m}$ [65]. The unit cell parameters in figure 2.17 are $a = 0.9378\ nm$, $b = 0.7448\ nm$, $c = 0.6513\ nm$, and $\beta = 91.15°$. The x-axis is parallel to the a-axis (parallel to the crystallographic direction) and it is oriented so that to make an angle of 13° with spontaneous polarization vector P_S. The y-axis is normal to the symmetry plane and parallels to the crystallographic b-axis and to the z-axis is parallel to the crystallographic c-axis and it is perpendicular to x- and y-axis.

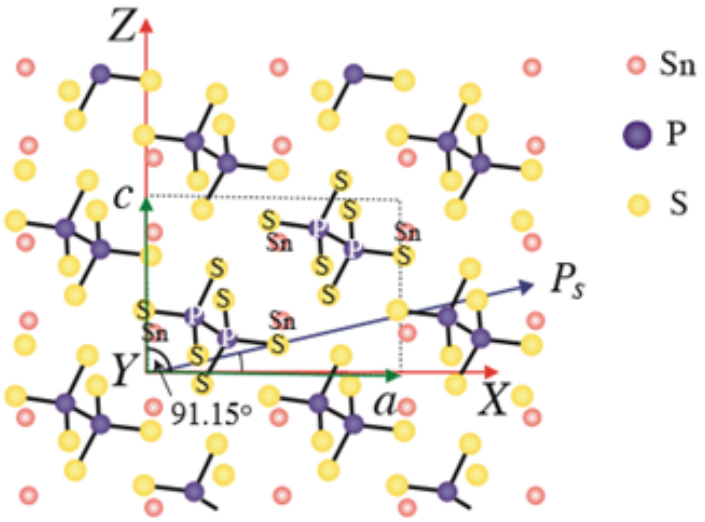

Figure 2.17: Crystallographic structure of SPS. The symmetry plane is parallel to the plane of the figure The unit cell defined by (a,b,c and β), is indicated by the dashed lines [90].

It is reported [65] that the crystallographic axes in the coordinate system described above do not suffer from variations in the orientation of the dielectric tensor and the optical indicatrix, that can be caused by varying one of the following parameters: the electric field frequency, the temperature, or the light wavelength. For its characteristic, it is known as the most one used for of the study the electro-optic phenomena and the photorefractive effect [65].

Types: depending on the transport agent chosen during the growth of SPS crystal, several types can be obtained: pure, brown and yellow SPS. In addition, different concentrations of doping (tellurium "Te", bismuth "Bi" or antimony "Sb") have been used to improve the photorefractive properties of these materials. The table below in figure 2.18 represents the parameters of each type obtained by the two-wave mixing method at different wavelengths.

$Sn_2P_2S_6$ Sample	λ (nm)	α_x (cm^{-1})	Γ_{max} (cm^{-1}) (±10%)	L_D (μm) (±50%)	r_{eff} (pm/V) (±15%)	τ_{die} at 10 W/cm^2 (ms) (±20%)	$\tau(\Gamma_{max})$ at 10 W/cm^2 (ms) (±20%)	N_{eff} (10^{16} cm^{-3}) (±15%)
Nominally pure	633	0.5	4–7	0.2			1–5	0.7
(type II) yellow	780	0.20	2.5		41		10	0.2
	860	0.16	1.8	0.9	48	9	12	0.08
	980	0.12	1.6	1.4	40	15	44	0.11
	1064	0.10	0.9		38			0.044
Brown	633	5.7	38	0.1		0.2	0.4	2.5
	780	0.9	18		180	0.4	1	0.7
	860	0.3	14		190			0.48
	980	0.14	11	0.5	190	29	33	0.39
	1064	**0.09**	**8.6**		160			0.04
SPS:Te 1.0%	633	1.0	10	0.5	60	0.1	0.3	0.9
	780	0.34	6	2.3	50	0.2	1.3	1.0
	860	0.19	6.5	0.5	89	6	10	0.44
	980	0.11	6	0.3	75	8	13	0.62
	1064	0.09	4.5					
SPS:Te 1.5%	860	0.8	8	0.5	89	7	15	0.44
	980	0.42	6	0.5	83	10	13	0.57
	1064	**0.36**	**4.5**	0.6	73	**11**	25	0.53
SPS:Te 2.0%	633	1.8	10	1.1	57	0.2	0.5	1.0
	780	0.6	6	0.8	47	0.5	1.6	0.8
	1064	0.10	2.2	0.9	54	17	32	0.22
SPS:Te 3.0%	633	2.7	12	2.6	81	0.1	0.4	0.8
	780	0.9	7	0.7	56	0.6	1.3	0.8
	1064	0.20	2.5	0.8	49	14	20	0.34
SPS:Sb 1.0%	633	1.4	20	0.7	110	0.2	0.4	1.0
	780	0.08	0.4					

Figure 2.18: Parameters of pure, brown, Te-and Sb- doped SPS crystal at different wavelengths.

2.6.1.1 Optical proprieties of SPS

The optical properties of the SPS crystals were first reported by Gurzan et al. in 1977. It is shown that the properties depend on the crystal growth method.

Refractive index: the SPS is a biaxial crystal and it has three different refractive indexes, n_1, n_2, n_3. The indicatrix orientation of the index is presented in figure 2.19. The spontaneous polarization axis P_s is deviated by 13° from the x-axis. The variation of the refractive index as a function of the wavelength λ is approximated by a two-term Sellmeier oscillator model [65]:

$$n^2(\lambda) - 1 = \frac{S_0 \lambda_0^2}{1 - (\lambda_0/\lambda)^2} \tag{2.26}$$

where S_0 and λ_0 are the oscillator strength and wavelength of a single-oscillator Sellmeier model. At the wavelength of 1.06 μm, the values of the refractive indices n_1, n_2, n_3 are 2.82, 2.71, and 2.9 [91] respectively.

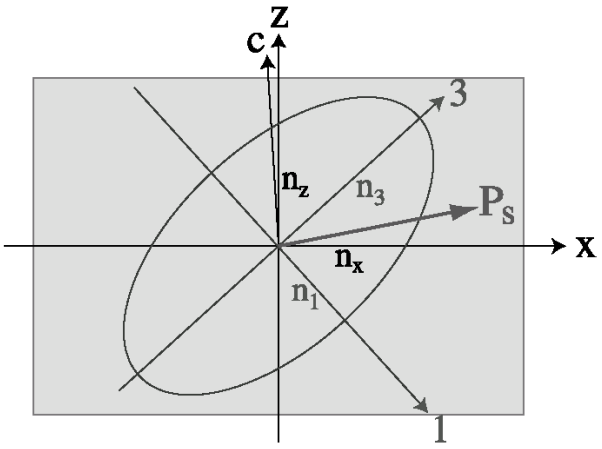

Figure 2.19: The indicatrix orientation and the position of spontaneous polarization at room temperature.

Electro-optic tensor: the third-rank electro-optical tensor (r_{ijk}) for monoclinic materials has ten (10) independent coefficients whose expression is given as follows:

$$r_{ijk} = \begin{pmatrix} r_{111} & 0 & r_{113} \\ r_{221} & 0 & r_{223} \\ r_{331} & 0 & r_{333} \\ 0 & r_{322} & 0 \\ r_{131} & 0 & r_{133} \\ 0 & r_{122} & 0 \end{pmatrix} \tag{2.27}$$

In 2002, D. Haertle et al. [65] measured the room temperature free electro-optic coefficients of the first column at $\lambda = 633\ nm$ wavelength. 1) At high-frequency, the electro-optic coefficient values are: $r_{111} = 174\ pm/V$, $r_{221} = 92\ pm/V$, $r_{331} = 140\ pm/V$, $r_{131} = -25\ pm/V$. 2) At low frequency, their values are: $r_{111} = 50\ pm/V$, $r_{221} = 11\ pm/V$, $r_{331} = 42\ pm/V$, $r_{131} = -11\ pm/V$.

Response time: the SPS crystal is characterized by two types of charge carriers, which are responsible for the creation of two photorefractive gratings under a laser illumination. A "fast" grating is built up by the redistribution of photoexcited carriers (electrons). A "slow" grating forms due to the redistribution of passive carriers (holes). As a consequence, these photorefractive gratings provide two different crystal response times, τ_f and τ_s. Then, the holes partially compensate the initial grating and provide another response that is called self-compensation response [92, 93].

The characteristic response function f_ω of the SPS crystal is given as follows:

$$f_\omega = \frac{b - 1\omega\tau_s}{(1 - \omega\tau_f)(1 - 1\omega\tau_s)} \tag{2.28}$$

where ω is the frequency detuning and $b < 1$ is the compensation factor.

According to the literature, the PR response time is inversely proportional to the total intensity [4].

2.6.1.2 Our samples

Analyzing the characteristics of the SPS presented in the table of figure 2.18, we have chosen two samples for our experiments: Te-and Sb-doped SPS. They offer the best performances, high gain and very short response time in the visible and infrared range. These samples come from the Institute of Solid State Physics and Chemistry, Uzhgorod National University", Uzhgorod, Ukraine. They were obtained by the gas-phase transport method.

In the following table, we present the important characteristics of our SPS samples at 638 nm, which are interesting for the study of the slow light process.

Crystals	Doping	Thickness (mm)	Response time (ms)	Gratings period (μm)
SPS: Te	1%	5	10	1.8
SPS: Sb	1%	8	10	1.8

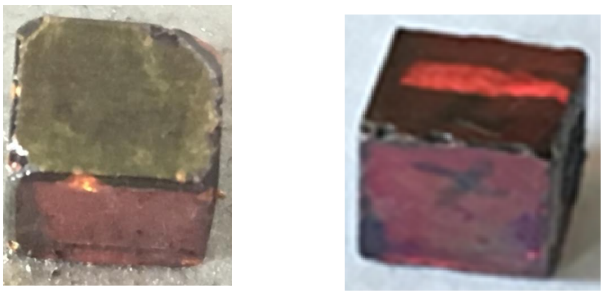

Figure 2.20: Pictures of the crystal samples. (a) SPS doped Te. (b) SPS doped Sb.

It should be noted that the response times of the PR crystals are measured by the two-wave mixing method, and the grating period is deduced from the Bragg formula.

3

Slow light using TWM

Contents

In the previous chapter we have reviewed the different methods to slow light, specifically in PR materials. In this chapter, we will first report the theory of deceleration of light using the photorefractive two-wave mixing process and secondly, we will present the theoretical determination regarding the delay time, the output pulse amplification and width as a function of the PR gain and the input pulse duration. We will optimize the TWM experiment in a photorefractive material at room temperature to slow down the light at visible wavelengths. We specifically address the question of the slow light performances in terms of group velocity reduction and fractional delay.

Most of our conclusions in this chapter are summarized in our publication [12].

3.1 State of the art and theoretical background of TWM

We have seen that the slowing down of light can be achieved in high-dispersion materials such as optical fibers [2] and photonic crystals [24]. Recently, it has been shown that photorefractive nonlinearity can also be used for the slowing down of pulse propagation at visible wavelengths. It was shown that the group velocity of light can be reduced using the recording of dynamic refractive index gratings in photorefractive crystals [94, 95]. The deceleration of light pulses is achieved using a beam coupling method at room temperature [4, 96]. The beam coupling yields amplification of the output pulse and modifies the light dispersion inside the crystal, hence reducing the group velocity of this pulse. Slow light in photorefractive crystals has several advantages compared to other systems. The process does not require precise frequency adjustment and can operate at room temperature in many materials. Moreover, the PR nonlinearity allows the amplification of the pulse at the crystal output unlike in the case of the EIT method. The pulse delay range can be varied as a function of the TWM gain and of the response time of the PR crystal.

In the last fifteen years, several PR materials have been employed to slowdown light pulses using the TWM process at room temperature [95, 97, 98]. Podivilov et al. demonstrated a large group velocity light reduction [4]. Their experiments are performed with a $BaTiO_3$ sample with thickness $d = 2\ mm$ and a response time of 3.5 s. As shown in figure 3.1, for a PR gain $\Gamma = 40\ cm^{-1}$, a pulse with a width at a half-maximum level equal to 0.76 s was delayed by $\Delta\tau = 8\ s$ corresponding to a group velocity $v_g = 0.025\ cm/s$. In the same time, the output pulse is strongly broadened with time which reduces the output bandwidth. Three years later, some new results have shown the reduction of the broadening of the

transmitted pulse in this material [99]: they used an artificial dispersive inhomogeneity produced by Bragg selectivity to slow simultaneously three spectral components of an input optical pulse in Ce: $BaTiO_3$. Then to solve the distortion problem, they coupled multiple pump beams with different frequencies and an input pulse. They showed theoretically that by using six pumps, a 1 s pulse can decelerate by 4 s without any distortion at the output of the crystal.

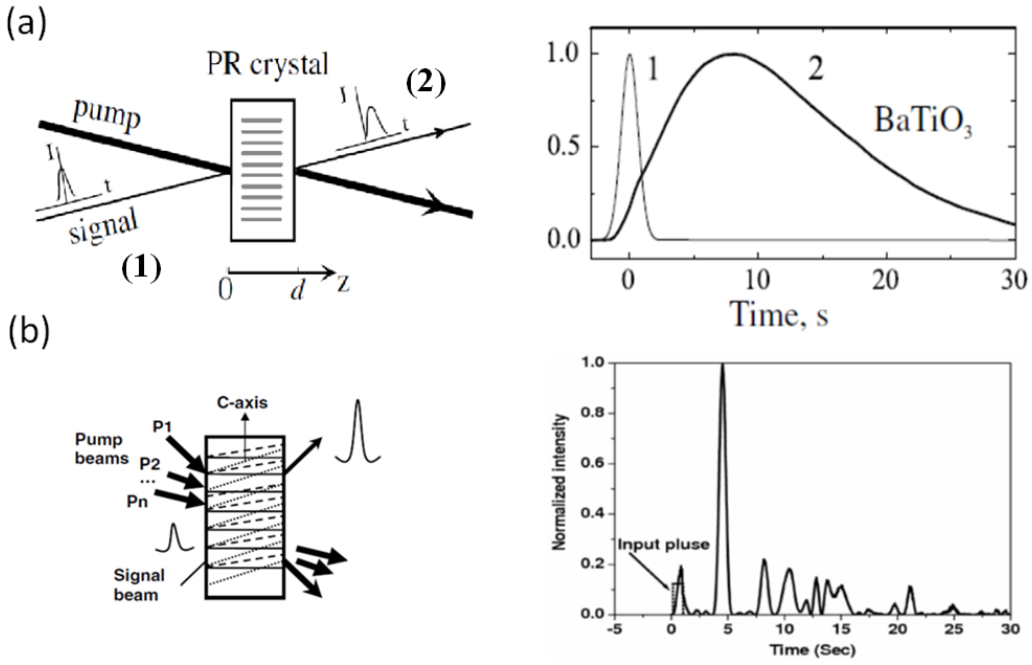

Figure 3.1: (a) Normalized input and output intensities of the signal curves 1 and 2, respectively as a function of time for a $BaTiO_3$ crystal length $d = 2\ mm$ and response time 3.5 s [4]. (b) Simulated output pulse with six pump beams [99].

Other groups have studied theoretically and experimentally the parameters that can vary the delay time and the shape of the output pulse for different types of photorefractive response [100, 101]. They demonstrated analytically that in all photorefractive crystals with local, nonlocal, diffusion, or photovoltaic response, the delay depends on the photorefractive gain and on the input pulse duration. The self-compensating responses which are present in some PR materials such as SPS and which are described in section (2.6), can both slowdown and speedup the light pulse simultaneously [93, 102]. Here, depending on the orientation of the polarization axis which can change the energy transfers of the TWM, the light pulse can be delayed or accelerated in the crystal [102] (figure 3.2).

Slowing down of light pulses can also be achieved using other nonlinear processes: pho-

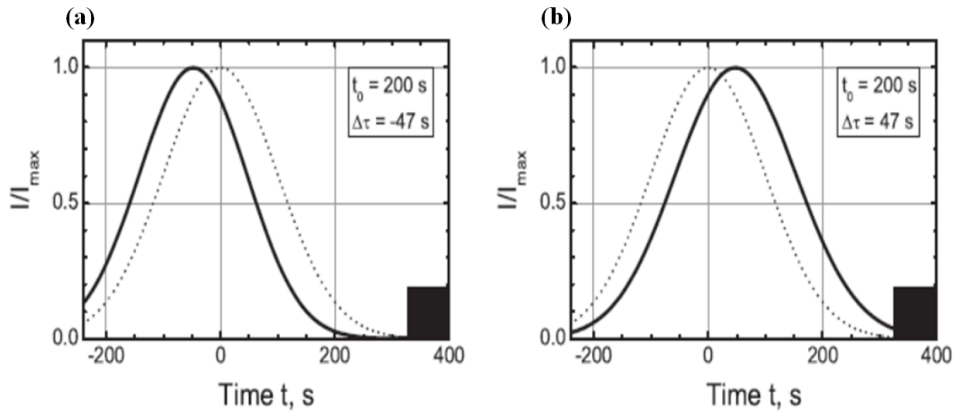

Figure 3.2: Normalized input signal pulse (dots) and calculated temporal envelopes at the sample output face (solid lines) respectively as a function of time for an input pulse duration $t0 = 200\ s$. (a) The orientation of the sample c axis is chosen to ensure the advancement of the signal pulse. (b) the sample is rotated through 180° and the signal pulse is delayed [102]

torefractive four-wave mixing [10, 98]. The interaction geometry of this process is shown in figure 3.3. The medium is pumped by two beams 1 and 2. The pulse signal 4 which propagates in the z-direction interferes with the beams 1 and 2 and then gives rise to the phase conjugated pulse 3. Using the four-wave mixing, both the transmitted 4 and the phase conjugate 3 pulses can be decelerated. Also, the phase conjugate pulse 3 has a longer delay and fractional delay compared to the transmitted pulse 4 in most of the considered experimental conditions [96].

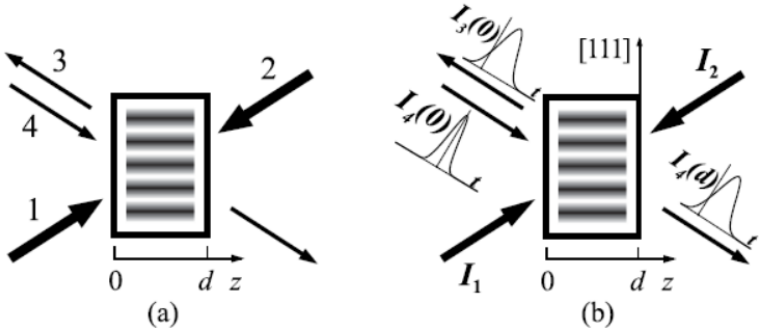

Figure 3.3: Geometric scheme of the backward four-wave coupling in a photorefractive crystal. The PR crystal is pumped with two counterpropagating beams 1 and 2, the signal beam 4 sent to the crystal and interacts with the pumps giving rise to the phase-conjugate 3 which is the replica of signal wave 4 for a pair of pump waves [96].

3.1.1 Theoretical modeling

The photorefractive TWM geometry for the slow light in the SPS crystal is presented in figure 2.15. An intense continuous pump beam and a weak Gaussian pulse with complex amplitudes A_p and $A_s = A_0 exp(-t^2/T_0^2)$ (where T_0 is the width parameter which is useful for analytical and numerical treatments, the half input pulse width, taken at $1/e$ time the maximum of A_s, is here $\sqrt{ln2/2}T_0$) respectively are injected to a PR crystal with thickness d.

The diffraction of both waves on the PR grating can be presented by the equation 2.18 presented in section 2.7. Let now consider the electric field complex amplitudes of the pump and the pulse $A_p(z,t)$ and $A_s(z,t)$ respectively propagating in the z-direction. In the undepleted pump approximation ($A_p \gg A_s$), $A_p(z,t) = A_p$ and the Fourier transform of the normalised output pulse $A(d) = A_s(d)/A_p$ is given by $A_\omega(d)$:

$$A_\omega(d) = A_\omega(0)e^{gd} \tag{3.1}$$

where $A_\omega(0)$ is the Fourier transform of $A(0,t)$ and $g = \Gamma f_\omega$ is a dimensionless parameter conventionally defined as the coupling strength with Γ being the PR gain and f_ω [93] is the characteristic response function (formula given in section (2.8): equation 2.28). For $\omega\tau_s \gg 1$, the characteristic response time of the SPS crystal is similar to that of other PR crystals which is defined as the diffusion response time $\tau = \tau_f$. In that case, g becomes:

$$g = \frac{\Gamma}{(1 - i\omega\tau)} \tag{3.2}$$

In the case of the TWM, the impact of the nonlinearity of the PR medium on the propagation of light is characterized by the coupling strength g. Figure 3.4 shows the dependence of g on $\omega\tau$. The real part of g, $g_1 = \Gamma/(1 + \omega^2\tau^2)$ shows the spatial amplification which is an even function with a maximum at $\omega = 0$. The imaginary part of g, $g_2 = \Gamma\omega\tau/(1 + \omega^2\tau^2)$, is related to the group velocity $v_g = \partial g_2/\partial\omega$ [100, 101].

By using the inverse Fourier transform, the output pulse electric field amplitude $A(d,t)$ is given by:

$$A(d,t) = A_0 \frac{T_0}{2\sqrt{\pi}} \int_{-\infty}^{\infty} e^{-0.25\omega^2 T_0^2 + g_d - i\omega t} d\omega \tag{3.3}$$

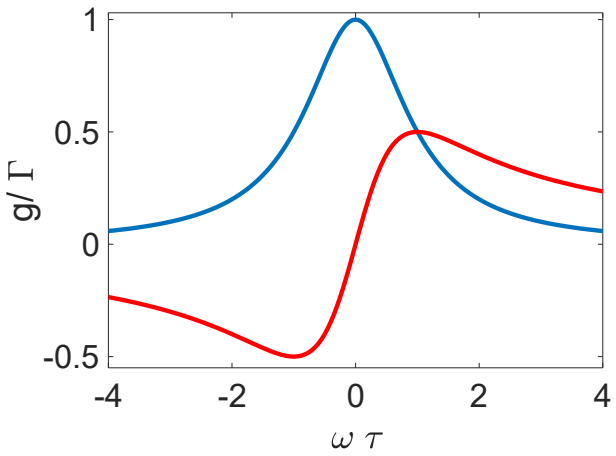

Figure 3.4: Dependence of g on $\omega\tau$. Blue and red curves are respectively the real g_1 and the imaginary g_2 parts of g.

where T_0 is the input width parameter which is useful for analytical and numerical treatments.

3.1.2 Slow light performances using TWM as a function of the input parameters

Generally speaking, the performances of the slow light process achieved in photorefractive materials depend essentially on the PR TWM gain and the input pulse duration.

In this section, we will give the mathematical equations and then some theoretical results that illustrate these dependencies. Equation 3.3 can be analytically calculated using saddle-point approximation [101] to get the relation of the delay and output pulse duration. This approximation can be used under specific hypotheses such as $\Gamma d > 1$ and $\omega\tau_s << 1$. In that case, and by replacing the expression of f_ω (equation 2.28 in section (2.8)) in $g = \gamma f_\omega$, this last one can be writing as:

$$g = \Gamma(b + \omega^2\tau_s^2) - i\Gamma\omega\tau_s \tag{3.4}$$

By replacing g (3.4) in 3.3, we get:

$$A(d,t) = A_0\frac{T_0}{2\sqrt{\pi}}e^{\Gamma db}\int_{-\infty}^{\infty} e^{-0.25\omega^2T_0^2+\Gamma\omega^2\tau_s^2 d-i\Gamma\omega\tau_s d-i\omega t}d\omega \tag{3.5}$$

Now, we consider:

$$s(\omega) = -0.25\omega^2T_0^2 + \Gamma\omega^2\tau_s^2 d - i\Gamma\omega\tau_s d - i\omega t \tag{3.6}$$

and we calculate its first and second derivatives $s^{'}(\omega)$ and $s^{''}(\omega)$:

$$\begin{aligned} s^{'}(\omega) &= -0.5\omega T_0^2 + 2\Gamma\omega\tau_s^2 d - i(\Gamma\tau_s d - t) \quad (3.7)\\ s^{''}(\omega) &= -0.5T_0^2 + 2\Gamma d\tau_s^2 \quad (3.8) \end{aligned}$$

Now, we calculate ω_0 for which $s^{'}(\omega) = 0$:

$$-0.5\omega T_0^2 + 2\Gamma\omega\tau_s^2 d - i(\Gamma\tau_s d - t) = 0 \quad (3.9)$$

$$\omega_0 = -2i\frac{\Gamma d\tau_s + t}{T_0^2 - 4\Gamma d\tau_s^2} \quad (3.10)$$

Then, if we compute $S(\omega)$ at $\omega = \omega_0$, we obtain:

$$\begin{aligned} s(\omega_0) &= \left(-\frac{1}{4}T_0^2 + \Gamma d\tau_s^2\right)\left(-2i\frac{\Gamma d\tau_s + t}{T_0^2 - 4\Gamma d\tau_s^2}\right)^2 - i\left(\Gamma d\tau_s + t\right)\left(-2i\frac{\Gamma d\tau_s + t}{T_0^2 - 4\Gamma d\tau_s^2}\right)\\ &= -\frac{(\Gamma d\tau_s + t)^2}{T_0^2 - 4\Gamma d\tau_s^2} \end{aligned} \quad (3.11)$$

According to the saddle-point approximation [103], we can write $s(\omega)$ as follows:

$$\begin{aligned} s(\omega) &= s(\omega_0) + \frac{1}{2}s^{''}(\omega)(\omega - \omega_0)^2\\ &= -\frac{(\Gamma d\tau_s + t)^2}{T_0^2 - 4\Gamma d\tau_s^2} + \frac{1}{2}\left(-0.5T_0^2 + 2\Gamma d\tau_s^2\right)(\omega - \omega_0)^2 \end{aligned} \quad (3.12)$$

Then by replacing the equation. 3.12 in the equation. 3.5, we obtain:

$$\begin{aligned} A(d,t) &= A_0\frac{T_0}{2\sqrt{\pi}}e^{\Gamma db}\int_{-\infty}^{\infty} e^{-\frac{(\Gamma d\tau_s + t)^2}{T_0^2 - 4\Gamma d\tau_s^2} + \frac{1}{2}\left(-0.5T_0^2 + 2\Gamma d\tau_s^2\right)(\omega - \omega_0)^2} d\omega\\ &= A_0\frac{T_0}{2\sqrt{\pi}}e^{\Gamma db}e^{-\frac{(\Gamma d\tau_s + t)^2}{T_0^2 - 4\Gamma d\tau_s^2}}\int_{-\infty}^{\infty} e^{\frac{1}{4}\left(T_0^2 - 4\Gamma d\tau_s^2\right)(\omega - \omega_0)^2} \end{aligned} \quad (3.13)$$

This integral has a form similar to $\int_{-\infty}^{\infty} e^{-\alpha x^2}dx$ so we can calculate $\frac{A(d,t)}{A_0}$:

$$\begin{aligned} \frac{A(d,t)}{A_0} &= \frac{T_0}{2\sqrt{\pi}}e^{\Gamma db}e^{-\frac{(\Gamma d\tau_s + t)^2}{T_0^2 - 4\Gamma d\tau_s^2}}\sqrt{\frac{\pi}{T_0^2 - 4\Gamma d\tau_s^2}}\\ &= \frac{T_0}{T_0^2 - 4\Gamma d\tau_s^2}e^{-\frac{(\Gamma d\tau_s + t)^2}{T_0^2 - 4\Gamma d\tau_s^2}} \end{aligned} \quad (3.14)$$

From this equation, we can deduce that the output pulse has a "Gaussian shape". The maximum time delay $\Delta\tau$ and the output width parameter at $1/e$, which we identify as T_1, are:

$$\Delta\tau = -\Gamma d\tau_s \tag{3.15}$$

$$T_1 = \sqrt{T_0^2 - 4\Gamma d\tau_s^2} \tag{3.16}$$

The theoretical fractional delay is:

$$FD = \frac{\Delta\tau}{T_1} = \frac{\Gamma d\tau_s}{\sqrt{T_0^2 - 4\Gamma d\tau_s^2}} \tag{3.17}$$

Dependence on the PR gain:

From equation 3.15, we can see that the maximum delay that can be theoretically reached is fixed by the gain Γ value. This situation can be demonstrated by calculating the profiles of an input pulse with a duration $T_0 = 50\ ms$ and related output pulse for different values of Γ. As shown in figure 3.5, the output pulses are delayed in time and the delay increases with increasing Γ.

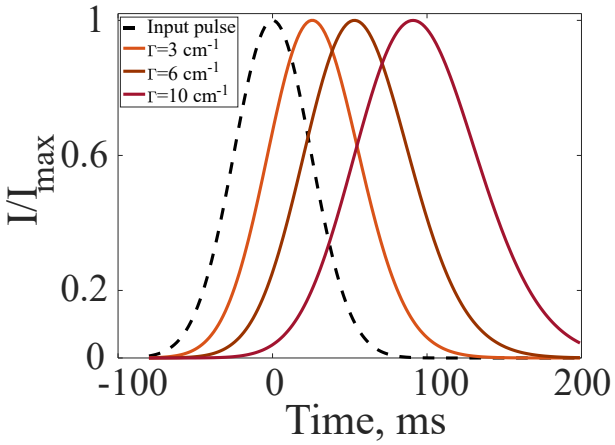

Figure 3.5: Normalized input signal pulse (black dots) of duration $T_0 = 50\ ms$ and calculated temporal envelopes of output pulses (solid lines) for three values of Γ. Delay $\Delta\tau = 25, 53.5, 91\ ms$ are calculated for $\Gamma d = 3, 6, 10\ cm^{-1}$ respectively.

Dependence on the input pulse width:

The time delay value changes also with respect to the input pulse duration for a fixed gain value Γ. This situation is presented in figure 3.6. We can see that, if we increase T_0, the value of $\Delta\tau$ vary. As illustrate in 3.6 (a,b,c), for $T_0 = 0.05,\ 0.07\ \ s$ and $1\ s$, the output

pulses are delayed respectively by 0.025 s, 0.027 s and 0.3 s. Figure 3.6 (d) shows what happens for the output pulse duration when increasing the PR gain and the input pulse duration. We can see that this duration increases with both parameters. Figure 3.6 (d) shows that the output pulse broadens compared to the ideal case (T_1=T_0) particularly for $T_0/\tau \ll (\Gamma d)^{1/2}$. However, for a sufficiently large value of T_0/τ (equation 3.16), we note that the output pulse width T_1 close to T_0.

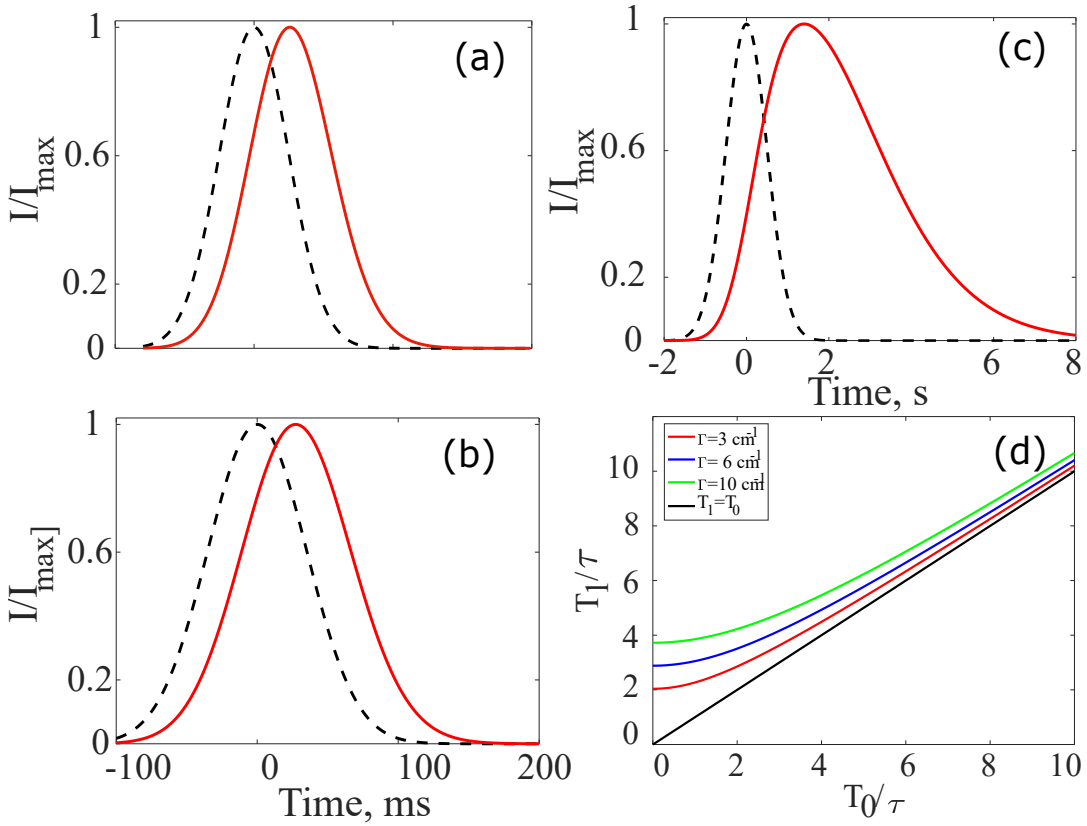

Figure 3.6: Normalized input pulses (black dots) of duration $T_0 = 0.05$, 0.07 and 1 s, (a), (b) and (c) respectively and calculated temporal envelopes of output pulses (solid lines) for $\Gamma d = 3$. d) Output pulse duration as a function of the input pulse duration for different values of Γ calculated with equation 3.16.

Dependence on the crystal response time:

The value of the PR crystal response time τ can also enhance the delay time performances. Using equation 3.5, we simulate the output pulse intensity for different response time τ and we calculate the corresponding delay for a fixed input pulse duration T_0 and gain Γ. Figure 3.7 plots the evolution of the delay and the output pulse duration versus the photorefractive response time for an input pulse duration $T_0 = 20$ ms and $\Gamma d = 12$. We

note that the theoretical value of the delay increases with the response time and its values can be larger than the input pulse width when $T_0/\tau \ll \Gamma d$ and the pulse propagates without any distortion. When $\tau \ll T_0$ the delay is smaller and the output pulse is broadened compared to the input one.

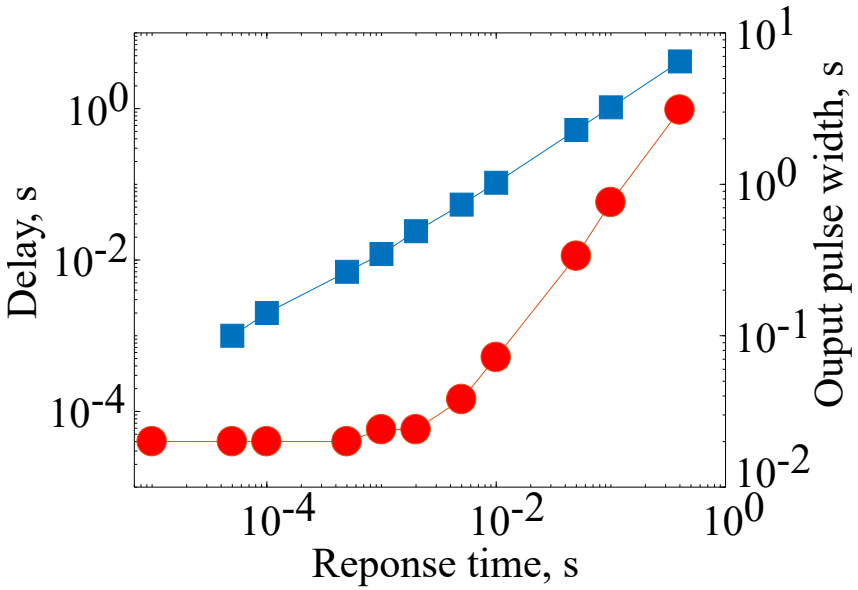

Figure 3.7: Delay time (red curve) and output width (blue curve) as a function of the PR response time, $T_0 = 20\ ms$, $\Gamma d = 12$

In the following, we use a 0.5-cm SPS photorefractive crystal with response time $\tau = 10$ ms at 638 ns to study first the TWM effect and secondly to measure the slow light performances at room temperature.

3.2 Experimental slow light results

The slowdown of light pulses in a SPS crystal using a two-wave mixing process has been studied theoretically [93] and experimentally [94] at visible wavelengths. In 2003, Podivilov. et al. [4] measured a small group velocity of 40 cm/s and a fractional delay value of 0.4 in the SPS considering ms pulse duration (figure 3.8). In this chapter, our objective concerns the optimization of a TWM process using the same crystal in order to improve the slow light performances in terms of delay, fractional delay and the pulse durations that vary from a few μs to s.

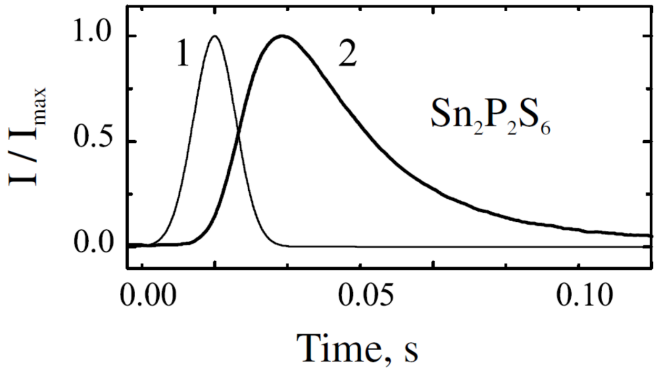

Figure 3.8: Slow-light using TWM configuration in the PR SPS. Group velocity of 40 cm/s is measured at room temperature [4].

3.2.1 Experimental setup

Figure 3.9 shows our experimental setup. A Crystal laser LC Reno, NV 89502 (Model No. DL638-070-SO) at ($\lambda = 638nm$) with an intensity of 3.8 W/cm^2 is split into two coherent waves, a weak signal S and a strong pump P with powers of 17 mW and 40 mW respectively. The signal is modulated by a NewFocus Model 4002-Visible Phase Modulator (EOM) to have a Gaussian optical pulse shape. The signal power is adjusted by an attenuator (A) placed before the modulator. The continuous pump beam and the signal pulse are injected inside a 0.5 $cm-$ long SPS crystal with response time $\tau = 10\ ms$ through the z-direction with a certain angle θ. Finally, the input and the output pulses are detected by two amplified silicon photodiodes (D_1) and (D_2) and analyzed by an oscilloscope.

In the following, we will use this setup to evaluate the PR gain Γ in order to optimize the slow light performance in the PR SPS crystal.

3.2.2 Experimental photorefractive gain

Using this TWM experimental setup, we will measure the gain of the two-wave mixing induced by the interference of signal and pump beams. Then, we will relate this gain parameter to the slow light performances. As reported in the literature [94, 101], the PR gain depends on several input parameters such as the input laser beam intensity, the photorefractive grating period Λ or the incident angle θ, the rotation of the crystal and the polarization of the input beams. In the following, we measure the amplification term

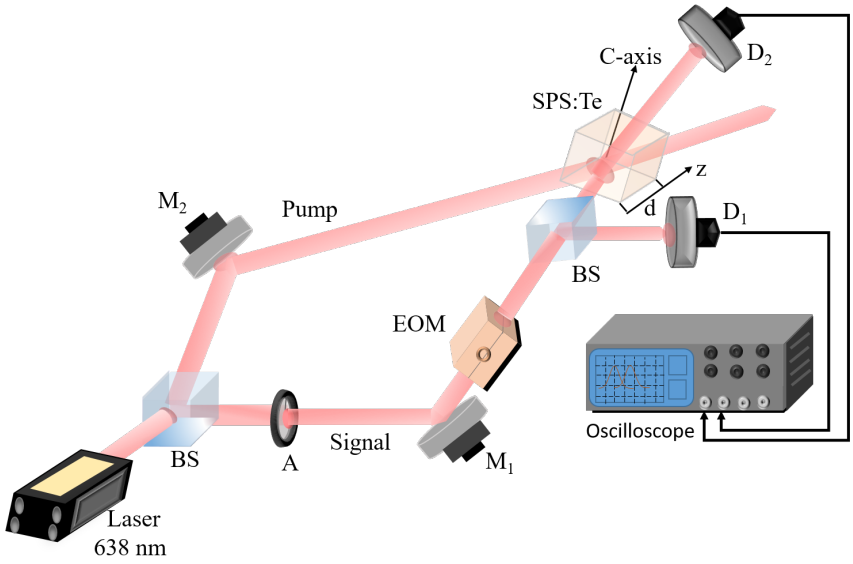

Figure 3.9: Slow-light experimental setup using TWM configuration in the PR SPS with thickness d; EOM: electro-optic modulator, $D_{1,2}$: photo-detectors, $M_{1,2}$: mirrors, SG: signal generator and BS: beam splitter.

$\gamma = I_s(d)/I_s(0)$ as a function of the ratio between the pump and signal intensities $I_p/I_s(0)$ in the case of horizontal polarization. Then, the photorefractive gain Γ is related to γ through the Kukhtarev model [67] and equation 2.21.

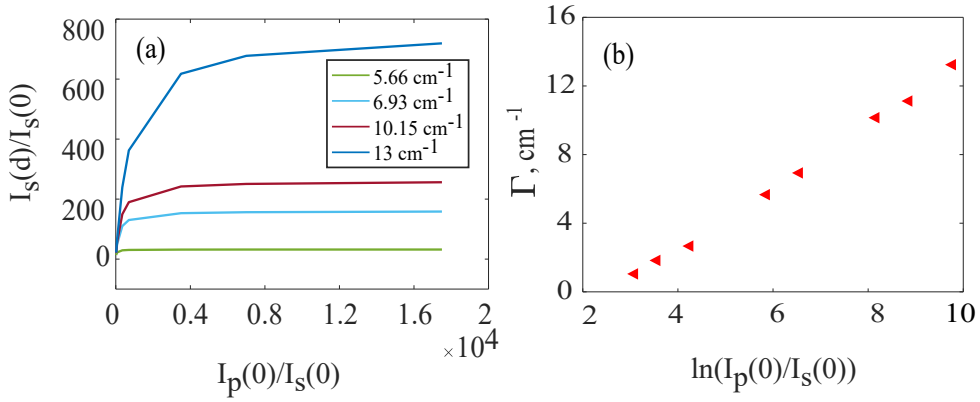

Figure 3.10: (a) Dependence of the amplification factor $\gamma = I_s(d)/I_s(0)$ versus the input intensity ratio $m = I_p(0)/I_s(0)$ for different photorefractive gain values. (b) Dependence of PR gain Γ on m for a grating period $\Lambda = 1.9\ \mu m$ and total input power $P_0 = 35\ mW$ in the case of horizontal polarization [12]

To measure the photorefractive gain, we fix the pump power $P_p(0)$ and vary the signal power $P_s(0)$ using an attenuator from 3 mW to 2 μW. Then we measure the output

intensity $I_s(d)$ and the amplification factor γ. Figure 3.10 (a) plots the measured variation of γ versus the pump signal ratio m for the corresponding Γ with a photoinduced refractive index grating with period $\Lambda = 1.9\ \mu m$. Figure 3.10 (b) plots the photorefractive gain Γ versus $ln(m)$. We note that the PR gain varies with m and a maximum value of Γ of 13 cm^{-1} is measured for an amplification factor $\gamma = 750$ and total input power $P_0 = P_p(0) + P_s(0) = 35\ mW$.

In the following, we use the previous setup to measure the slow light performances such as the delay, the group velocity and the fractional delay both at the visible and infrared wavelengths.

3.2.3 Slow light measurement: group delay and velocity

As discussed in the first chapter, when a single pulse is delayed, the delay time is usually defined in terms of the peak position of a single Gaussian pulse: it is the delay between the maximum of the transmitted signal and input signal. To estimate this delay, we measure the input and the output pulses intensities using two photodetectors. We then measure the delay $\Delta\tau$ and the full output pulse duration at half maximum:

$$\Delta\tau = t_2 - t_1 \tag{3.18}$$

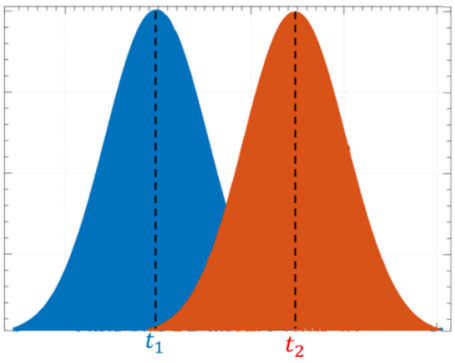

Figure 3.11: Experimental measurement of the group delay.

with t_1 and t_2 are presented in figure 3.11. Finally, the group velocity v_g can then be estimated as the ratio between the distance traveled by the pulse (crystal thickness d) and the measured delay:

$$v_g = \frac{d(cm)}{\Delta\tau(s)} \tag{3.19}$$

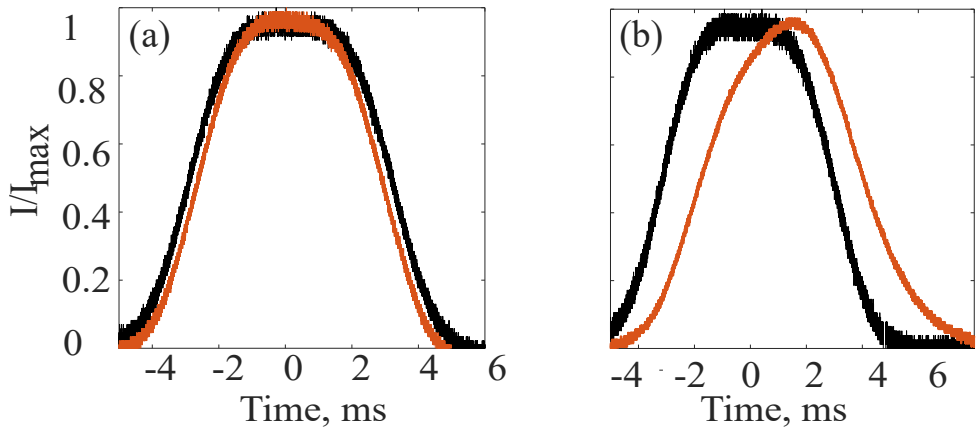

Figure 3.12: Envelopes of the input pulse (black line) and output pulse without (a) and with two-wave mixing in the SPS crystal [11].

Figure 3.12 shows an experimental result of the slowdown of a light pulse of full width at half maximum (FWHM) $t_0 = 1.3\ ms$ (this pulse duration differs from T_0) . In the absence of the interference of the pump and the signal, no delay is observed when the pulse passes through the material. In the presence of the PR TWM process, the output pulse is amplified and delayed by 0.26 ms compared to the input pulse. In the following paragraph, we give more experimental results which show the dependence of the delay and the output pulse durations on the strength of the beam coupling and the input pulse duration. It will then allow us to deduce the best experimental conditions to control and optimize slow light performances.

3.3 Controlling the light velocity SPS

3.3.1 Delay and fractional delay as a function of TWM gain

The measured TWM gain is related to the slow light performance and consequently to the delay and the fractional delay. To see this dependence, we inject an input pulse with a width close to the response time of the crystal $\tau_0 = 10\ ms$ through the PR crystal and we measure $\Delta\tau$ and the corresponding FD for different values of Γd. By analyzing the pulses intensity evolution measured by $D_{1,2}$, we observe that the transmitted pulse is delayed by comparison to the reference input pulse. The curves of figure 3.13 show that both the delay and FD increase with the PR gain. Under the optimal conditions, *ie* a

photorefractive gain $\Gamma = 9.4\ cm^{-1}$ and despite the output pulse widening, we measure a delay time $\Delta\tau = 9.4\ ms$ close to the pulse duration t_0 (figure 3.13(b)).

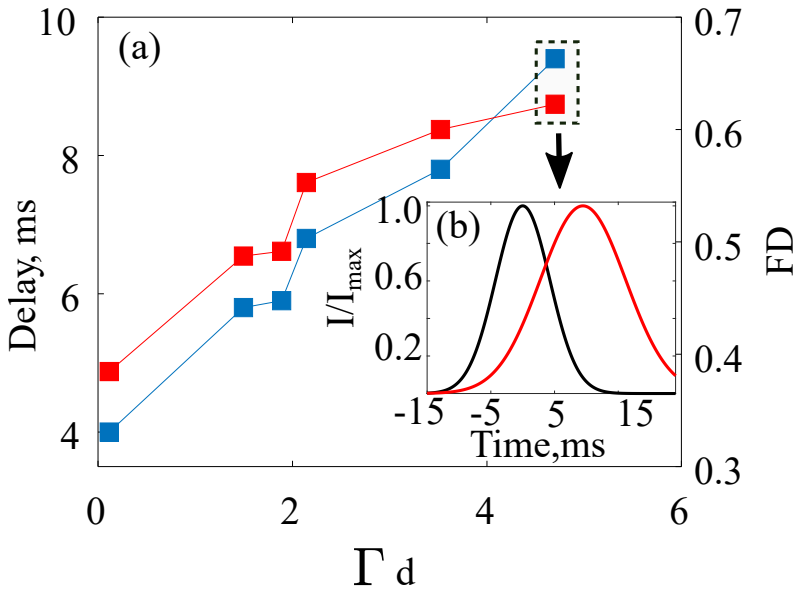

Figure 3.13: Delay time (blue curve) and fractional delay FD (red curve) as a function of Γd for an input pulse with duration 10 ms.(b) (b) Delay time of 9.4 ms for $\Gamma = 9.4\ cm^{-1}$ (period grating $\Lambda = 1.9\ \mu m$).

Also, for the same value $\Gamma = 9.4\ cm^{-1}$, a maximum fractional delay of 0.62 is measured. We can then conclude that to improve the slow light performances, it is almost important to optimize the TWM setup to get a maximum PR gain.

Figure 3.14 shows the numerical prediction and experimental data on the maximum achievable delay and the widening factor $R = t_1/t_0$ (note that t_1 and t_0 are the FWHM of output and the input pulses respectively) and the fractional delay FD as a function of Γd for an input pulse duration of 14 ms. The measurement results are compared with the theoretical ones calculated by using equation 3.5 (section (3.1)).

The numerical simulations of the time delay and FD as a function of the gain are presented in figure 3.14(a_1). The delay is found to increase with increasing Γd. Furthermore, for sufficiently large values of $\Gamma d > 2$, the delay can be higher than the input pulse duration. For example, a delay $\Delta\tau = 25\ ms$, twice as large as t_0 is calculated for $\Gamma d = 4.7$. By analyzing the experimental results, we note that the behavior of the curves of figure 3.14(a_2) is the same as the curve presented in figure 3.14(a_1), but for the same value of Γd, the measured delay is less important than the calculated one. On the other hand, the values of the experimental fractional delay are in the same range as those obtained

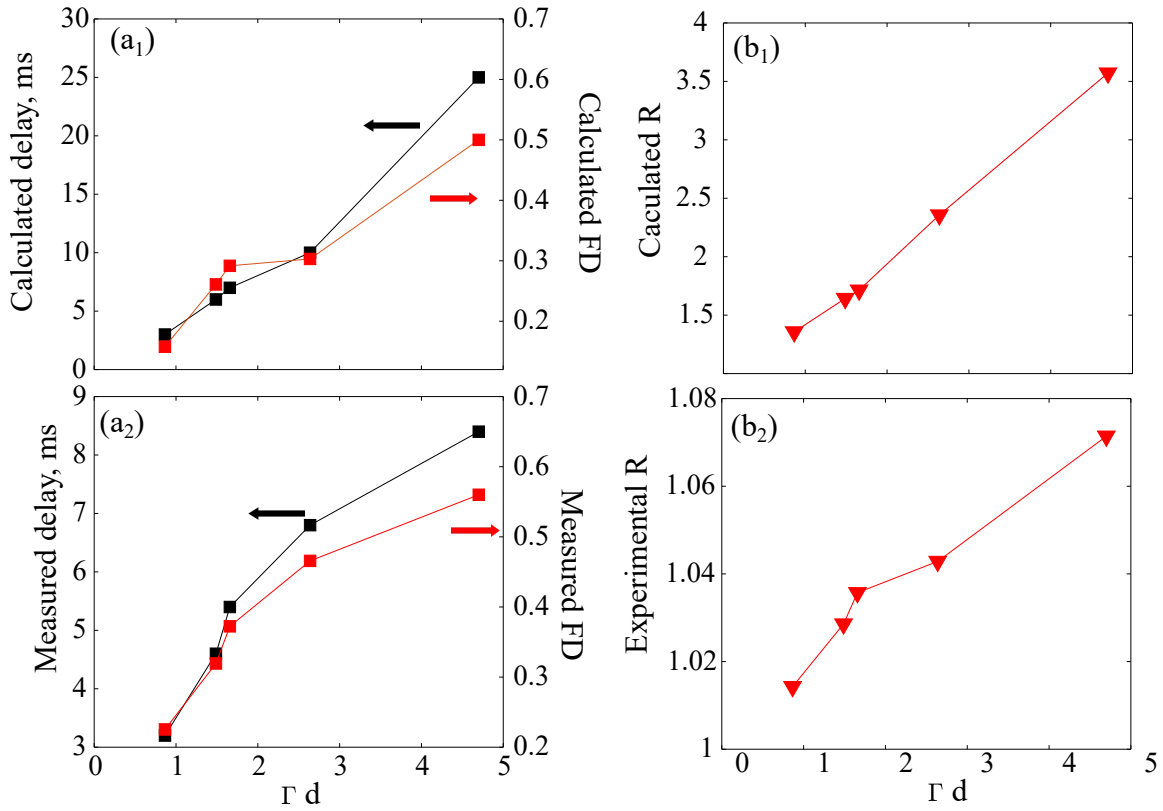

Figure 3.14: Slow light performances as a function of Γd for a full input pulse width at half maximum $t_0 = 14\ ms$ and 0.5 $cm-$ SPS crystal with response time $\tau = 10\ ms$. (a_1) and (b_1) Theoretical results (a_2) (b_1) experimental results. (a_i) Time delay $\Delta\tau$ and fractional delay, (b_i) widening factor $R = t_1/t_0$[15]

theoretically. The maximum FD of the order of 0.5 and 0.56 are respectively obtained theoretically and experimentally for $\Gamma d = 4.7$. The FD values do not exceed the unit: this is due either to the large widening of the output pulse (theoretical case) or to the small values of the delay (experimental case). Indeed, figure 3.14(b_1) shows that the theoretical factor widening factor $(R = t_1/t_0)$ is three times greater than the experimental one (figure 3.14(b_2)).

3.3.2 Delay as a function of the input pulse duration

After characterizing the time delay and FD versus the photorefractive gain for a fixed input pulse width, we choose the optimal angle to allow us to optimize the setup and to get a maximum PR gain Γ. We then analyze the delay and the output pulse shapes for different input pulses durations for $\Gamma = 13\ cm^{-1}$. In figure 3.15, we plot the temporal

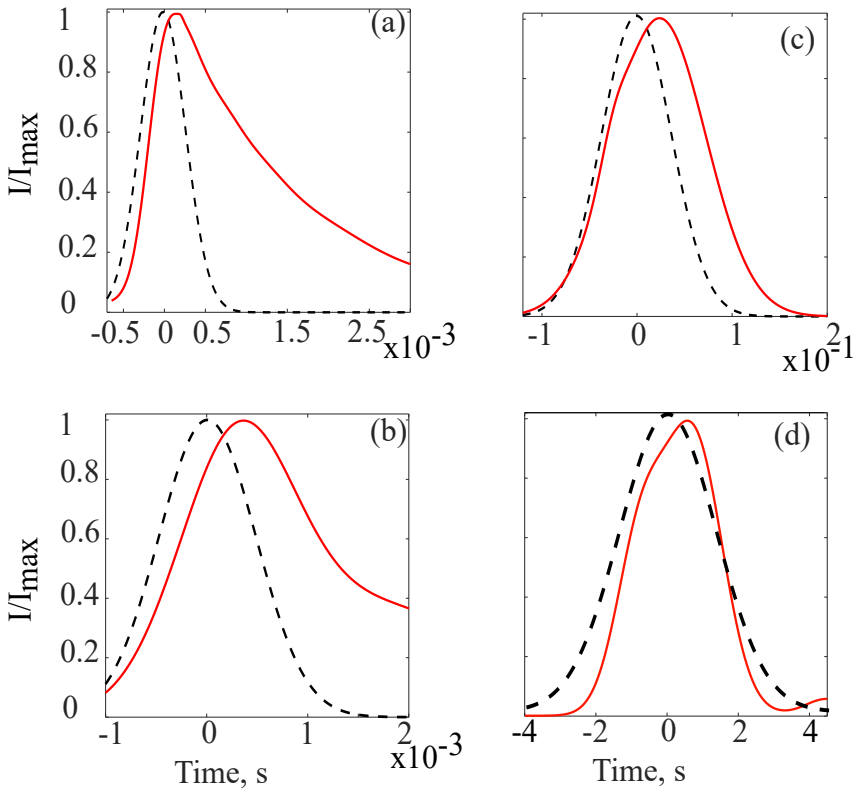

Figure 3.15: Temporal envelopes of the normalized input pulse (dotted line) and output pulse (red line) for four input pulse durations. (a) $t_0 = 600\ \mu s$, (b) $t_0 = 1.2\ ms$, (c) $t0 = 90\ ms$ and (d) $t_0 = 3.5\ s$ corresponding to a delay $\Delta\tau = 96\ \mu s$, $\Delta\tau = 400\ \mu s$, $\Delta\tau = 24\ ms$, $\Delta\tau = 550\ ms$ and to group velocities $v_g = 52\ m/s$, $12.5\ m/s$, $20\ cm/s$, $0.9\ cm/s$, respectively; $\Gamma = 13\ cm^{-1}$, $\Lambda = 1.9\ \mu m$. Crystal: SPS doped Te with $d = 5\ mm$ and response time $\tau = 10\ ms$.

envelopes of the normalized output and input pulses as a function of the time for four input widths. The results of this figure show that **1)** the slow light TWM experiment is able to decelerate a pulse with a duration shorter (figure 3.15(a,b)) or larger (figure 3.15(c,d)) than the response time of the crystal $\tau = 10\ ms$. Pulses with widths of 600 μs, 1.2 ms, 90 ms, and (d) 3.5 s are delayed respectively by 96 μs, 400 μs, 24 ms, 550 ms. **2)** A very small group velocity of $v_g = 0.9\ cm/s$ is measured for an input pulse duration of 3.6 s. **3)** The widening of the output pulse is larger in the case of shorter pulses.

3.3.3 Improved slow light performances using TWM

To analyze the slow light performances, we fix the photorefractive gain to the maximum ($\Gamma = 13\ cm^{-1}$) and we vary the input pulse duration between 0.3 ms and 3.5 s. As

discussed in the theoretical case (section (2.1.2)), figure 3.16 (a) shows that the delay increases with the input pulse width. Also, the results show that shorter pulses smaller than 1 ms (300 μs in this case) are slowed down in the PR SPS crystal. These delay values are larger than those reported in [94] for the same pulse durations. The corresponding group velocity values are plotted in figure 3.16 (b). As shown, v_g decreases with the input pulse duration in the range of 10^4 to 0.9 cm/s.

Figure 3.16 (c) shows the variation of the output pulse duration increase with t_0. We also note a large broadening of the output pulse with a duration smaller or equal to the response time of the SPS crystal.

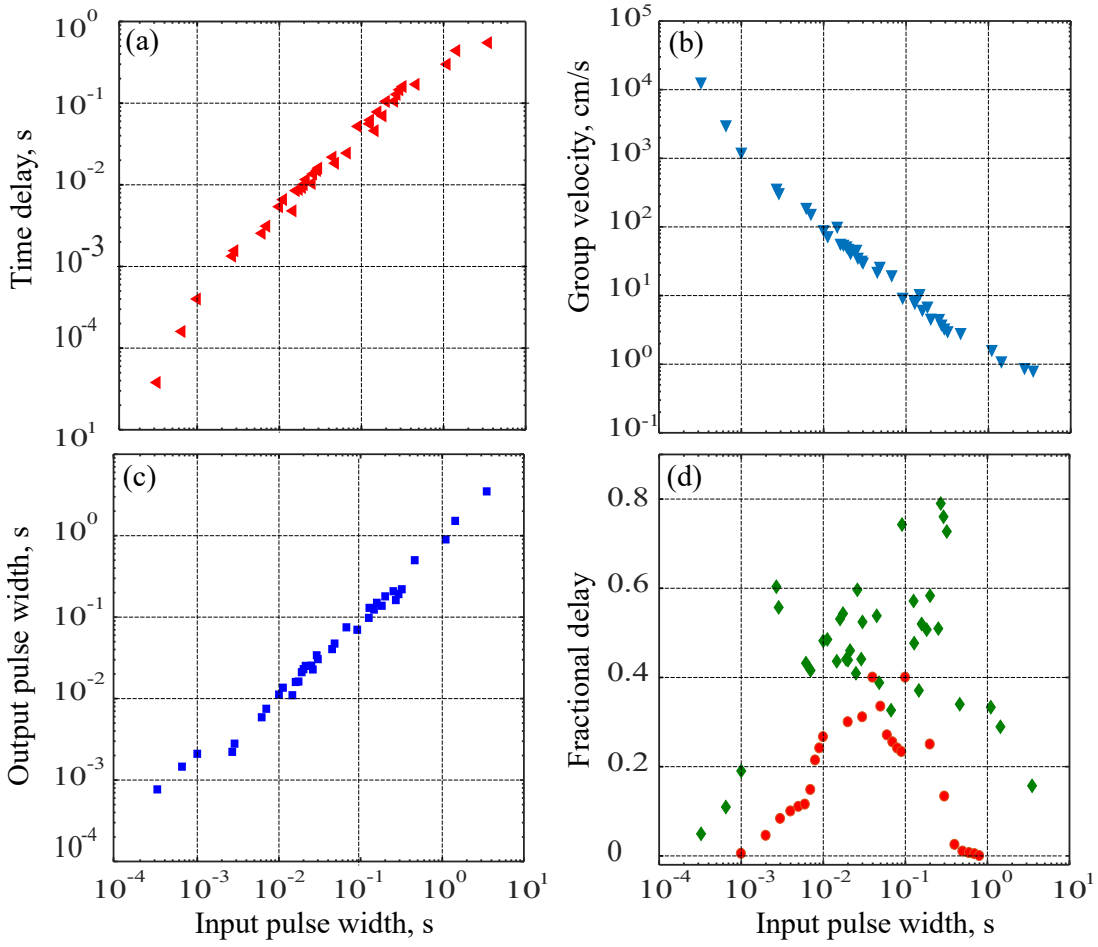

Figure 3.16: Slow light performances as function of the full input pulse à half maximum t_0 for $\Gamma = 13\ cm^{-1}$, period grating $\Lambda = 1.9\ \mu m$ and $d = 5\ m$[12]. (a) delay time, (b) group velocity, (c) full output pulse at half maximum and (d) fractional delay. The red dotted curve plots the values of fractional delay calculated from the time delay values and output pulse durations of the publication [94]

Figure 3.16 (d) plots the fractional delay versus the input pulse duration. We can see that the experimental data of FD are scattered significantly and the value of FD remains of the order of 0.5 in a broad range of input pulse duration. While scanning the input width, a maximum FD of 0.79 is obtained for a pulse duration of 165 ms. From figure 3.16 (d), we note that the maximum values of FD do not correspond to the largest delay. However, they are achieved for pulses durations close to the response time of the crystal $\tau = 10$ ms. The achieved FD is compared to the one reported in Ref. [94] which is plotted in figure 3.16 (d). We note that our results are systematically larger in the full range of pulse durations and typically, the FD is improved by a factor of 2 when compared to the one published in [94].

In the previous subsections, we mentioned that the widening of the transmitted pulse depends on the photorefractive gain values and also on the input pulse duration (figure 3.15). The comparison of the output pulse shape to the input one shows that the TWM in the SPS enables the slowdown of the output pulses without so much distortion, even for a strong gain $\Gamma = 13$ cm^{-1}. In figure 3.17, we plot the measured output pulse duration to those corresponding to the ideal case where $t_1 = t_0$. If we compare the results of both curves, we note that the output pulse duration t_1 measured experimentally is close to t_0. Also, we observe the compression of some pulse when its width is larger than the response time of the crystal.

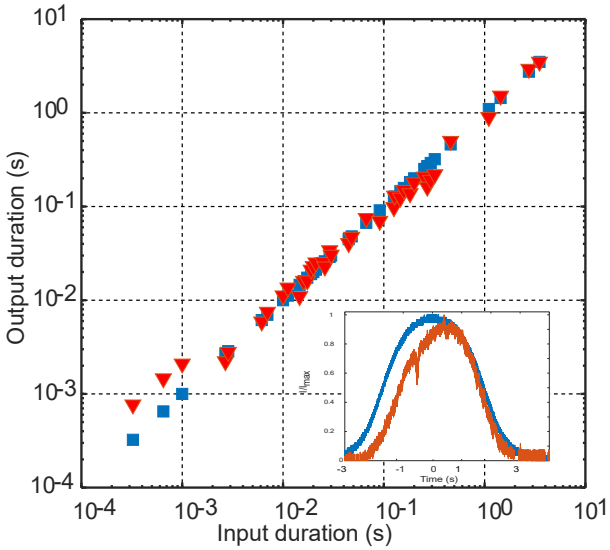

Figure 3.17: Output pulse duration t_1 as a function of the input pulse duration t_0 (red triangle), $\Gamma = 13$ cm^{-1}, $\Lambda = 1.9$ μm, and $\tau = 10$ ms. A curve with blue squares plots the output pulse width with no TWM mixing in the PR crystal and, therefore, $t_1 = t_0$[12]

This small output pulse widening can be explained by **(1)** the value of the photorefractive gain achieved in our PR sample which is smaller than that of $BaTiO_3$ crystal [4]. **(2)** The presence of two charge carrier types (electrons and holes) in SPS that create two index grating: a slow one and a fast one that allows the slowdown (with the output pulse widening) and the speed up (with the output pulse compression) of the light pulses. By increasing the input pulse width or changing the rotation of the crystal c-axis, we can modify the direction of the energy transfer (the sign of the PR gain) and the delayed light pulse can be accelerated. This result is shown in figure 3.18

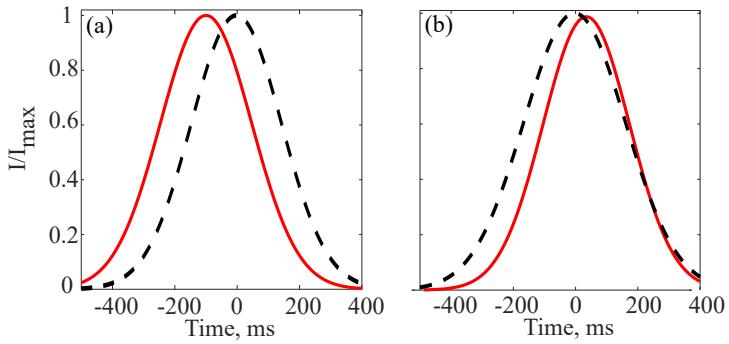

Figure 3.18: Normalized input pulse (dotted line) and output pulse (red line) for input duration $t_0 = 380\ ms$; (a) time advance $\Delta\tau$ =-0.97 ms, (b) time delay $\Delta\tau = 0.35\ ms$ according to the dispersion sign, $\Gamma d = -5, 5$, respectively[12].

3.3.4 Group velocity acceleration and deceleration at 1064 nm

In the previous section, we have given and discussed the results of the slow light in SPS crystal at visible wavelength. These results are interesting but for future applications in telecommunication, it is interesting to slowdown light pulses at infrared wavelengths. Here we demonstrate for the first time that the same SPS crystal is able to decelerate and accelerate the light pulse in the infrared range using the TWM method at room temperature. Similarly to what we did in the visible range, we start our study by measuring the photorefractive gain, the response time of the crystal and then we analyze the slow light performances by analyzing the evolution of the light propagation as a function of the input experimental conditions. Our experiment is similar to the one described above except that in this case, the setup is performed using a Crystal laser LC Model IR$-700-1064$ which is used to generate the pump and the signal beams. The input and the output pulses are detected by two amplified photodetectors New Focus Model 1611 IR. The signal

beam is modulated by a NewFocus Model 4104-IR Amplitude Modulator. For an input intensity $I_0 = 3\ W/cm^2$ and an angle between the propagating beams $\theta = 43°$, we found that the response time of the crystal at 1064 nm is of the order of $\tau = 13\ ms$. This value is determined from the measurement of the TWM gain considering that [85]

$$\Gamma = \Gamma_0(1 - e^{t/\tau}) \tag{3.20}$$

where Γ_0 is the saturation photorefractive gain value.

Figure 3.19 shows that our SPS sample allows doing the two-wave mixing at infrared wavelength $\lambda = 1064\ nm$. The interference of two beams with horizontal polarization in the z-direction of the crystal leads to an output signal amplification. The two-wave mixing gain starts to increase with respect to m, until it reaches a maximum value of 2.5 cm^{-1} for a high ratio m and an input power $P_0 = 187\ mW$. This value is less than the one measured in the visible range (13 cm^{-1}) because of the mobility reduction of the charge carriers at the wavelength of 1064 nm.

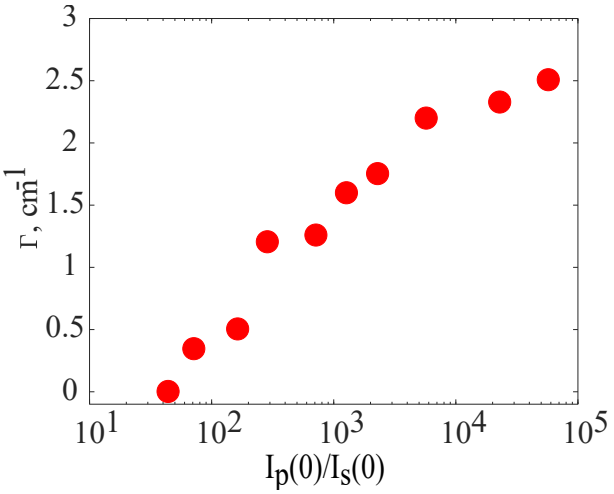

Figure 3.19: Photorefractive gain Γ at infrared wavelength 1064 nm as a function of the ratio between the power of the pump and signal beams. The beams with horizontal polarization interfere in the 0.5 cm-long SPS crystal with an incident angle $\theta = 43°$.

The measurement of the pulse profiles shows that in addition to the amplification, the transmitted pulse is delayed with respect to the input pulse and depending on the crystal c-axis orientation, this delay can be positive or negative. This situation corresponds to the case of slow and fast light respectively. Figure 3.20 plots the normalized input pulse (black line) and output pulse (red line) versus time. For frames (a_1), (a_2) and (a_3), pulses with

durations of $t_0 = 0.04\ s$, $0.22\ s$ and 2.54 are respectively delayed at the crystal output compared to the input pulses. As observed at $638\ nm$, if we rotate the c-axis of the crystal by 180°, the energy transfer changes its direction which modifies the sign of the PR TWM and leads the attenuation and the acceleration of the transmitted pulses. As shown in Figure 3.20(b_1), (b_2) and (b_3) pulses with durations equal to $t_0 = 0.07\ s$, $0.38\ s$ and $0.9\ s$ are accelerated by $-0.008\ s$, $-0.02\ s$ and $-0.038\ s$ respectively.

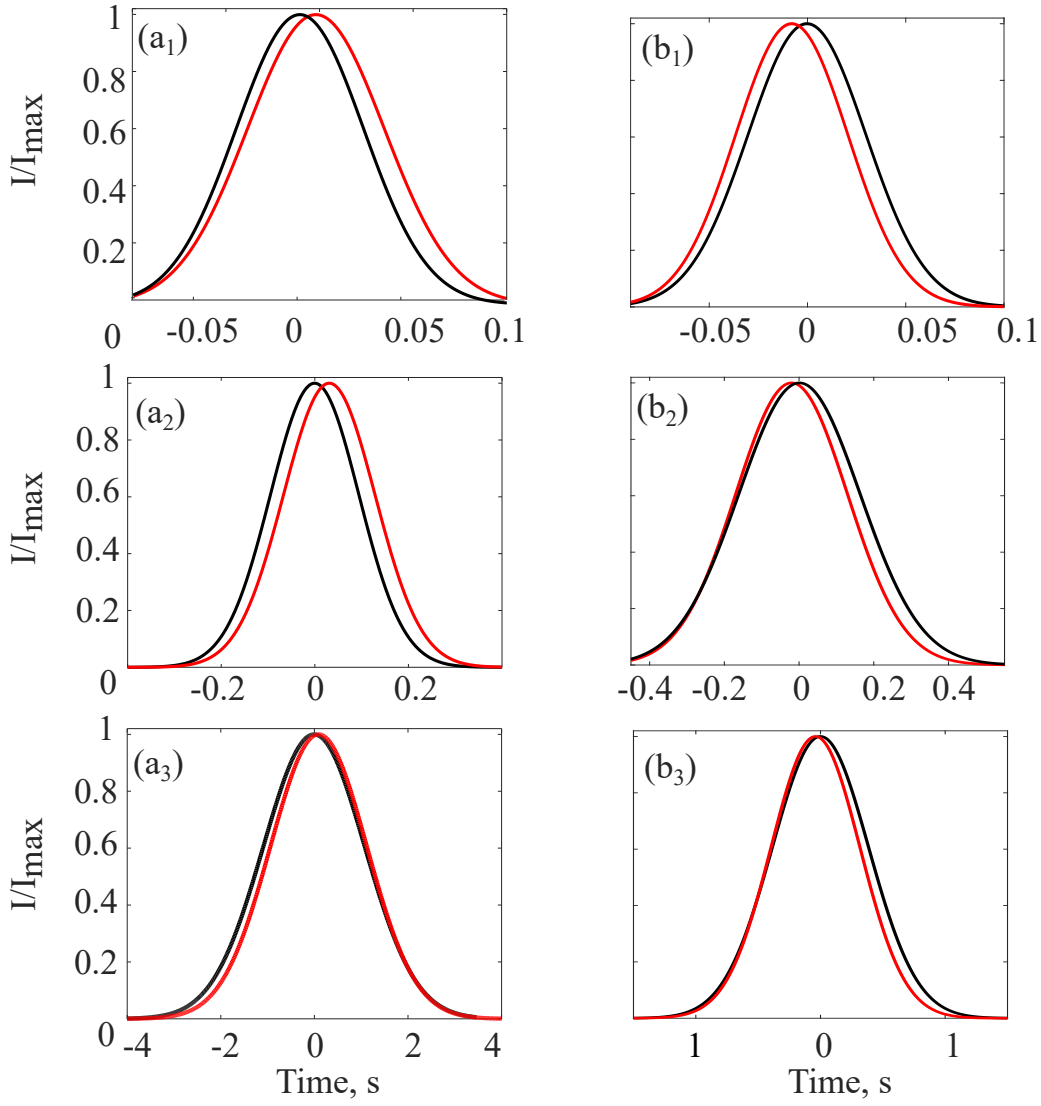

Figure 3.20: Normalized input pulse (black line) and output pulse (red line) versus the time with $\tau = 13\ ms$ and $\lambda = 1064\ nm$. ($a_{1,2,3}$): pulses with durations $t_0 = 0.04\ s$, $0.22\ s$, and $2.54\ s$ are delayed by $\Delta\tau = 0.008\ s$, $0.03\ s$ and $0.06\ s$ respectively with $\Gamma = 2.5\ cm^{-1}$. ($b_{1,2,3}$): the sample is rotated through 180°, pulses with durations $t_0 = 0.07\ s$, $0.38\ s$, and $0.9\ s$ are advanced by $-0.008\ s$, $-0.02\ s$, and $-0.038\ s$ respectively with $\Gamma = -2.5\ cm^{-1}$

Figure 3.21 shows the measured performances obtained in the slow ((a$_1$), (a$_2$) and (a$_3$)) and fast ((b$_1$), (b$_2$) and (b$_3$)) light regimes according to the input pulse duration t_0. As shown in figure 3.21(a$_1$), we note that the delay varies from 0.003 s to 0.075 s and the largest delay value is obtained for $t_0 = 0.7$ s. In the opposite case, the advancement in time A varies from 0.6 ms to 88 ms. From figures (a$_2$) and (b$_2$), we can see that the output pulse duration increases linearly with t_0, which means that the pulses propagate through the PR crystal without strong broadening. The curve of figure 3.21 (a$_3$) shows that the maximum FD value of 0.15 is achieved for an input pulse width of 25 ms.

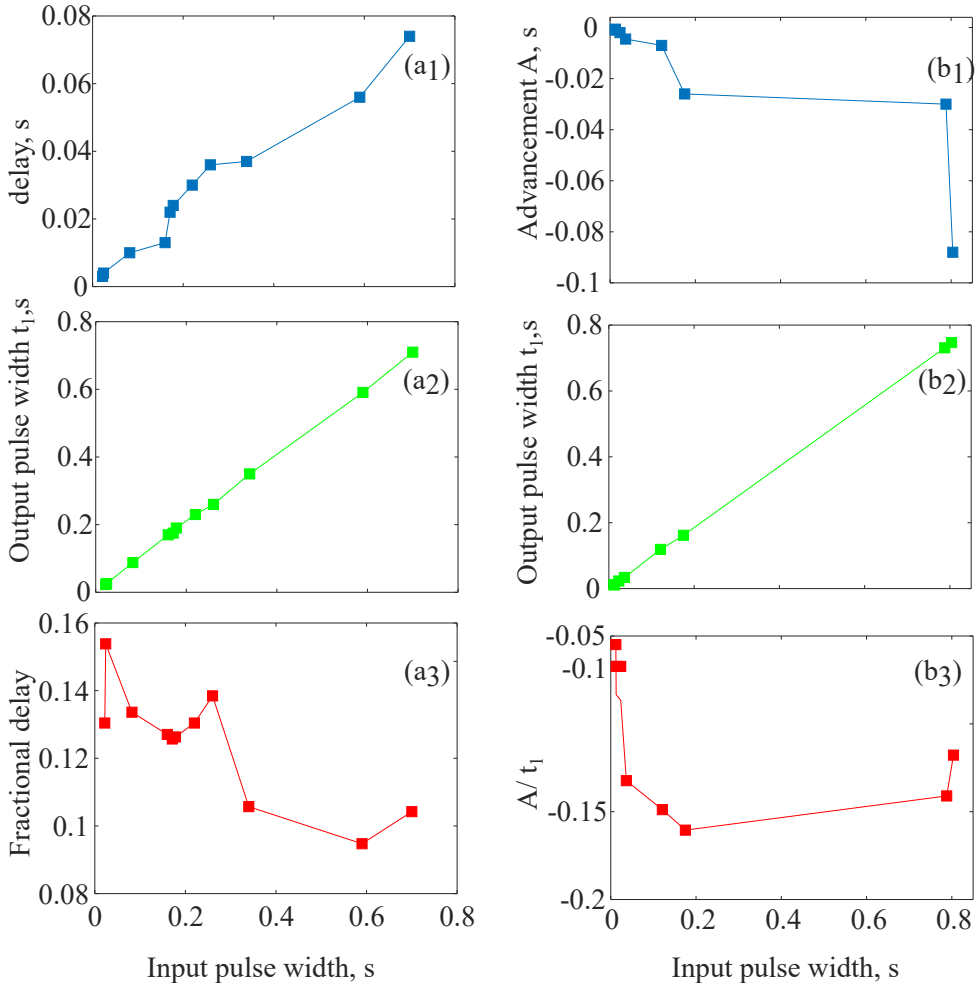

Figure 3.21: Measured pulse delay time $\Delta\tau$ (a$_1$), advancement time A (b$_1$), output pulse duration t_1 (a$_2$, b$_2$), fractional delay FD (a$_3$) and A/t_1 (b$_3$) versus the input pulse duration t_0 for $\tau = 13$ ms and $\lambda = 1064$ nm for slow and fast light respectively. $\Gamma = 2.5$, -2.5 cm^{-1} for the slow and the fast light respectively.

The delay time and the fractional delay obtained at the infrared wavelength are not as good as those achieved in the visible range for the same input pulse durations. These

results can be justified by the fact that the gain value reached at $\lambda = 1064\ nm$ ($\Gamma = 2.5\ cm^{-1}$) is smaller than the one obtained at $\lambda = 638\ nm$ ($\Gamma = 13\ cm^{-1}$). However, the output pulse propagates with less distortion when it is generated by an infrared beam with respect to the last case because the dispersion of the material is less important when the PR gain is smaller.

3.4 Conclusion

To conclude, slow light has been achieved using the TWM process in the SPS crystal at room temperature. First, the light propagation in PR material is theoretically studied. The dependence of the delay time and the output pulse shape on several parameters such as the PR gain, the input pulse duration and the crystal response time are discussed in detail.

This analysis helped us to optimize the PR TWM slow light experiment with as a result a significant slowdown of light pulses with $v_g = 0.9\ cm/s$ and FD close to 0.8. A large photorefractive gain induces a small output pulse distortion in our SPS sample compared to the one measured in other photorefractive crystals such as $BaTiO_3$.

Finally, the performances of the slow and fast light pulses are presented and analyzed according to the gain and the input pulse width at the infrared wavelength. The values of the delay and the fractional delay are slightly smaller than those measured at visible wavelength because of the small value of PR gain. Still, good slow light performances at room temperature are therefore achieved in the PR material in both visible and infrared wavelength ranges.

4

Slow light of dark pulses using TWM method

Contents

In this chapter, we investigate theoretically and experimentally how dark pulses may be decelerated in a PR crystal at room temperature. For this, we propose the use of the same nonlinear process presented in the previous chapter (TWM) in order to slow light with dark pulses.

First, we will present the state of the art of dark pulses and their applications in several domains such as optical solitons and optical telecommunications. Then, we will describe our analytical model that allows getting a clear and simple expression of the temporal envelope of a dark pulse propagating through a PR crystal. As for the Gaussian light pulses (chapter.3), we will present theoretically and experimentally the dependence of the delay and the shape of the output dark pulse as a function of the photorefractive TWM gain and the input pulse duration.

Contrary to Gaussian light pulses, we will show that dark pulses offer the possibility to generate more important delays, larger than the input pulse duration. Finally, we will close this chapter with a comparative study of the performances obtained with Gaussian and dark pulses. We will then discuss and analyze the results in detail.

The results of this chapter have been published in [16]

4.1 Dark pulse and their applications

A dark pulse has the form of a density dip resulting in a reduction in the intensity of electromagnetic radiation. Dark pulses have been experimentally and theoretically studied in the last years. It is reported that a dark pulse presents more advantages compared to a bright one: (1) it can be more stable and less sensitive to noise in optical fiber transmissions [104–106]. (2) It is less susceptible to scattering than a bright pulse. These interesting properties of dark pulses allow a wide scope of applications such as long-optical transmission and the design of new dark pulsed lasers. Note that the dark laser is a good candidate for telecommunications: indeed, the data can be encoded in dark pulses in the same way as in bright pulses but can travel long distances without being distorted or degraded.

Since its first observation in optical fibers [107], researchers have found that dark pulses cannot be easily obtained and involved very complicated experimental conditions. However, the generation and the propagation of the dark pulse has been studied extensively and has

been demonstrated with several methods. For example, femtosecond and nanosecond dark pulses have been generated by passive spectral filtering in a single-mode fiber [108–110], and in a quantum dot laser [111]. In other work, the dark pulses have been generated from continuous-wave beam by means of an electrooptic modulator such as Mach–Zehnder [112, 113], phase-modulated optical loop mirror (MOLM) [114] or guided-wave electrooptic modulators [115].

In addition to long-distance optical communications [104], the dark pulse has been attracting great interest for other applications. 1) It has been used to study the propagation and the interaction of dark solitons in an optical fiber [105, 106] and in Bose-Einstein condensate [116]. 2) Also, it has been demonstrated that the femtosecond pulse that appears in the generated x-rays can be used for time-resolved spectroscopy [117]. 3) D. Meshulach et al. have shown that the use of a dark pulse allows the control of two-photon transitions in Caesium (Cs) [118]. 4) Other works demonstrated the generation of dark pulse combs, dark pulses in the normal-dispersion microresonators with mode-interaction assisted excitation, and mode-locking transitions [119]. 5) By the end, the use of dark pulses has been recently suggested in the study of light propagation in plasmas [36, 120, 121].

In the following part, we will focus on the more important application fields of dark pulses such as solitons, optical telecommunications and slow light systems.

Solitons:

The dark pulse studies started and they were theoretically predicted in the field of Bose-Einstein condensates in 1971 [122] and in optical fiber in 1973 [123]. The first experiments involving the generation and the propagation of the dark soliton were reported in 1988 by Weiner et al. [108]. As shown in figure 4.1 (a), their experiment was performed by a colliding pulse−mode−locked dye laser at 620 nm wavelength in $1.4m$ length of single−mode optical fiber. A spatial mask and a standard grating were used to obtain an anti-symmetric input pulse. Figure 4.1 (b) shows the experimental results obtained for an odd-symmetry dark pulse for different power levels. The input pulse in figure 4.1 (b_1) is characterized by a central hole with a full width at half maximum of 185 fs and a background of 1.76 ps. From Figures 4.1 (b_2)−(b_5), we note that the shape of the dark pulse changes as a function of the input peak power. For the lowest power, the dark pulses propagate without distortion through the optical fiber.

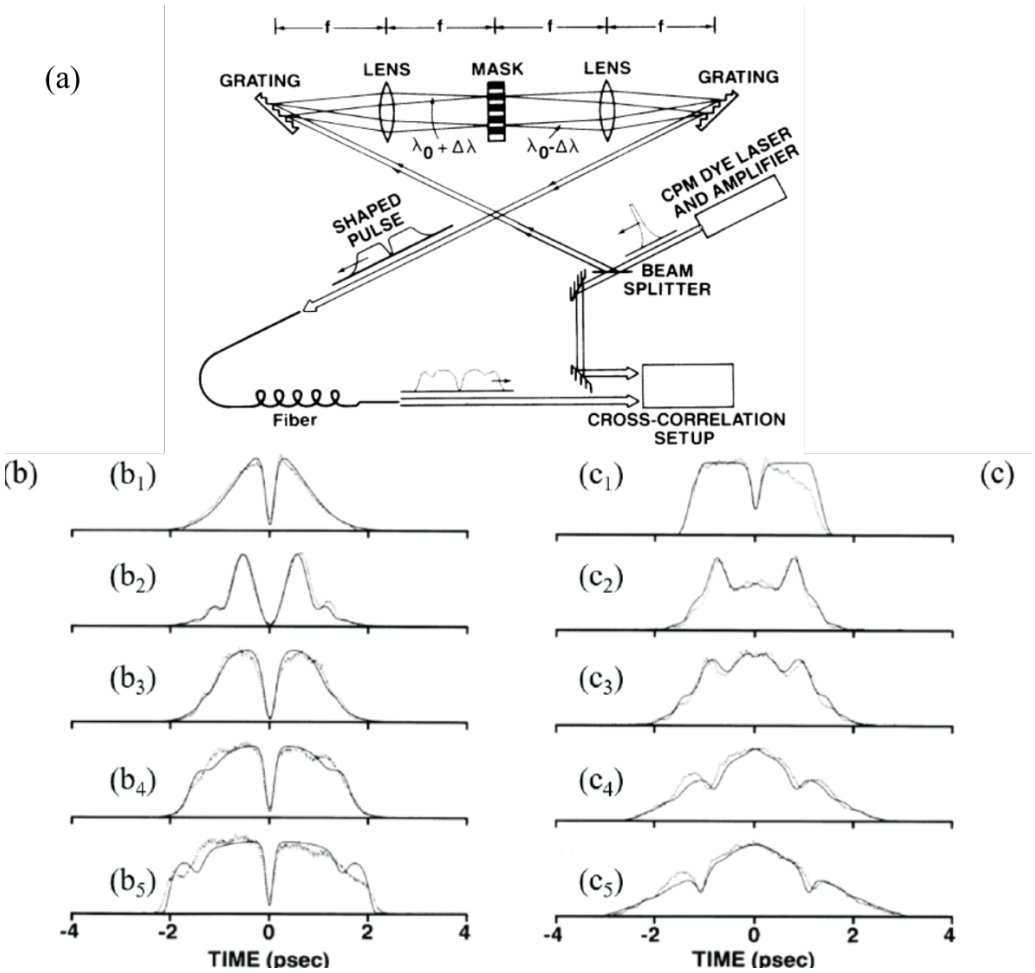

Figure 4.1: (a) Experimental setup proposed by Weiner et al. [108] with f is the lens focal length .Calculated (solid line) and measured (dotted line) for the odd-symmetry dark pulse (b) and even-symmetry dark pulse (c). (b_1) and (c_1 are the input dark pulses. (b_2)−(b_5) and (b_2)-(b_5) are Pulses emerging from the figure for peak input power (b_2) 1.5, (b_3) 52.5, (b_4) 150, (b_5) 300, (c_2) 2.5, (c_3) 50, (c_4) 150 and (c_5) 285 W.

In the second part, they use a different spatial mask to generate even-symmetry dark pulses. The experiment results in this case, are presented in figure 4.1 (c). The background is distorted and the dark pulse is broadened for low power. By increasing the input peak power, they observe the formation of two holes separated by a certain time, which changes with the value of the power. For example, for a 285 W peak power, the holes are separated by 2.3 ps. Analyzing all these results, the authors conclude that the odd-symmetry dark pulse propagates in the optical fiber without any distortion as what is called black soliton and the even dark pulse splits into two gray solitons. Since this study, various other methods have been used for generating single or several dark solitons [113,

124]. For example, in 1995, M. Nakazawa and K. Suzuki [113] proposed a new scheme for generating a pseudorandom data train of dark solitons by using an AND gate and T-flip-flop circuits.

Optical communications: as mentioned in the introduction, the dark soliton can be used for telecommunications. The studies of the propagation of dark pulses over distances relevant to telecommunications were first reported in 1993 by Emplit et. al [125]. They numerically simulated and experimentally observed propagation of picosecond odd-symmetry dark pulses over 1-km single-mode fiber at 850 nm wavelength. The results of their study are presented in figure 4.2. The temporal intensity and spectral density profiles of the input and output pulses show that the dark pulse propagates without distortion at the power corresponding to the fundamental dark pulse. Also, the measurement results are in quantitative agreement with numerical simulations.

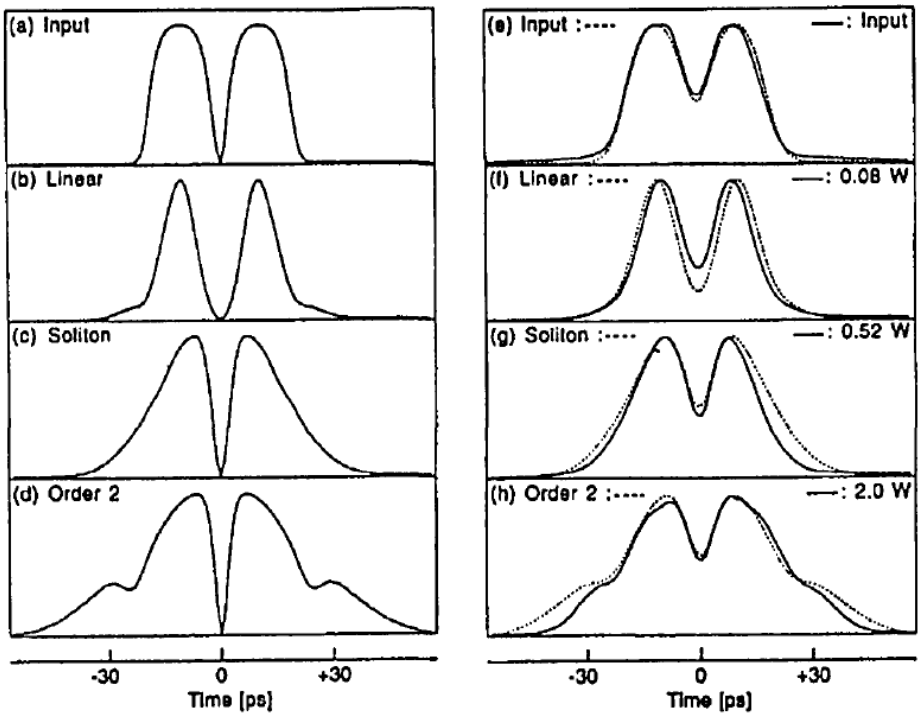

Figure 4.2: Numerical simulations of pulse intensity profiles which propagate through 1-km optical fiber at 850 nm. (a) Input odd-symmetry dark pulse with a duration of 5.3 ps. (b)-(d) are the numerical results and the solid line in (e)-(h) are the experimental results [125].

Then, in 1995, M. Nakazawa and K. Suzuki have shown the transmission of dark soliton data trains over 1200-km length optical fiber. [113]. In their work, they used a one-bit-

shifting technique with a Mach-Zehnder interferometer to convert the dark pulse into a non-return-to-zero (NRZ) signal.

Slow light systems in plasmas: the dark pulses are also investigated in slow light systems including in plasmas [120] and insulator-insulator-metal metal plasmonic waveguides [121]. In [121], they proposed an analytical model for describing the propagation of temporal dark solitons in the insulator-insulator-metal metal geometry. Using this model, they have shown that a 10 $Gbit/s$ signal at $\lambda = 1540\ nm$ can be delayed by 10 ns. Also, they have demonstrated that the dispersion of the transmitted signal can be compensated by using Kerr dielectrics and dark solitons.

4.2 Theoretical study of slow light using dark pulse

In this section, we study theoretically the slow light principle induced by the TWM between a continuous pump and a dark pulse. We report an analytical model that describes a dark-pulse propagation through a photorefractive media. The delays observed when a dark pulse propagates in the nonlinear medium are analyzed as a function of the different input parameters: gain, propagation distance and response time. For the calculation, we consider an input dark pulse with the electric field $A(0,t)$ given by:

$$A(0,t) = \sqrt{A_0^2 - A_0^2 exp\left(-\left(\frac{t}{T_0}\right)^2\right)} \tag{4.1}$$

were A_0 and T_0 are respectively the amplitude and input $1/e$ width of the input pulse intensity (section (3.1.1)). Figure 4.4 plots an example of the dark pulse intensity $I(0,t)$. As shown, this pulse is presented as a Gaussian hole that is characterized by a localized reduction in intensity compared to a more intense background.

For simplicity of the next calculations, let us use the Taylor expansion to rewrite the expression of $A(0,t)$ as follows:

$$A(0,t) = A_0\left(1 - \sum_{n=0}^{\infty} a_n exp\left(-2n\left(\frac{t}{T_0}\right)^2\right)\right) \tag{4.2}$$

where a_n is given by:

$$a_n = \frac{(2n)!}{2^{2n}(2n-1)(n!)^2} \tag{4.3}$$

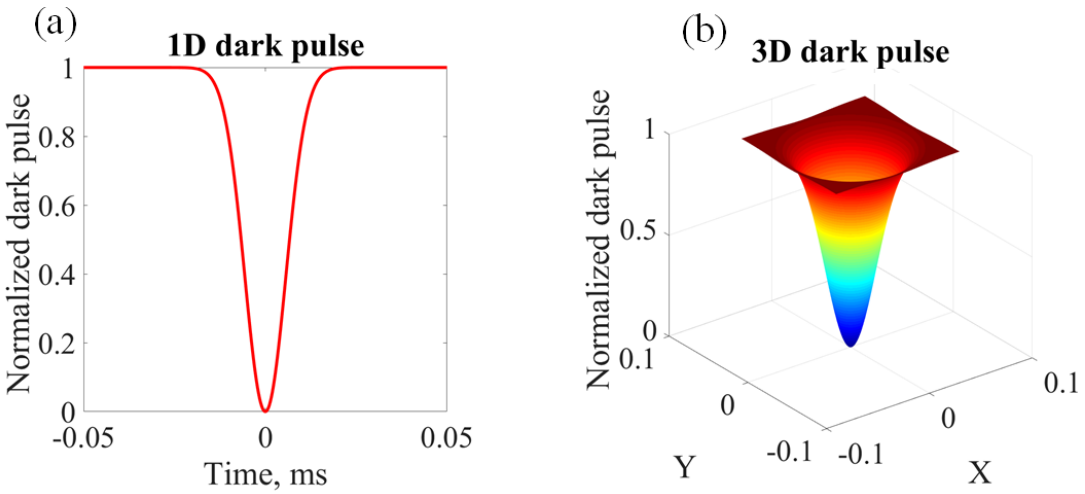

Figure 4.3: Normalized dark pulse intensity, (a) 1D, (b) 3D.

As for the Gaussian pulse, the interference of the continuous pump wave and the input dark pulse $A(0,t)$ in the PR crystal with thickness d can generate a PR TWM gain Γ, so the amplification of the output pulse can be written as:

$$A(d,\omega) = A_\omega(0)e^{gf_\omega} \tag{4.4}$$

where $g = \Gamma d$ is the dimensionless factor referred to as the photorefractive coupling strength, f_ω is the characteristic response function of the SPS crystal and $A_\omega(0)$ is the Fourier transform of $A(0,t)$ defined as:

$$A_\omega(0) = A_0\delta(\omega) - A_0\frac{T_0}{2\sqrt{\pi}}\sum_{n=0}^{\infty} a_n exp\left(-\frac{n\omega^2T_0^2}{2}\right) \tag{4.5}$$

By replacing the expression $A_\omega(0)$ in equation 4.4, we will get:

$$A(d,\omega) = A_0\delta(\omega) - A_0\frac{T_0}{2\sqrt{\pi}}\sum_{n=0}^{\infty} a_n exp\left(-\frac{n\omega^2T_0^2}{2}\right)e^{gf_\omega} \tag{4.6}$$

By using the inverse Fourier transform, the amplitude of output dark pulse $A(d,t)$ is given by:

$$\begin{aligned} A(d,t) &= A_0\int_{-\infty}^{\infty}\left(\delta(\omega)e^{gf_\omega}\right)d\omega - \\ &\quad A_0\frac{T_0}{2\sqrt{\pi}}\sum_{n=0}^{\infty} a_n\int_{-\infty}^{\infty} e^{-0.5n\omega^2T_0^2+gf_\omega-i\omega t}d\omega \end{aligned} \tag{4.7}$$

The numerical calculations of this equation demonstrate that the two-wave mixing between the dark pulse and the continuous pump allows both the amplification and the deceleration of the transmitted pulse. In the case of the dark pulses, the delay is defined as the time shift between the minimum of the output dark pulse and the input one.

Now, we analyze the profiles of the normalized pulse intensities and compare the results to those calculated for the Gaussian pulses. For this, we use the expression of the output signal given by equation 3.3 (section.3.3.1) and equation 4.7 to plot respectively the intensities of bright (Gaussian) and dark pulses. Figure 4.4 plots the results for a full input width at half maximum $t_0 = 60\ ms$ and $|\Gamma d| = 6.62$. By analyzing the results, we note that the minimum of the output dark pulse in Figure 4.4(b) is more delayed than the output bright pulse maximum (Figure 4.4(a)). Indeed, for the same input pulse duration, the bright and the dark pulses are respectively delayed by $\Delta\tau = 67\ ms$ and $\Delta\tau = 77\ ms$ at the output of the PR crystal.

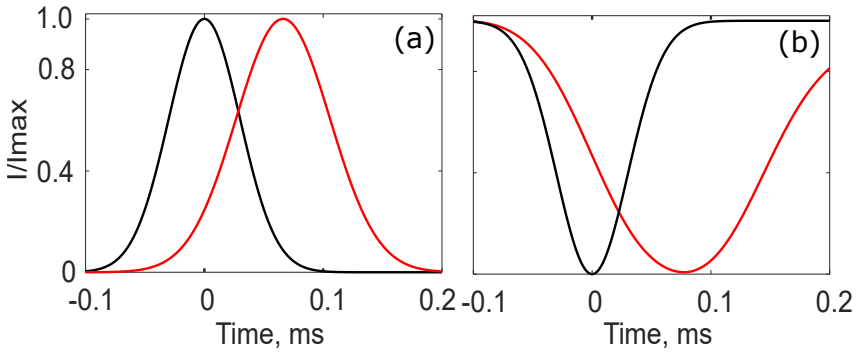

Figure 4.4: Normalized input (black line) and output (red line) pulses intensities as a function of the time for an input full pulse width at half maximum $t_0 = 60\ ms$, $|\Gamma d| = 6.62$ and response time $\tau = 10\ ms$. (a) time delay $\Delta\tau = 67\ ms$ for the Gaussian light pulse. (b) Time delay $\Delta\tau = 77\ ms$ for the dark Gaussian pulse [16].

In order to study the dependence of the optical delay of the dark pulse on the photorefractive gain, second series of calculations was performed with three different values of $|\Gamma d|$. Figure 4.5 plots the temporal envelopes of the input and output intensities with for input pulse duration $t_0 = 60\ ms$ and $|\Gamma d| = 5,\ 8,\ 10$. As for the Gaussian pulses, we can see that both the dark pulse delay and the output pulse duration can be changed varying the PR gain. The corresponding transmitted pulse delays are $\Delta\tau = 50,\ 80,\ 100\ ms$ respectively, for $|\Gamma d| = 5, 8, 10$. Also, when we increase the PR gain, we note a broadening of the output

dark pulse. Indeed, for $|\Gamma d| = 5$, 8 and 10, the full width at half maximum of the output dark pulse becomes $t_1 = 2t_0$, $t_1 = 2.2t_0$ and $t_1 = 2.5t_0$ respectively.

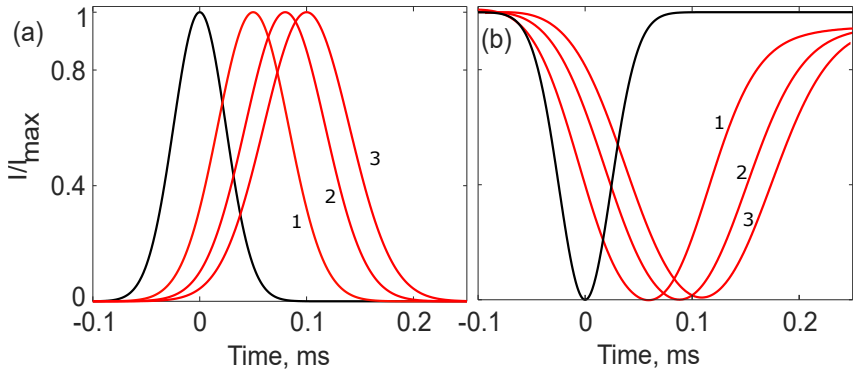

Figure 4.5: Normalized input (black line) and output (red line) pulses intensity as function of the time, for an input pulse duration $t_0 = 60\ ms$, $\tau = 10\ ms$ and for three values of Γd; (1) $|\Gamma d| = 5$, (2) $|\Gamma d| = 8$ and $|\Gamma d| = 10$. (a) Time delay $\Delta\tau = 50, 80, 100\ ms$ for the Gaussian light pulse. (b) Time delay $\Delta\tau = 58, 88, 106\ ms$ for the dark pulse [16].

4.2.1 Theoretical results and discussions

Next, we examine the evolution of the dark pulse delay as a function of the PR gain but also of different other parameters such as the propagation length and the response time of the photorefractive material. The curves of figure 4.6 are obtained from numerical simulations of the equation 4.7 for a dark pulse with an input width of $t_0 = 50\ ms$. In this case, we varied the PR gain value and then we changed either the propagation length (crystal thickness) or the response time of the crystal. As shown in figure 4.6, the optical delay of the dark pulse varies strongly with the PR gain. When the photorefractive gain is low, it is clear that the output dark pulse undergoes a very small optical delay. On the other hand, for an important gain, the delay becomes larger.

Figure 4.6 (a) shows the evolution of the dark pulse delay as a function of the gain for a crystal response time of 10 ms and for different thicknesses extending from 0.5 cm to 2 cm. It is obvious that increasing both the propagation length d and the PR gain Γ allows to improve the coupling strength Γd, hence increasing the delay value of the output pulse. On the other hand, to achieve wide delays, it is important to use a long crystal (long propagation distance) or a crystal that can generate a high PR gain.

To finalize this study, figure 4.6 (b) shows the variation of the delay as a function of the gain for different response time values. In this case, we consider that the response time of the crystal is independent of the input pulse duration. We will see in the chapter (6) that this model and the one used for bright pulses with the TWM in the continuous regime are no valid when the response time of the crystal changes according to the pulse duration. As shown for the bright pulses (figure 3.7, section (3.1)), the results show that the value of the response time of the PR crystal can control the value of the delay.

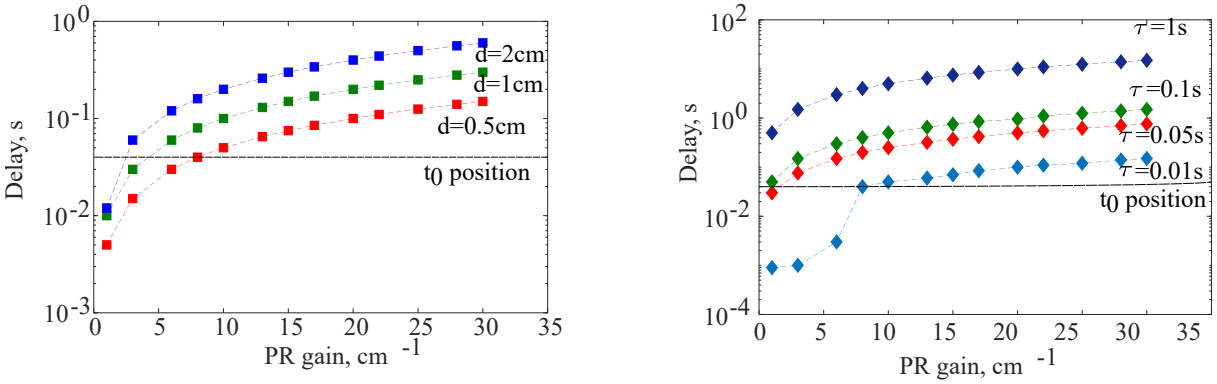

Figure 4.6: Evolution of the delay of a dark pulse with a duration of $t_0 = 50\ ms$ as a function of photorefractive gain Γ (a) Time delay for different values of the propagation length $d = 0.001$, 0.008, 0.02, 1 and 2 cm, with $\tau = 0.01\ s$. (b) Time delay for different response time values $\tau = 0.01$, 0.05, 0.1 and 1 s, with $d = 0.5\ cm$.

From figures 4.6 (a) and 4.6 (b), we note that if $\Gamma d > t_0/\tau$, the delay can be larger than the input pulse width t_0 and its value can be estimated as $\Delta\tau = \Gamma d\tau$. For example, for $\Gamma = 30\ cm^{-1}$, the delay reaches a significant value of 15 s in 0.5-cm PR crystal with a response time of 10 ms.

For our experimental work on slow light with dark pulses, we will use a crystal with a response time of 10 ms and a thickness of 0.5 cm and able to generate a photorefractive gain that can reach 13 cm^{-1}. This crystal is the same as the one used in the TWM experiment presented in the previous chapter.

4.3 Experimental study

In this section, we present the experimental studies that demonstrate the possibility to slowdown dark pulses using the TWM setup presented in figure 4.7. This setup is

performed with a 0.5-cm SPS crystal and a red laser at 638 nm. It is similar to the one used in chapter 3. The electro-optic amplitude modulator (EOM) can be used to generate a Gaussian or dark pulse by changing the electric signal phase. The phase difference between a dark and a bright pulse is 180°.

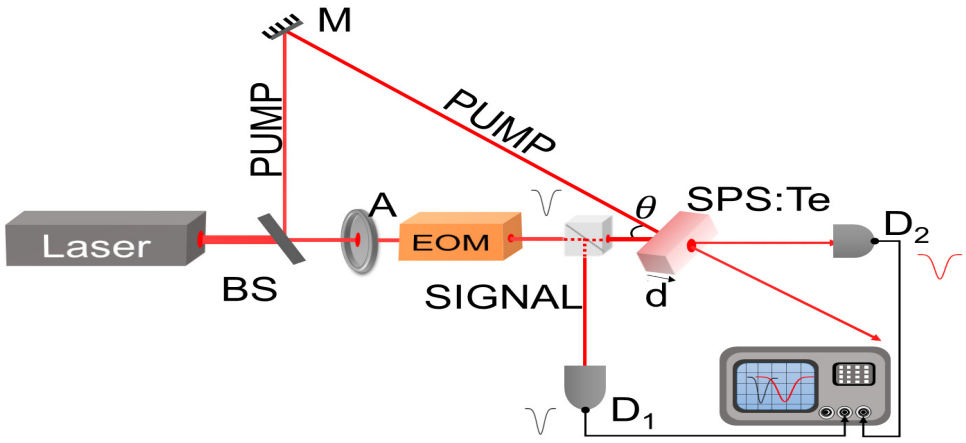

Figure 4.7: Experimental setup of the beam coupling between a dark pulse and a continuous pump in the PR SPS crystal with a thickness $d = 0.5\ cm$ and a response time equal to 10 ms ; BS is the beam splitter, A is the attenuator, EOM is the electrooptic amplitude modulator, $D_{1,2}$ are the detectors, M is the mirror, θ is the incidence angle between the pump and the input dark pulse [16].

By using the device of figure 4.7, it is shown that the minimum of the output dark pulse (red line) that propagates through the SPS crystal is delayed in time by comparison to the minimum of the reference (black line). As demonstrated in the case of Gaussian pulses, this delay is therefore resulting from the wave mixing between the pump and the dark pulse. In the following parts, we will analyze this delay as a function of the input pulse duration and the photorefractive gain. Also, the conditions allowing to have delays larger than the pulse duration will be discussed.

4.3.1 Dark pulse transmission through the SPS crystal: delay and distortion

In order to validate the analytical predictions about the influence of the input pulse duration on the output dark pulse delay, we measured it for two different FWHM, $t_0 = 10$ ms and $t_0 = 480$ ms. As a preliminary result, figure 4.8 illustrates the normalized profiles of the dark pulse at the input and output crystal faces for these two pulse durations. The experimental results are achieved using the TWM process with $\Gamma d = 5$: this is measured

for low dark pulse intensity I_{dark} with a ratio $I_p/I_{dark} = 7.10^3$. For a pulse duration FHWM, $t_0 = 10.3\ ms$ (figure 4.8 (a)) close to the response time of the SPS crystal τ ($\tau = 10\ ms$), the dark output pulse has a duration $t_{out} = 15.7\ ms$ and it is delayed by $\Delta\tau = 7.9\ ms$. From figure 4.8, we note that the delay increases with t_0. A delay value $\Delta\tau = 146\ ms$ is measured for a pulse duration $t_0 = 480\ ms$.

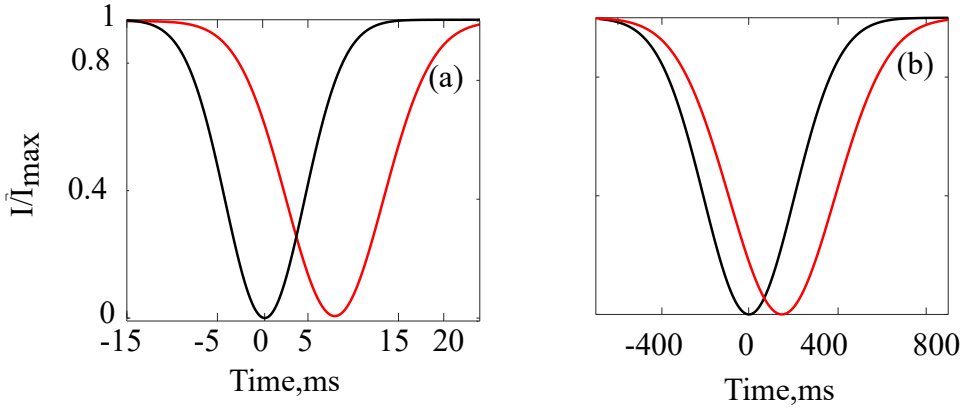

Figure 4.8: Normalized input (black line) and output (red line) pulse intensities as a function of the time for $\Gamma d = 5$ and $\tau = 10\ ms$, (a) Time delay $\Delta\tau = 7.9\ ms$ for an input pulse duration $t_0 = 10.3\ ms$; output pulse duration $t_{out(FHWM)} = 15.7\ ms$, (b) Time delay $\Delta\tau = 146\ ms$ for an input pulse duration $t_0 = 480\ ms$; output pulse duration $t_{out(FHWM)} = 570\ ms$.

4.3.2 Experimental performances as a function of gain

Now, we are will study the experimental performances of the slow dark pulses process in a PR SPS crystal as a function of the TWM gain. A 10-ms pulse injected into the crystal is delayed with a dependence on the value of the photorefractive gain. Figure 4.9(a) presents the normalized input and output pulse intensities for two experimental values of the coupling strength: $\Gamma d = 2$ and $\Gamma d = 2.9$. For $\Gamma d = 2$, we note that the dark pulse propagates in the crystal without any broadening, however, the output pulse undergoes a widening of about 3 times its initial duration for $\Gamma d = 2.9$. From figure 4.9(b), we can see that the delay can present a strong variation as a function of gain. Thus, for a 10-ms pulse, the delay can vary from 3 to 16.5 ms for Γd varying from 2 to 4.47. As it is shown, beyond $\Gamma d = 2.4$, the measured delay $\Delta\tau$ is larger than the dark pulse duration t_0. The delays obtained with dark pulses are better than those measured for the Gaussian pulse with the same width.

The curve in figure 4.9(c) shows the variation of the output pulse duration as a function

of Γd. Note that there is a strong dependence of the gain on the output pulse widening, meaning that a slight change in Γd will change the duration of the transmitted pulse. For example, for $\Gamma d = 4.6$, the output pulse duration $t_{out(FHWM)}$ changes from 10 ms to 28 ms. Although the delay values are more important than the input dark pulse duration for large gain values, we notice that the fractional delay remains less than 1. Indeed, as illustrated in figure 4.9(d), the FD varies from 0.3 to a maximum value of 0.6. Its value increases with the delay until reaching the maximum at $\Gamma d = 2.4$ and decreases with a large widening of the output pulse.

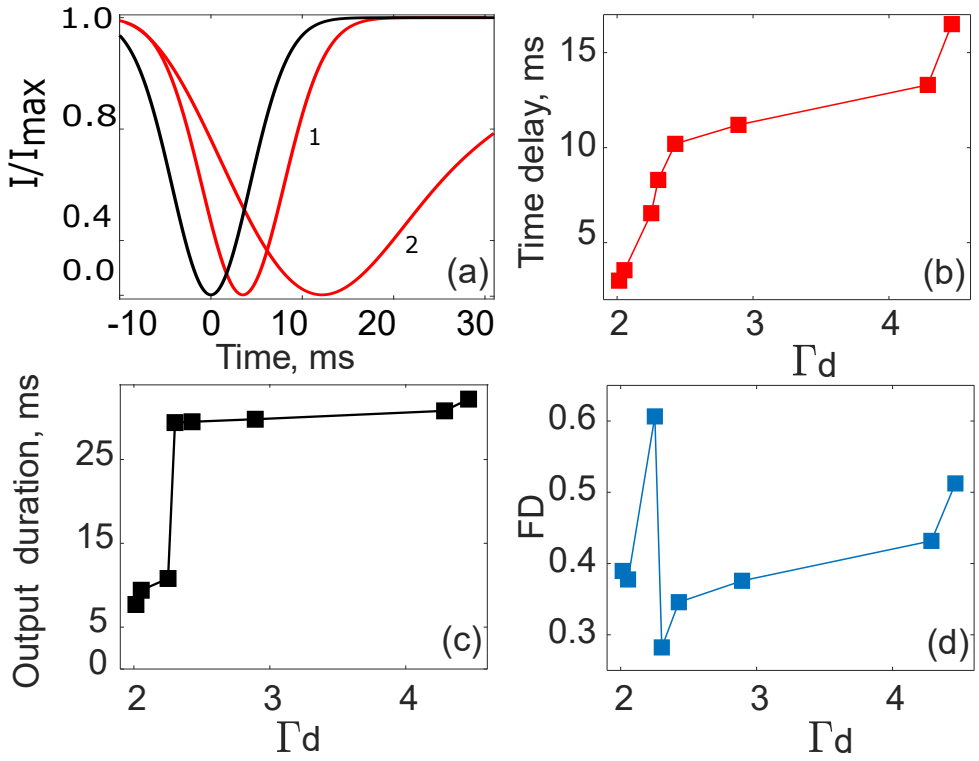

Figure 4.9: Performances of the deceleration of the dark pulse as a function of the coupling strength Γd. a) Temporal envelopes of the normalized input (black line) and output (red line) intensities for input pulse duration $t_0 = 10\ ms$, $\tau = 10\ ms$ and $\Gamma d = 2$ (1) $\Gamma d = 2.9$ (2). (b) Time delay $\Delta\tau$ as a function of Γd. (c) Output pulse duration at half maximum $t_{out(FHWM)}$ as a function of Γd. (d) Fractional delay FD as a function of Γd [16].

4.3.3 Optical delays larger than pulse durations

In section (4.3.1), we presented some experimental results of the performances of dark pulse deceleration as a function of PR gain. We have shown that the improvement of the

photorefractive gain is a first way for achieving larger delay than the input dark pulse width. In the following, we will see that in addition to the gain, it appears that the choice of the pulse duration is a second key parameter to reach a large delay. To illustrate this in detail, figure 4.10 represents a case where the measured delay $\Delta\tau$ is larger than the input dark pulse duration: a pulse with a duration $t_0 = 23.5\ ms$ is delayed by $\Delta\tau = 28\ ms$ for $\Gamma d = 5$.

Varying both the coupling strength Γd and the input pulse duration t_0, we can conclude that in the slowing down of dark pulses, quite large values of delay are achieved for a large gain and for rather small input pulse width close to the response time of the PR crystal. A large coupling strength and rather small input pulse width (close to the response time of the PR crystal) allows achieving large delay values with a corresponding FD equal to 1.

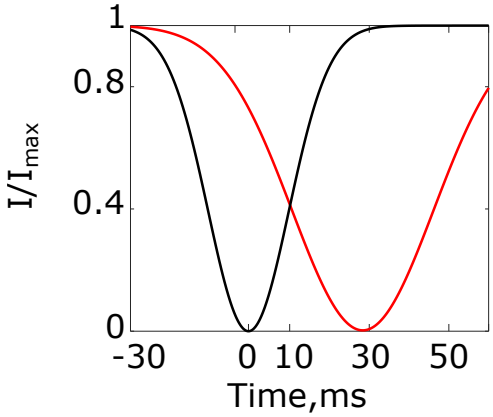

Figure 4.10: Temporal envelopes of the normalized input (black line) and output (red line) pulses for $\Gamma d = 5$, dark pulse FHWM $t_0 = 23.5\ ms$ is delayed by $\Delta\tau = 28\ ms$ in the PR SPS (with response time is $\tau = 10\ ms$).

4.3.4 Performances according to the input pulse durations

In order to complete the experimental analysis, we performed a series of measurements of the delay and FD by varying the input pulse duration over a wide range, from 1 ms to 1 s pulse durations. The performances of the delay τ, the output dark pulse duration (FWHM) t_1 and the corresponding fractional delay FD are plotted in figure 4.11 for $\Gamma d = 5$.

From figure 4.11(a), we can see that the values of the delay increase for the short pulses FHWM $t_0 < 250\ ms$, then decrease to zero. A maximum delay value of 156 ms

corresponding to the group velocity $v_g = 3.2\ cm/s$ is achieved for $t_0 = 240\ ms$. The full input pulse widths at half maximum close to the crystal response time allow achieving delays equal or larger than t_0. Delays $\Delta\tau = 11\ ms$, $\Delta\tau = 12\ ms$, $\Delta\tau = 26\ ms$ and $\Delta\tau = 28\ ms$ are measured for $t_0 = 11\ ms$, $t_0 = 12\ ms$, $t_0 = 22\ ms$ and $t_0 = 23.5\ ms$ respectively. For larger t_0 higher than 880 ms, the delay values become negatives which causes the acceleration of the output dark pulse. As discussed in section (3.3.3), the light pulse acceleration can be also observed with the dark pulse because of the self-compensation response time of the SPS crystal. In our case, the advance time is measured for a dark pulse duration greater than 800 ms.

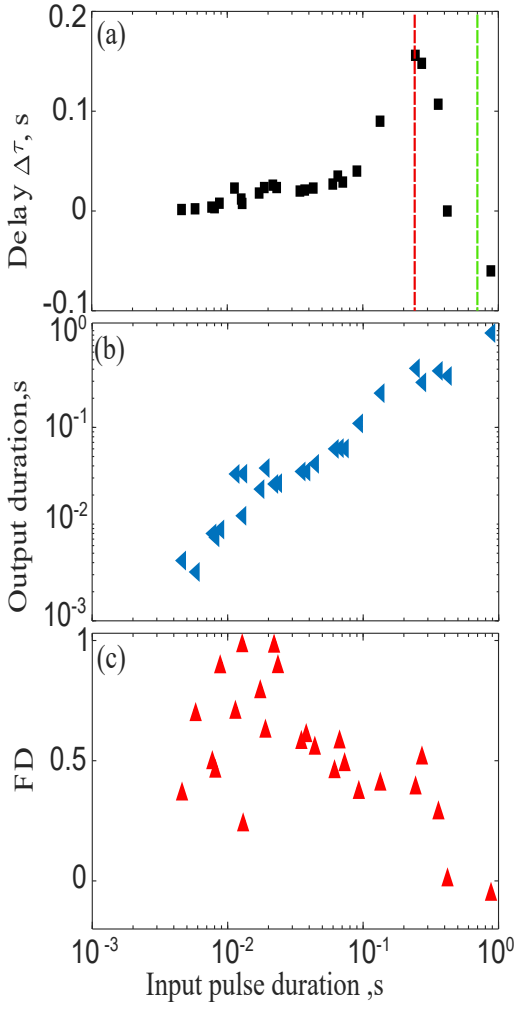

Figure 4.11: Performances of the slow dark pulse as a function of the input pulse duration t_0 at $\lambda = 638\ \ nm$, $\tau = 10\ ms$ and $\Gamma d = 5$. (a) Time delay. (b) Output pulse duration. (c) Fractional delay. The dotted red line in (a) presented the position of the maximum value of the delay. The dotted green line presents the position of negative delay values or advancement times [16].

Figure 4.11(b) shows that the output dark pulse width increases with respect to the input pulse durations. The transmitted dark pulse propagates through the PR SPS crystal with a small time distortion for $t_0 < 10\ ms$ or $t_0 > 40\ ms$. However, when the input pulse duration is close to the response time of the crystal ($10 < t_0 < 30\ ms$), the pulse widening becomes very important. For example, input pulses of $t_0 = 11$ and $t_0 = 19\ ms$ widen by twice their duration at the crystal's output. It means that the pulses that are significantly delayed ($\tau \geq t_0$) are the most broadened compared to the other pulses.

Figure 4.11(c) shows the value of fractional delay as a function of the input pulse durations. It is shown that the fractional delay is maximum for t_0 which is close to the crystal response time ($\tau = 10\ ms$). When $t_0 \gg \tau$ and increasing t_0, the delay value increases slowly than the increase of the dark pulse broadening, hence also decreasing the FD value.

Now, we compare the performances of slow light of dark pulses to those achieved with bright pulses. Figure 4.12 presents the behaviors of the delay and the fractional delay in both cases for ms pulses. From the curve of figure 4.12 (a), we note that for pulse durations close to the response time of the crystal, the dark pulses are more delayed than the Gaussian pulse. However, when the pulse width $t_0 \ll \tau$ or $t_0 \gg \tau$, the behaviors are almost the same in both cases. The same observation was noted for the fractional delay. As shown in figure 4.12 (b), Maximum values of 1 and 0.79 are measured for $t_0 \simeq \tau$ and $t_0 \simeq 100\ ms$ respectively for the dark and the Gaussian pulses.

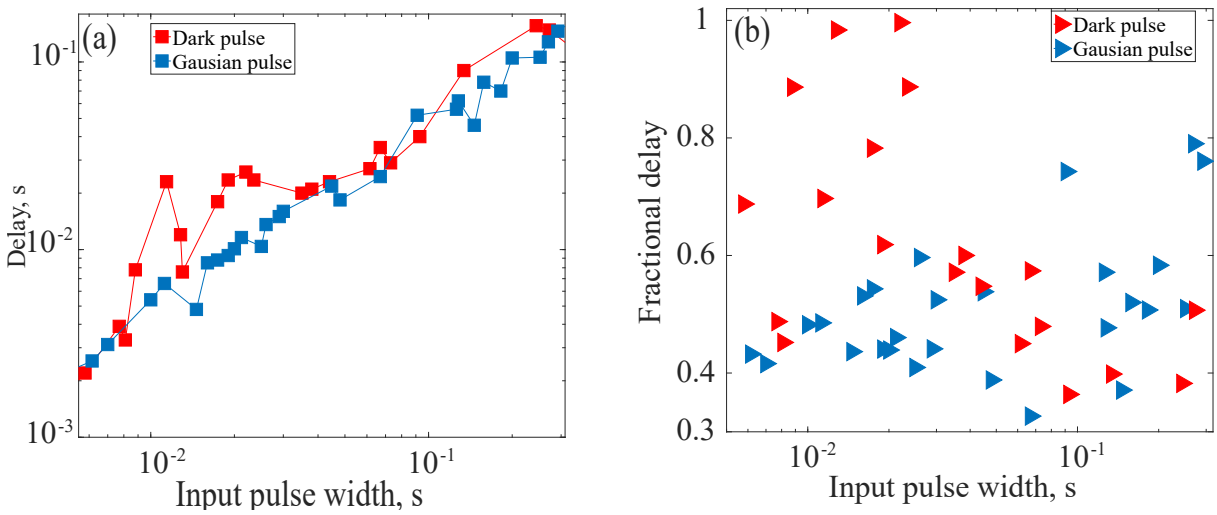

Figure 4.12: Delay (■ for a dark pulse and ■ for Gaussian pulse) and fractional delay (▲ for dark pulse and ▲ for Gaussian pulse) as a function of the input pulse duration t_0. For the Gaussian pulses for laser beam at $\lambda = 638\ \ nm$, $\tau = 10\ ms$ and $\Gamma d = 6.6$. For the dark pulses, $\tau = 10\ ms$ and $\Gamma d = 6.6$.

4.4 Conclusion

To conclude, we have theoretically and experimentally demonstrated that the two-wave mixing phenomenon in the SPS photorefractive crystal can be used to generate optical delays of dark pulses at room temperature. First, we have given a simple analytical expression that allows us to calculate the profile of the output intensity and to determine the optical delay undergone by the dark pulse during its propagation in this material. Numerical calculations based on this mathematical model are performed to analyze the performances of dark pulses deceleration, including the delay, the output pulse distortion and the resulting fractional delay.

In order to validate the analytical study, we have used the two-wave mixing setup to generate optical delays using dark pulses. Indeed, the experimental results confirm the validity of the theoretical model: in both cases, it is shown that the slow light performances depend on the PR gain and on the width of the input dark pulse.

Experimentally, we have measured a maximum delay of $\tau = 156\ ms$ for an input dark with duration $t_0 = 240\ ms$. This delay corresponds to a group velocity of $v_g = 3.2\ cm/s$ and a fractional delay of 0.4. However, the maximum fractional delays of 1 have been obtained

for shorter input pulse duration t_0 around the crystal PR response time $\tau = 10\ ms$. On the other hand, it is shown that for an input pulse duration in the range $0 < t_0 < 100\ ms$, the values of FD are more important than those of the Gaussian pulses.

Finally, the dark pulse with a duration close to the response time of the SPS crystal can be delayed by $\Delta\tau$ larger than t_0 when the Γ is important. In these conditions, the output pulse distortion becomes however important.

5

Slow light using the photorefractive beam fanning

Contents

The two-wave mixing process allows us to slow down light pulses in a photorefractive material with good performances, but this can be accompanied by some implementation difficulties. Indeed, the experimental scheme is very sensitive to external noise caused by mechanical vibrations. This may limit the photorefractive gain, hence reducing the slow light performances.

In this chapter, we demonstrate both theoretically and experimentally the slow light by making use of the so-called photorefractive beam fanning of the materials. This alternative method is more simple than a standard two wave-mixing configuration. Unlike the TWM, which is based on two incident waves coupling in the nonlinear material, this physical process is a nonlinear optical phenomenon involving only one single incident wave. We will first briefly review the state of the art of the beam fanning, its physics and its applications. In the second time, we will present the mathematical model that describes the light propagation in the photorefractive crystal in the presence of beam fanning. We will then report the results which demonstrate the slowdown of a single Gaussian pulse at both visible and infrared wavelengths. In both cases, we show that the fanning strength allows achieving both slowdown and acceleration of light pulses in the PR crystal.

The results of this chapter have been published in [14]

5.1 Beam fanning: state of the art and theoretical modeling

The propagation of light beam in photorefractive material is accompanied by different phenomena. Among these is the beam fanning which arises from the light amplification of the radiation, induced by the impurities in the PR crystal through a two-wave mixing between the input beam and its scattered light. In other words, when a laser beam passes through a photorefractive medium, it is often scattered on any crystal imperfections like defects, impurities and surface roughness. The incident beam interferes with the scattered light in the photorefractive crystal and because the beam fanning has a large number of spatial components, this coupling leads to the recording of several noisy index gratings in the PR crystal. As shown in figure 5.1, the beam fanning is superposed on the transmitted probe beam. Depending on the orientation of the PR crystal, it may be amplified or attenuated via the TWM. By placing a screen behind the crystal, we can observe the beam fanning as a broad fan-shaped beam which is formed by several wavelets propagating at different angles (different directions).

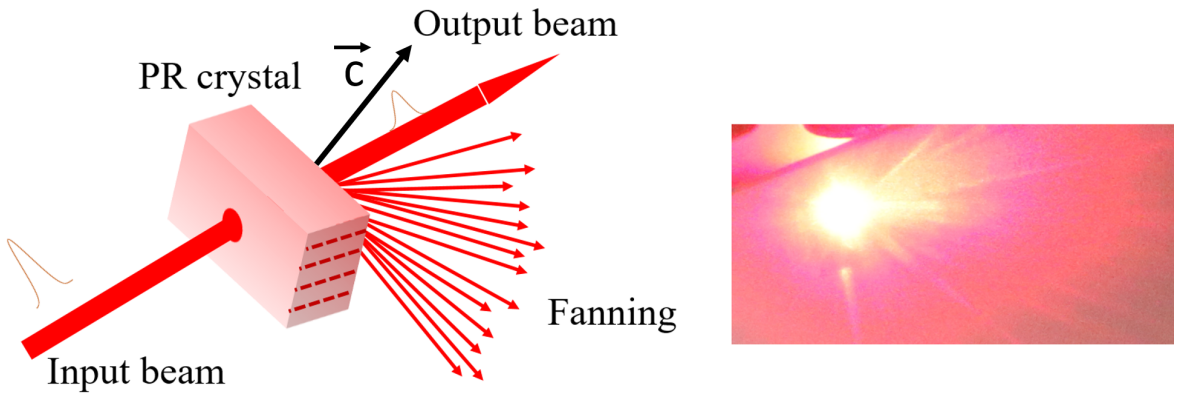

Figure 5.1: a) Geometry for optical beam fanning propagating in different directions. b) Photography of the beam fanning on a screen placed behind the PR crystal, obtained with a red laser at 638 nm in our PR $Sn_2P_2S_6$: Te crystal.

The strength of the beam fanning depends on three important parameters: - the incidence angle (angle between the incident beam and c-axis of the crystal)-the input beam intensity and-the polarization. It is characterized as the depletion variation of the input beam when it propagates through the PR crystal. This strength can be defined by the so-called depletion factor D which is the output beam intensity variation for different input intensity values [126]:

$$D = \frac{I_0 - I_{t\infty}}{I_0} = 1 - e^{-Gd} \tag{5.1}$$

where I_0 and $I_{t\infty}$ are respectively the initial intensity at $t = 0$ and the transmitted intensity at $t = \infty$ and Gd is the exponential depletion factor [127].

Figure 5.2 shows the attenuation of the transmitted beam intensity and the amplification of the beam fanning versus time at the output of the PR SPS:Te crystal.

5.1.1 Demonstration and modeling of the beam fanning

The term "beam fanning" was first used in 1982 by Feinberg [128] to describe the asymmetrical defocusing of light formed in a $BaTiO_3$ photorefractive crystal. In their device, an incidence laser beam at 514.5 nm with extraordinary polarization enters in the material and creates a "fan" of light that illuminates one of the crystal edges. The wave coupling between the input beam and the fanning can according to the author generate a high-quality replica of the conjugated phase of a beam that carries an input image. Figure

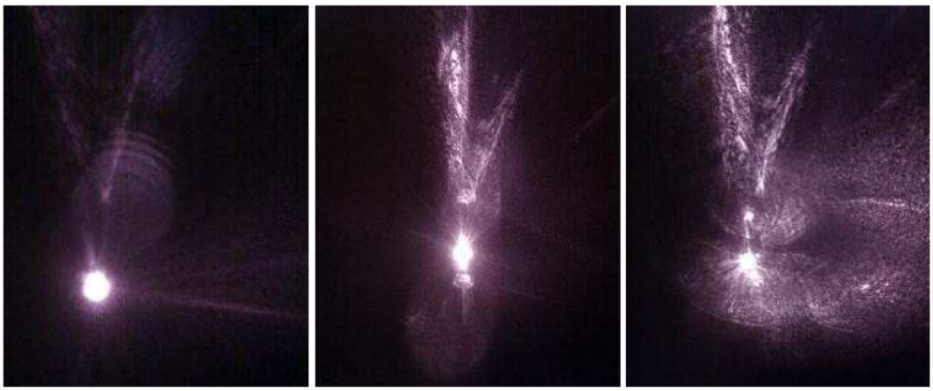

Figure 5.2: Beam fanning through a PR SPS: Te crystal. The three photographs follow each other in time and clearly show the implementation of this effect as well as the decrease in the intensity of the main beam [90]

5.3 shows that the presence of the loops characterizing the fanning in $BaTiO_3$ crystal depends on the polarization of the incident beam. When the incident beam is ordinarily polarized, no loop is observed (figure 5.3 (a)). On the other hand, the number of the loops increases when the input beam is extraordinary polarized and especially when the input beam carries an image (figure 5.3 (c)).

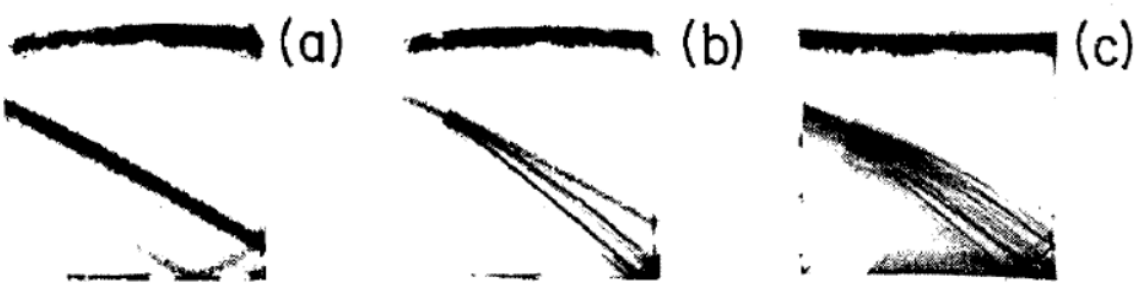

Figure 5.3: Photomicrographs of the photorefractive $BaTiO_3$ crystal, where, an incident beam inters on the left face of the crystal, the fan is the dark horizontal line that passes through the top of the crystal. a) Absence of the loop when the incident beam is ordinarily polarized. b) A loop appears between the input beam and the lower-right-hand edge of the crystal in the case of extraordinarily polarization. c) The number of the loop increases when the input beam bears an image [128].

This phenomenon had previously been observed in 1974 in pure $LiNbO_3$ crystal [129],

but known as photorefractive noises. In 1978, Voronov et al. [130] observed what they called in their turn "photo-induced diffusion" in a PR SBN crystal. They attributed this phenomenon to a holographic amplification of the light scattered over the defects of the PR crystal. In 1986 [131], the effect was also observed in Barium Titanate crystal and was attributed in this case to a stimulated photorefractive two-wave mixing process.

Since then, the beam fanning effect has attracted considerable attention and was studied widely [132, 133] both theoretically and experimentally. A theoretical model to calculate beam fanning using the beam coupling mechanism in a PR 45° cut $BaTiO_3$ crystal has been presented in 1993 [134]. In their configuration, a single incident beam was only considered to generate fanning and this last one has been characterized for different crystal orientations. An excellent agreement is obtained between the calculation results and the experiments performed by the authors. The calculation assumes the prior determination of the initial angular distribution of the scattered energy and, it requires the integration of the elementary intensity diffracted in one direction over the entire angular range.

In 1993 Segev et al. [135] studied the temporal and spatial evolution of the beam fanning in photorefractive materials. Their work involves the numerical resolution of the propagation equations for an incident wave decomposed into plane waves. This model systematically considers the horizontal deviation of the beam due to fanning (figure 5.4 (a)), and does not interpret the lobes observed with this effect. Other researchers have focused on the origin of these lobe structures (figure 5.4 (b)) in the fanning [136]. They demonstrated that these are explained by the piezoelectric and photoelastic contributions of crystal deformations to photorefractive non-linearity.

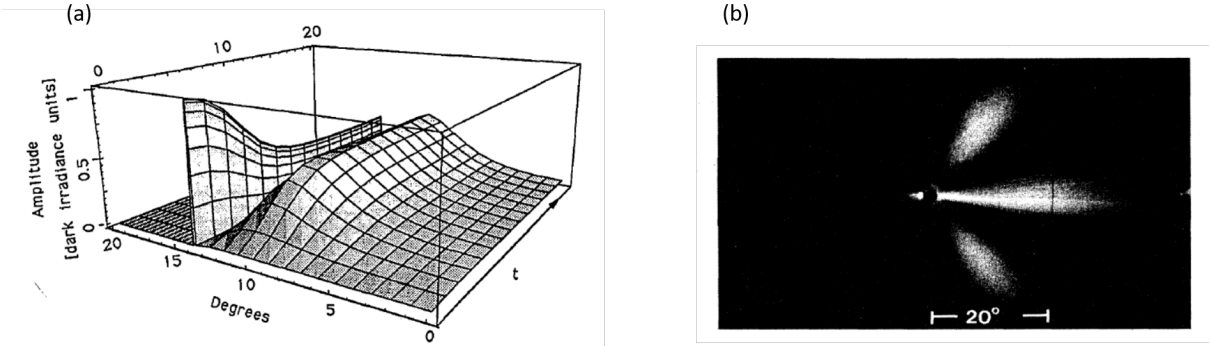

Figure 5.4: a) Temporal evolution of the beam fanning at the output of a $BaTiO_3$ crystal without absorption[135], b) Distribution of the beam fanning in $BaTi0_3$ at 514 *nm* wavelength observed by Montemezzani et al. [136]

In 1995, Zhang et al. [137] reported that the doping in a $LiNbO_3$ photorefractive crystal can control the strength of the beam fanning. They demonstrate that the beam fanning of $LiNbO_3$: Fe crystals could be suppressed by doping with damage-resistant dopant M(M=M^{2+}, In^{3+},Zn^{2+}). The evolution of the beam fanning in this crystal has been also investigated in 2001 [133]. They have shown that the intensity beam fanning is stronger with the illumination is starting and then is reduced through the time.

The photorefractive beam fanning and light scattering have been also observed in doped $Sn_2P_2S_6$. Here it is demonstrated that this effect depends on incident light polarization azimuth [138].

5.1.2 Applications

Beam fanning is an important nonlinear phenomenon in photorefractive materials that is used in several optical applications such as those involving the amplification of the signal beam. It has been used in the demonstrations of optical limiting [139], the Barium Titanate beam fanning novelty filter [140], self-pumped phase conjugation [141], incoherent-to-coherent conversion [142], and fast light manipulation. In the following, we briefly present three important applications of the beam fanning.

Optical limiters:

Since the publication of its first study in a photorefractive material, a number of device architectures using phase conjugate mirrors and the beam fanning was performed in the last years. Optical limiters involving beam fanning may reduce the input intensity of the beam propagating through the crystal and present several features: **1)** the use of a single input beam in the experiment makes the device design very simple and without thermal heating; **2)** it can operate at different wavelengths for which the photorefractive material can operate. **3)** It can also respond to sources with small coherence length. In 1985 [143], a preliminary study (figure 5.5) showed that the PR $BaTiO_3$ crystal can play the role of an optical limiter over the entire visible spectrum. This PR limiter dumps excess power from the incident beam into the beam fanning direction. In this case, it is reported that as much as $98 - 99\%$ of the incident light can be diverted to the fanning.

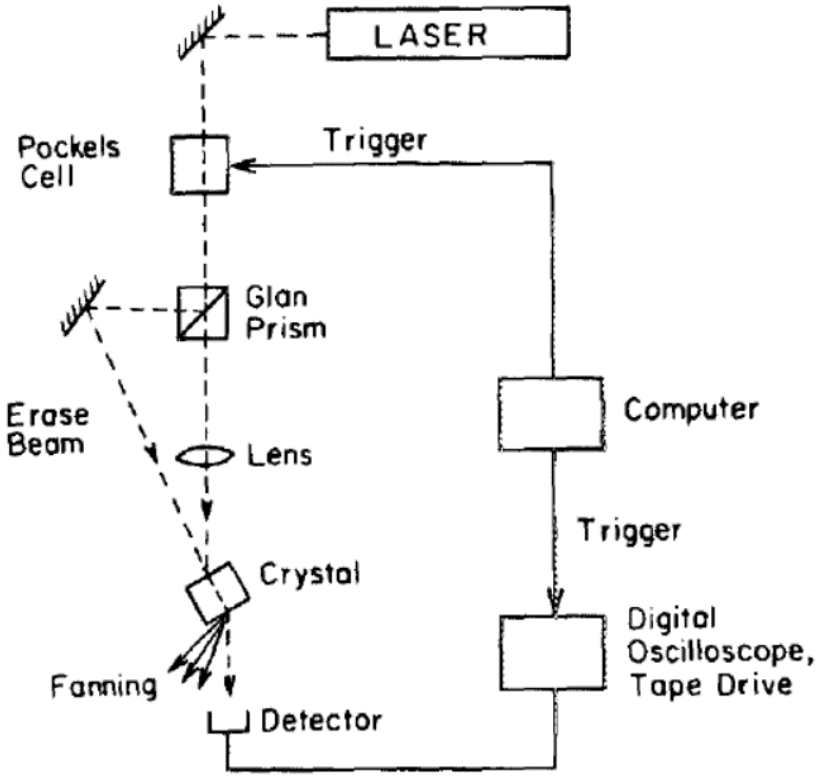

Figure 5.5: Experimental setup used to investigate fanning limiter performed with an argon-ion laser 488 nm, an electro-optic shutter and PR crystal ($5X5X4$ mm) with the c axis parallel to the 4-mm side [143].

Novelty filters:

Novelty filters can be used for phase visualization and measurement of the transient phase change in the laser beam. In addition to wave mixing, phase conjugate and another nonlinear process [144], the beam fanning effect is also employed to design a temporal PR novelty filter, which can detect only the modifications of the input beam (image). indeed, these systems detect only the image which changes within a response time of the PR crystal itself [144]. The scheme of the PR novelty filter using the fanning is presented in figure 5.6. Compared to the other optical filters, those designed with fanning are the simplest devices because they need to use only one single incident beam [145] in PR crystal with large TWM gain. It is reported that depending on the crystal orientation and the way to focus the input image in the crystal, this filter is sensitive to change in the amplitude, phase, or incident beam polarization [144].

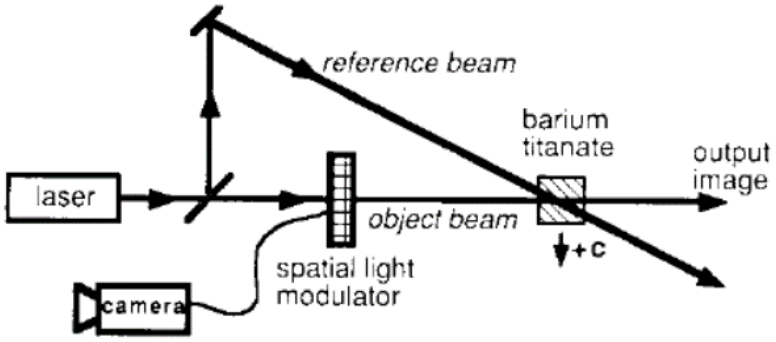

Figure 5.6: PR novelty filtering that uses two-wave mixing or beam fanning to deplete the energy of the input beam which bears an image. In the case of a beam-fanning novelty filter, the pumping beam is replaced by the fanning [144].

Fast light manipulation:

In 2004, A. Grabar et al. [127] have used the beam fanning to manipulate the light pulse propagation in PR material. They demonstrated that both Gaussian pulses and sinusoidal signals can be advanced in Sb-doped SPS crystal using the experiment presented in figure 5.7 (a).

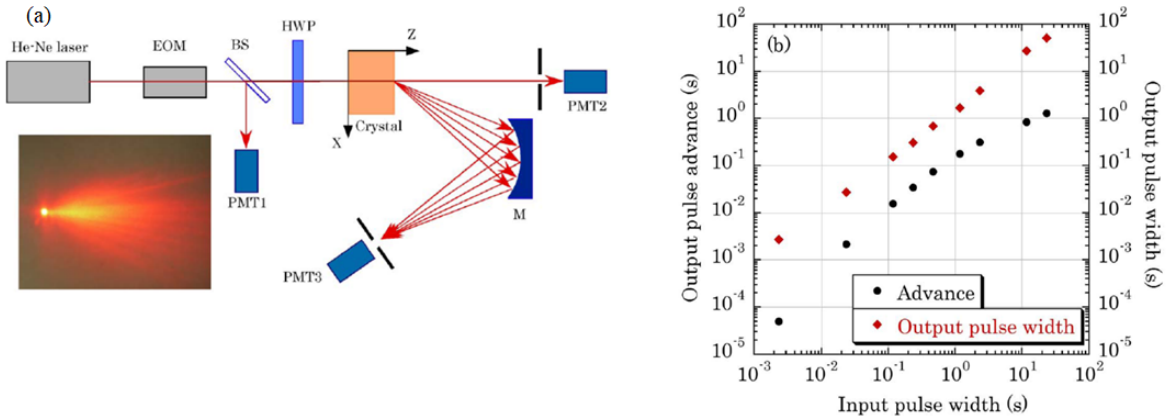

Figure 5.7: a) Experimental setup using the beam fanning. M is a mirror, HWP is a half-wave plate, EOM is an electro-optic modulator, BS is a beam splitter, PMT1, PMT2, and PMT3 are three photomultiplier tubes. b) Experimental measurement of the advancement time and the output pulse duration as a function of the input pulse width [127].

In their work, they characterized the exponential depletion factor Gd and the response

time of the crystal as a function of the input intensity. For the Gaussian pulses, the fast light scheme is achieved for a pulse width in the range 0.001-10 s. The measured advancement time and the output pulse width are presented in figure 5.7(b) for an exponential depletion factor Gd of the order of 0.4. In this case, they demonstrated that the fast light performances can be controlled by the intensity and the polarization azimuth of the input pulse.

In the following section, we propose another interesting application of the PR beam fanning which consists of the slowdown of one single light pulse in a SPS crystal using the same scheme as in [127].

5.1.3 Theoretical model of slow light using beam fanning

The coupling or the wave mixing of the input pulse with each wavelet of the fanning can lead to the amplification of the beam fanning and therefore to the modulation of the PR refractive index. This can lead to an increase in the dispersion in the material and to the slowdown of the transmitted pulse. Here we give a theoretical model that allows us calculating the output pulse intensity. Our mathematical model is performed with a single Gaussian pulse $I(0) = |A(0)|^2$ such as:

$$A(0) = A_0 exp(-t^2/T_0^2) \tag{5.2}$$

By analogy with the two-mixing between the input and the fanning beams, using equation 5.1, the Fourier transform of transmitted beam intensity, $I_\omega(d)$ in the frequency regime, propagating through a PR crystal with self-compensating response can be written as:

$$I_\omega(d) = I_\omega(0)e^{-Gdf} = I_\omega(0)(1-D)^f \tag{5.3}$$

where $I_\omega(0)$ is the Fourier transform of the input intensity $I(0)$, ω is the frequency and f is related to the response of the crystal and it is defined in equation 2.28. Using the inverse Fourier transform, the transmitted pulse intensity $I(d,t)$ becomes:

$$I(d,t) = \int_{-\infty}^{\infty} I_\omega(0)(1-D)^f e^{-i\omega t} d\omega \tag{5.4}$$

This equation may predict how the output pulse propagates in the photorefractive crystal in the presence of the beam fanning effect. As we can see, the value of $I(d,t)$ depends on

the time t, the depletion factor D, the input duration T_0 (T_0 is $1/e$ input width of the pulse intensity defined in section (3.1.1) and the input amplitude I_0.

Numerical simulations using equation (5.4) for three different values of the depletion factor D can give three major information: **1)** When the beam fanning is amplified, the incident pulse with full input pulse width at half maximum $t_0 = 20\ ms$ and $I_0 = 0.6\ W/cm^2$ (figure 5.8 (a_2)) is attenuated and delayed at the output of the crystal. As shown in figure 5.8 (a_2) and as discussed above, the variation of the output beam intensity depends on the values of D and vice versa. Whenever the fanning amplifies ($D \nearrow$), the intensity of the output pulse decreases. **2)** The value of the delay also changes with the strength of the fanning. From the figure 5.8 (a_2, b_1), the transmitted pulse is delayed by $\Delta\tau = 14$, 12 and 10 ms for $D = 0.94$, 0.93 and 0.91 respectively. **3)** If we change the sign of the depletion factor D, we note that instead of slowing down of the transmitted pulse, this one is speeding up. This situation is presented in figure 5.8 (b_2).

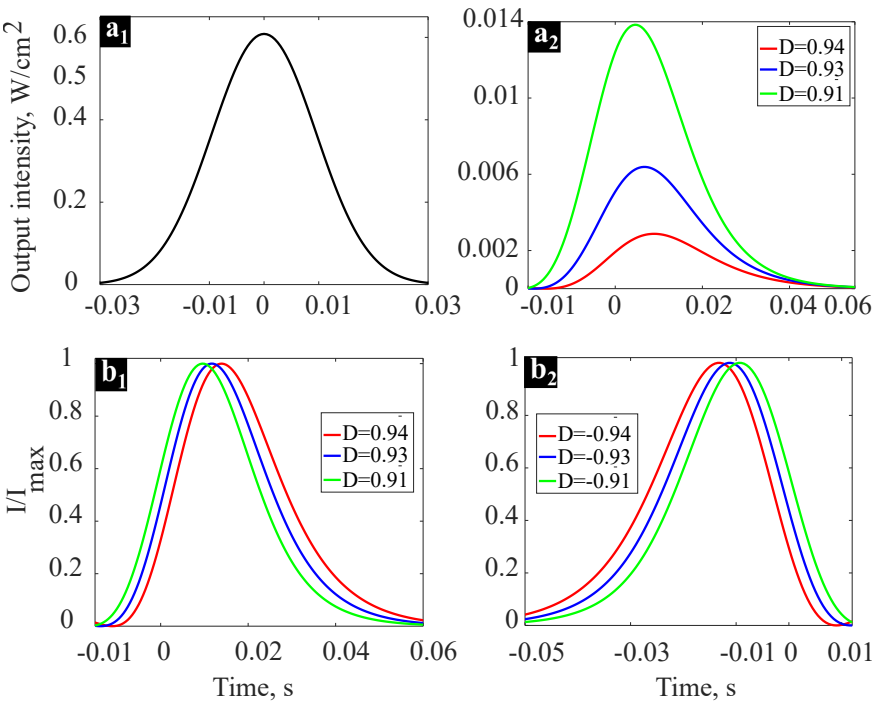

Figure 5.8: Theoretical results calculated with Equation.5.4 for different depletion factors D, time response $\tau = 10\ ms$ and $b = 0.9$. a_1) Input pulse with full input pulse duration at half maximum $t_0 = 0.02\ s$ and intensity $I_0 = 0.6\ W/cm^2$. a_2) Depletion of output pulse intensity I_d in the case of slow light configuration, for $D = 0.94$, 0.93 and 0.91, $I_d = 0.013$, 0.006 and 0.003 W/cm^2 respectively. b) Normalized output intensities for different values of D, in the case of slow light (b_1) and fast light (b_2) schemes.

More theoretical results showing the dependence of the delay and the depletion of the output intensity on the values of D are plotted in figure 5.9. The results are calculated for a 20 ms pulse in the PR crystal with charge self-compensation, where the fast response time τ is equal to 10 ms.

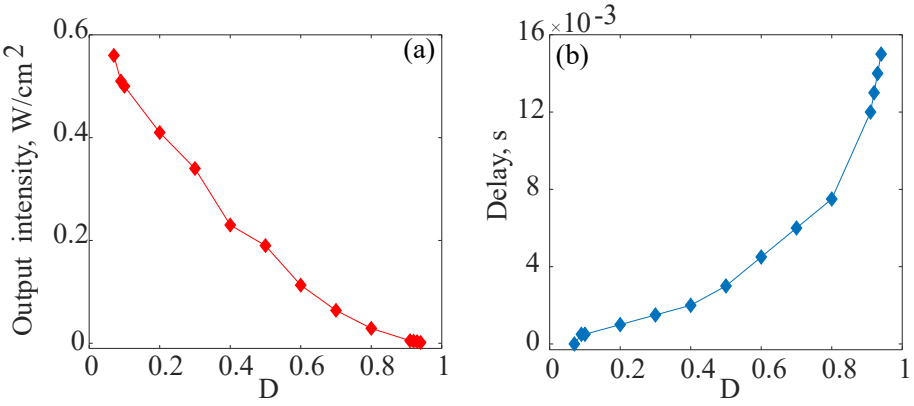

Figure 5.9: Theoretical results of the variation of the output pulse intensity (a) and the delay (b) versus the depletion factor D; time response $\tau = 10$ ms and FHWM $t_0 = 2$ř ms.

5.2 Experimental fanning characterization

In this chapter, we will show experimental results that demonstrate the slowdown of a single light pulse in a SPS crystal at room temperature. This configuration can be used to achieve slow light at both visible and infrared wavelengths. For both cases, we will start by measuring and characterizing the fanning as a function of the intensity and polarization of the input pulse. Then, in this section, the performances, the delay and the fractional delay are analyzed and discussed as a function of the width of the incident pulse in section 4.3.

5.2.1 Experimental Setup

The experimental setup used is shown in figure 5.10. It is much simpler than the one used in the two-wave mixing configuration and in particular, avoids a careful alignment between the pump and signal beams, in this configuration, the pump beam is replaced by the scattered light of the incident pulse. The same setup is employed to study the deceleration of light pulses at both visible and infrared wavelengths. For the visible (infrared) range,

a beam from a Crystal laser LC Model DL638 − 070−SO (Model IR−700 − 1064) with linear polarization is modulated by a NewFocus Model 4002-Visible Phase Modulator (NewFocus Model 4104-IR Amplitude Modulator). The input pulse of Gaussian shape is transmitted through a 0.5 *cm*-long Te-doped SPS crystal in the z-direction. The input and output pulse profiles are recorded by two amplified photodetectors D_1 and D_2: New Focus Model 1601, 1 GHz Low Noise PhotoreceiverNew (Focus Model 1611 IR, 1 GHz Low Noise PhotoreceiverNew). Finally, the results are analyzed by an oscilloscope.

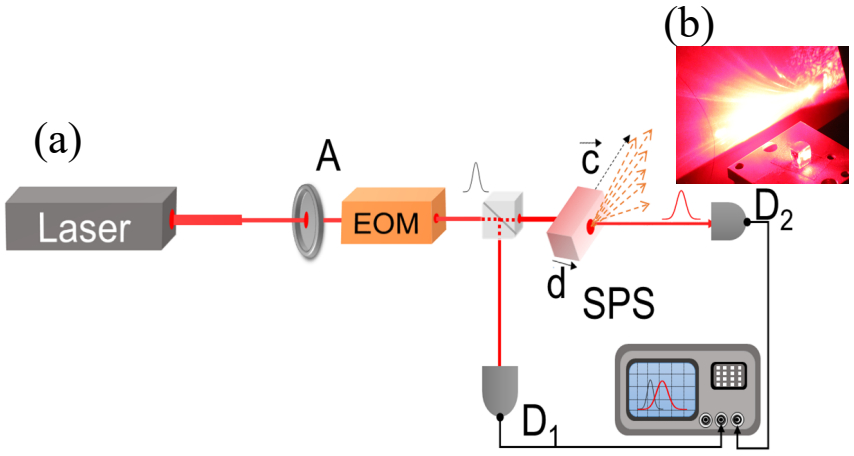

Figure 5.10: a) Experimental setup of slow light using beam fanning at two wavelengths 638 *nm* and 1064 *nm*; A: attenuator, EOM: electrooptic modulator, $D_{1,2}$: detectors and d: photorefractive SPS crystal thickness. b) Shape of the beam fanning at the output of the PR crystal.

5.2.2 Depletion factor at visible and infrared wavelengths

At the beginning of our study, we characterize the beam fanning of a Te-doped SPS photorefractive crystal versus different experimental conditions varying the intensity, the polarization, and the angle of incidence of the input beam. For this, we consider a Gaussian input pulse injected inside the crystal through the z-direction. When we rotate the crystal so that the incident beam and c-axis make an incidence angle $\theta = 45°$, a stronger beam fanning appears in the output pulse direction. On the other hand, if we change this incidence angle, the intensity of the transmitted pulse increases, while the fanning decreases at the output of the PR SPS. This observation means that the choice of the angle is crucial to maximize the fanning strength in the sample.

We vary the incident intensity using the optical attenuator and we measure both the input

and the output intensities on detectors D_1 and D_2 to determine the depletion factor D using equation 5.1. In figure 5.11, we plot the value of D at two wavelengths, $\lambda = 638$ nm and 1064 nm. As shown in both cases, the depletion factor increases with the input beam intensity I_0. If we compare the result of the two curves, we note that the values of D at $\lambda = 638$ nm are more important than those measured at $\lambda = 1064$ nm. For input intensity $I_0 = 0.6$ W/cm^2, a maximum $D = 0.94$ is achieved in the visible range, while the maximum value in the infrared domain corresponds to 0.54. So we can note that the coupling strength between the fanning and the incident beam is better in the visible range.

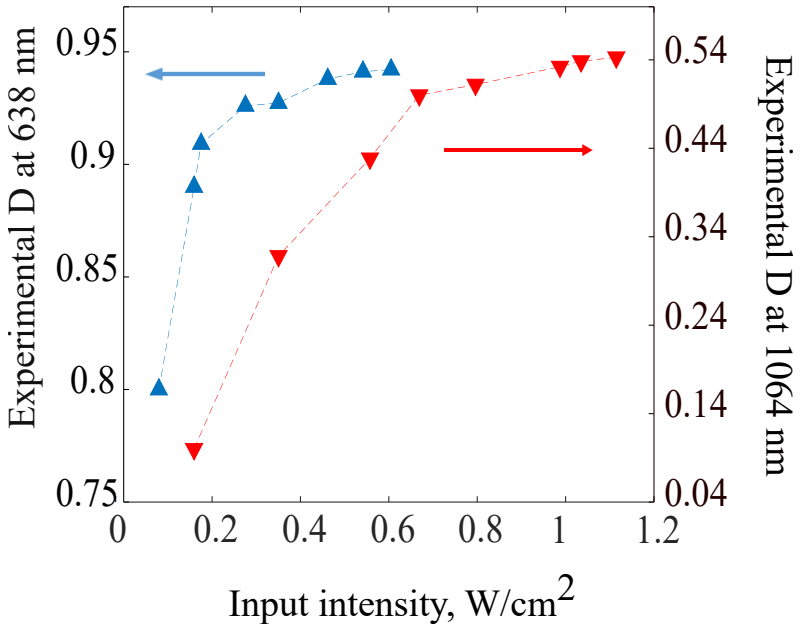

Figure 5.11: Experimental depletion factor D according to the input intensities. (▲) D at the visible wavelength in the SPS crystal with thickness $d = 0.5$ cm and response time $\tau = 10$ ms. (▼)D at the infrared wavelength in the SPS crystal with thickness $d = 0.5$ cm and response time $\tau = 13$ ms[14].

To show the dependence of the depletion factor versus the laser beam polarization, we illuminate the crystal with a red laser at 638 nm and adjust the experimental conditions so that we can generate a maximum fanning (input intensity $I_0 = 0.6$ W/cm^2 and $\theta = 45°$) at the output of the PR crystal. We use a mirror to collect the beam fanning and a lens to focus it into another detector to measure its power for different input pulse polarization. The experimental results are plotted in figure 5.12. As shown, the beam fanning power changes with the polarization and reaches a peak value of 1.3 mW at a polarization equal to 45°.

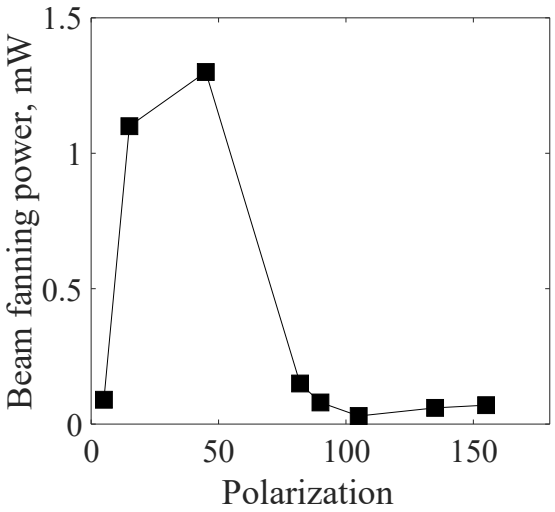

Figure 5.12: Experimental beam fanning power evolution at the visible wavelength versus polarization of the input pulse with an intensity $I_0 = 0.6\ W/cm^2$ and an incidence angle $\theta = 45°$ in the SPS crystal (thickness $d = 0.5\ cm$; response time $\tau = 10\ ms$).

5.3 Experimental slow light in the visible and infrared range

5.3.1 Evolution of the transmitted intensity pulse

In this section, we will present the experimental results that show the possibility of slowdown light pulses in the visible and infrared wavelengths using the photorefractive beam fanning at room temperature. In this aim, we fix the input beam intensity so that we get the maximum beam fanning at the crystal output with a depletion factor $D = 0.94$ at $\lambda = 638\ nm$ and $D = 0.54$ at $\lambda = 1064\ nm$. We measure the output pulse profile in both cases using the detectors $D_{1,2}$ and the oscilloscope.

Figure 5.13 shows an example of temporal profiles of input and output pulse intensities for different incident pulse widths. Figure 5.13(a_i) ($i = 1, 2, 3$) shows the result of the deceleration of light pulses in the PR SPS crystal in the visible range $\lambda = 638\ \ nm$ for an input pulse intensity $I_0 = 0.6\ \ W/cm^2$ and an incidence angle $\theta = 45°$. Figure 5.13(b_i) ($i = 1, 2, 3$) shows the result of slow-down of light pulses obtained with an IR beam laser at $\lambda = 1064\ \ nm$ of intensity $I_0 = 1.2\ \ W/cm^2$. In both cases, we note that the maximum of the transmitted pulse is delayed compared to the input pulse maximum. The deceleration

of the light pulse results from its coupling with the beam fanning when it propagates through the PR crystal.

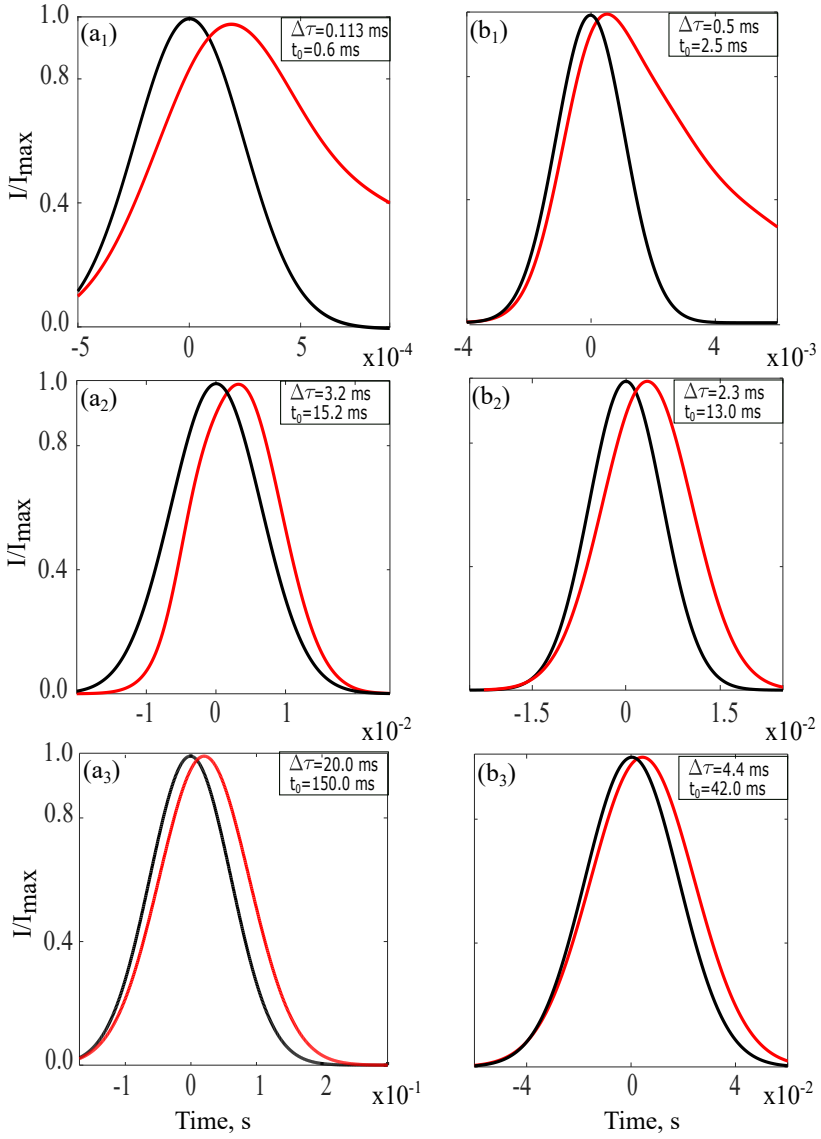

Figure 5.13: Experimental temporal envelopes of the normalized input pulse (black line) and output pulse (red line) as a function of the time for $\lambda = 638 \ \ nm$ and input pulse intensity $I_0 = 0.6 \ \ W/cm^2$ (a_i) and for $\lambda = 1064 \ \ nm$ with $I_0 = 1.2 \ \ W/cm^2$ (b_i) with $i = 1, 2, 3.$ (a_1) and (b_1) Input pulses durations $t_0 = 600 \ \mu s$ and $2.5 \ ms$ shorter than the response time of the crystal leading to deceleration; $\Delta\tau = 113 \ \mu s$ and $\Delta\tau = 500 \ \mu s$ respectively. (a_2) and (b_2) Input pulses durations $t_0 = 15.2 \ ms$ and $13 \ ms$ around the response time of the crystal leading to deceleration: $\Delta\tau = 3.2 \ ms$ and $\Delta\tau = 2.3 \ ms$ respectively. (a_3) and (b_3) Input pulses durations $t_0 = 150 \ ms$ and $42 \ ms$ greater than the response time of the crystal leading to deceleration: $\Delta\tau = 20 \ ms$ and $\Delta\tau = 4.4 \ ms$ respectively [14].

The results demonstrate that the beam fanning can slowdown light pulses shorter than the response time of the crystal, both at visible and infrared wavelengths. Two examples of these cases are shown in figures 5.13(a_1) and 5.13(b_1). Here, time delays $\Delta\tau = 113\ \mu s$ and $\Delta\tau = 500\ \mu s$ are measured respectively for pulses durations $t_0 = 600\ \mu s$ and $t_0 = 2.5\ ms$. In addition to the slowdown, the pulses broaden dramatically at the output of the PR media. When we increase the input pulse durations, the output pulse propagates in the crystal with less distortion: for both visible and infrared wavelengths, the measured delays time increases with the input pulse duration.

5.3.2 Comparison between slow light at visible and infrared wavelengths

Figures 5.14(a) and 5.14(d) plot the time delays $\Delta\tau$ for pulses respectively emitted by lasers at $\lambda = 638$ and $\lambda = 1064\ \ nm$ wavelengths. In both cases, the time delay value increases with the input pulse width. If we compare the curves of these figures, we note that the time delay values achieved at $\lambda = 638$ are larger than those measured $\lambda = 1064\ \ nm$ for the same input pulse duration. Indeed, for $\lambda = 638\ \ nm$, $\Delta\tau$ varies from 39 μs to 20 ms while for $\lambda = 1064\ nm$, it varies from 80 μs to 8 ms.

Figures 5.14(b) and 5.14(e) show the variation of the output pulse broadening factor R as a function of the input pulse duration for $\lambda = 638$ and $\lambda = 1064\ \ nm$ respectively. The factor R is the ratio of the full output over the full input pulse width at half maximum. It should be noted that in the ideal case when the pulse is transmitted without broadening and shape transformation, this factor is equal to 1. From figures 5.14(b) and 5.14(e), it is shown that the output pulse broadening is greater than 1 and it is found to be larger for pulse duration smaller than or equal to the time response of the PR crystal. For example, in Figure 5.14(e), we indeed distinguish two situations: i) for $0.08\tau < t_0 < 0.2\tau$, R varies from 1.5 to 2.1 which shows an important enlargement of the pulse that increases with t_0, ii) for $t_0 > 0.2\tau$, R decreases until reaching the ideal case for pulses greater than 20 ms.

Figures 5.14(c) and 5.14(f) then plots the fractional delay FD as a function of the input pulse duration. The fractional delay is defined by the ratio between the delay and the output pulse full width at half maximum. It varies between 0.05 and 0.4 for $\lambda = 638\ \ nm$ and the largest fractional delay value achieved at $\lambda = 1064\ \ nm$ is of the order of 0.2 for pulse duration $t_0 = 9.4\ ms$. The systematic analysis of figure (5.14) shows that the slow-light performances at $\lambda = 1064\ nm$ are slightly lower than those achieved at visible wavelength. This lower performance is due to the reduction of the coupling strength

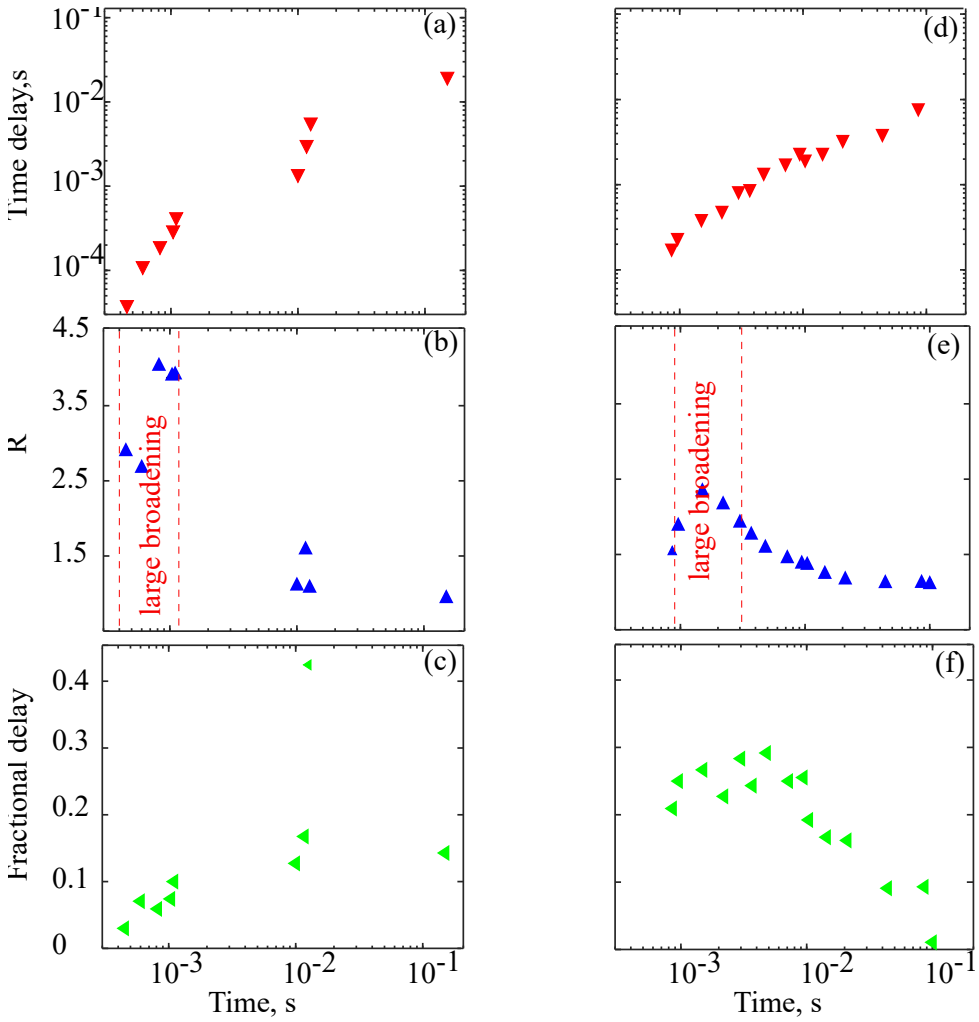

Figure 5.14: Performances of slow light as a function of the input pulse durations for laser beam at $\lambda = 638\ \ nm$, input pulse intensity $I_0 = 0.6\ \ W/cm^2$ and $\tau = 10\ ms$ (a,b,c) and for laser beam at $\lambda = 1064\ \ nm$ with $I_0 = 1.2\ \ W/cm^2$ and $\tau = 13\ ms$ (d,e,f). (a) and (d) Time delay. (b) and (e) Ratio between the output and input pulse durations. (c) and (f) Fractional delay [14].

between the input beam and the beam fanning, *i.e* for lower D value, when operating at infrared wavelengths.

5.4 Fast light using the beam fanning

The same experimental setup presented above may be used to generate both the deceleration and the acceleration of light pulses in a PR SPS crystal. This is possible because of the

self-compensating response of this type of crystal described in the first chapter. As we discussed, both phenomena can be experimentally observed by rotating the crystal by 180° which changes in the configuration of the transferred energy direction between the incident and the fanning beams (i.e the sign of D). Figure 5.15 shows the acceleration of a transmitted 500 μs pulse that is scattered at the output of the PR crystal when its c-axis is rotated by 180°. Both theoretical and experimental results are presented. The result of figure 5.15(a) is achieved using Equation. 5.4 for $D = -0.64$ and -0.91. We note that instead of the depletion of the input beam, it is amplified at the output of the crystal. As shown in figure 5.15(a) the delay value changes its sign and increases with the absolute value of D. figure 5.15(b) shows an experimental result of the acceleration of an input pulse with a duration of $t_0 = 200\ \mu s$.

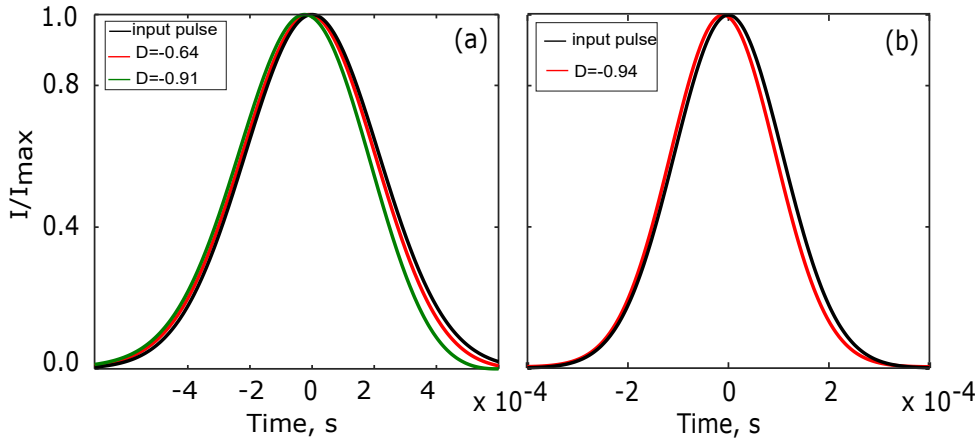

Figure 5.15: Temporal envelopes of the normalized input pulse and output pulse as a function of time. (a) Theoretical advancement of an input pulse of duration $t_0 = 500\ \mu s$ by using Equation.5.4, $\Delta\tau - 10\ \mu s$ and $-25\ \mu s$ are obtained respectively for $D = -0.64$ and -0.91. (b) Experimental pulse light advancement at 1064 nm when the SPS is rotated through 180°, $t_0 = 200\ \mu s$ with $\Delta\tau = -10\ \mu s$[14]

The performances of the fast light achieved at $\lambda = 1064\ nm$ for a depletion factor $D = -0.54$ are plotted in figure 5.16. As shown, the advancement is measured for short pulse durations of the order of μs. The advancement values vary from 0.5 μs to 3 μs for t_0 which vary between 15 μs to 30 μs.

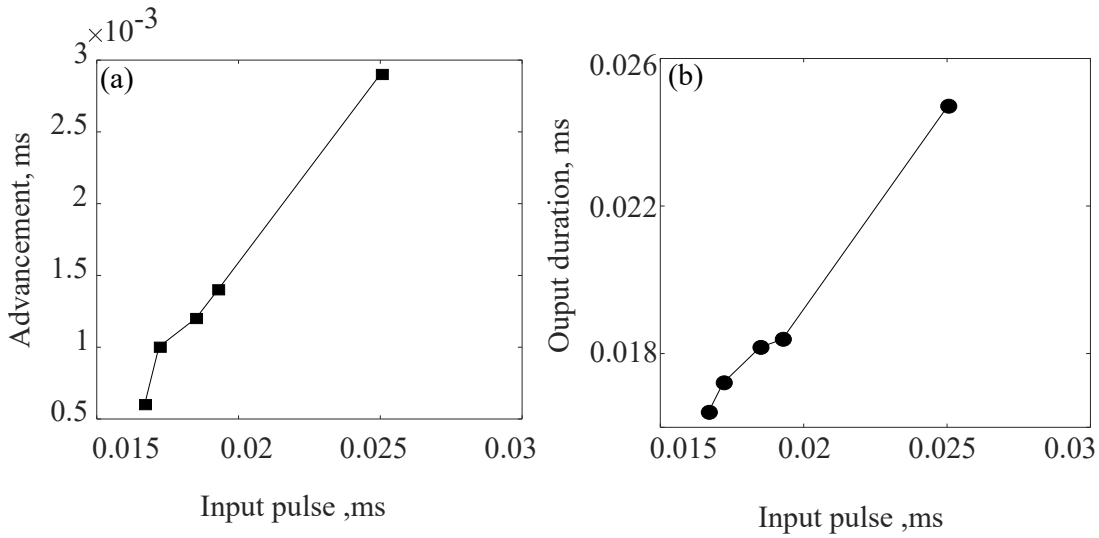

Figure 5.16: Performances of the fast light as a function of the input pulse durations for laser beam at $\lambda = 1064\ nm$, the input intensity $I_0 = 1.2\ W/cm^2$ when the SPS is rotated through 180° and $D = -0.54$. (a) and (b) plot the advancement time output pulse durations in the case of the fast light respectively.

5.5 Conclusion

In this chapter, we have reported a new mechanism to slow light, that involves the PR beam fanning at room temperature. First, we have shown that the beam fanning varies with the beam intensity, the incidence angle and the polarization of the input beam. We also have presented an analytical model that allows controlling the group velocity propagation of a Gaussian pulse with this effect.

Then the slow light performances have been experimentally studied and analyzed for both the visible and infrared ranges. The comparison of the results obtained for the two wavelengths shows that the slow light performances are better for visible than for infrared wavelengths. Indeed, the fractional delay is twice larger in the visible wavelength range compared to the one for infrared pulses. In addition, the analysis of the temporal broadening of the output pulse shows that the best fractional delay values are achieved for pulse durations close to the crystal time response.

We have demonstrated the slowdown of one single pulse of 13 ms with $v_g < 80\ cm/s$ and FD max equal to 0.4, which is very close to the state of the art performances we achieved earlier with a much more complex conventional wave mixing approach.

6

Nanosecond light pulses slowing down in a photorefractive crystal

Contents

In chapter 2 and 3, we have studied respectively the slowdown of bright and dark pulses using two-wave mixing of a modulated signal and a continuous pump. We have shown that this method allows achieving the first objective of my thesis: the improvement of the performances of the slow light of bright/dark pulses measured in a PR SPS crystal. However, the results are limited in terms of pulse duration. Indeed, we have seen that only long pulses (with durations of typically *ms-s* and at least larger than about 100 μs) can be slow down via this method both at the visible and infrared wavelengths. This limit is due to two main factors; (1) the crystal does not respond to light pulses shorter than its response time. (2) The narrow bandwidth of the signal generator we use does not allow us to generate pulse durations shorter than 100 μs.

In this chapter, we propose to use the so-called TWM in a photorefractive SPS crystal to slowdown nanosecond light pulses at room temperature. First, we will theoretically demonstrate that to slowdown nanosecond light pulses, it is important that: the response time of the optical nonlinearity and the duration of the laser pulses are comparable. Then, we will experimentally show that the use of a pulsed laser at an infrared wavelength with high intensity may reduce the crystal response time and increases the TWM gain. In that aim, the PR gain will be studied as a function of the grating period ($\lambda = 1$ μ to 5.5 μ), the input beam intensity and polarization. Finally, the performances of slow light at nano-regime will be discussed and analyzed.

6.1 How to slowdown short pulses in a PR material?

The photorefractive effect with nanosecond or picosecond pulses have been observed in different PR crystal [146, 147]. These optical pulses have two important characteristics: short durations and high peak powers. As the maximum electric field that can be induced in a PR material at the stationary state does not depend on the illumination, we cannot hope to increase the amplitude of the space charge field. On the other hand, the response time is inversely proportional to the input intensity I_0. So increasing this intensity may reduce the response time to a magnitude of the same order as the pulse duration applied at the input of PR crystal.

In this section, we will give the important conditions that allow us to slowdown shorter pulses (with durations of μs and ns) in a photorefractive crystal. Using equation 3.14 (section.3.1), we can expect that the performances of the deceleration of the light pulse

also depend on the response time of the crystal. The value of this response time can then fix the time range of pulse durations that can be slowed down in each photorefractive crystals.

Figure 6.1 shows the simulation results of the temporal envelopes of the input and output pulses. The calculations are done for two input pulse width: $T_0 = 1\ \mu s$ (figure 6.1 (a)-(e)) and $T_0 = 10\ ns$ (figure 6.1 (b)-(k)) for PR gain of 4 cm^{-1}, crystal thickness $d = 1\ cm$ and different values of the crystal response time ($\tau = 10^{-3}t_0$ to $\tau = 10^{3}t_0$).

The results show that the slowdown of shorter light pulses is possible if the value of the response time is close to the pulse duration that we want to slow down: 1) When, $10^2 < t_0/\tau < 10^3$ (figures 6.1 (a) and 6.1 (f), the output pulse propagates in the PR crystal with a small delay, $\Delta\tau = 0.01\ \mu s$ (figures 6.1 (a)) and $\Delta\tau = 0.5\ ns$ (figure 6.1 (f)). 2) For $t_0/\tau = 10$, the delay becomes more important $\Delta\tau = 0.3\ \mu s$ (figure 6.1 (b)) and $\Delta\tau = 4\ ns$ (figure 6.1(g)) and the light pulse propagates with small distortion. For $t_0 = \tau$, the output pulse is more delayed, $\Delta\tau = 2.4\ \mu s$ (figures 6.1 (c)) and $\Delta\tau = 25\ ns$ (figure 6.1 (h)) and its broadening becomes important. 3) For $t_0/\tau = 0.01$, the output pulse has not a Gaussian shape, but it consists of a sharp peak and a weak long-tail possessing a maximum shifted in the time (figures 6.1 (d) and 6.1 (j)). As the response time of the crystal increases, the output pulse returns to its Gaussian form, but is less slowed down than in the case where $t_0 = \tau$. Finally, if $t_0 \ll \tau$, no delay is calculated (figures 6.1 (e) and 6.1 (k)).

From this theoretical calculations, we can conclude that to slowdown very short light pulses in a photorefractive crystal, we have two possibilities: (1) first, we can use a sample with very short response time, of the order of the pulse duration, (2) We can use a laser with high intensity to reduce the response time of the nonlinear sample because we know that τ is inversely proportional to the input intensity.

6.2 Nanosecond two-wave mixing in SPS crystal

6.2.1 State of the art of TWM in a pulsed regime

In the CW regime, it has been reported that the photorefractive nonlinear materials can exhibit gain as great as 40 cm^{-1} in $BaTiO_3$ crystal [4] and 23 cm^{-1} [148] at the visible and

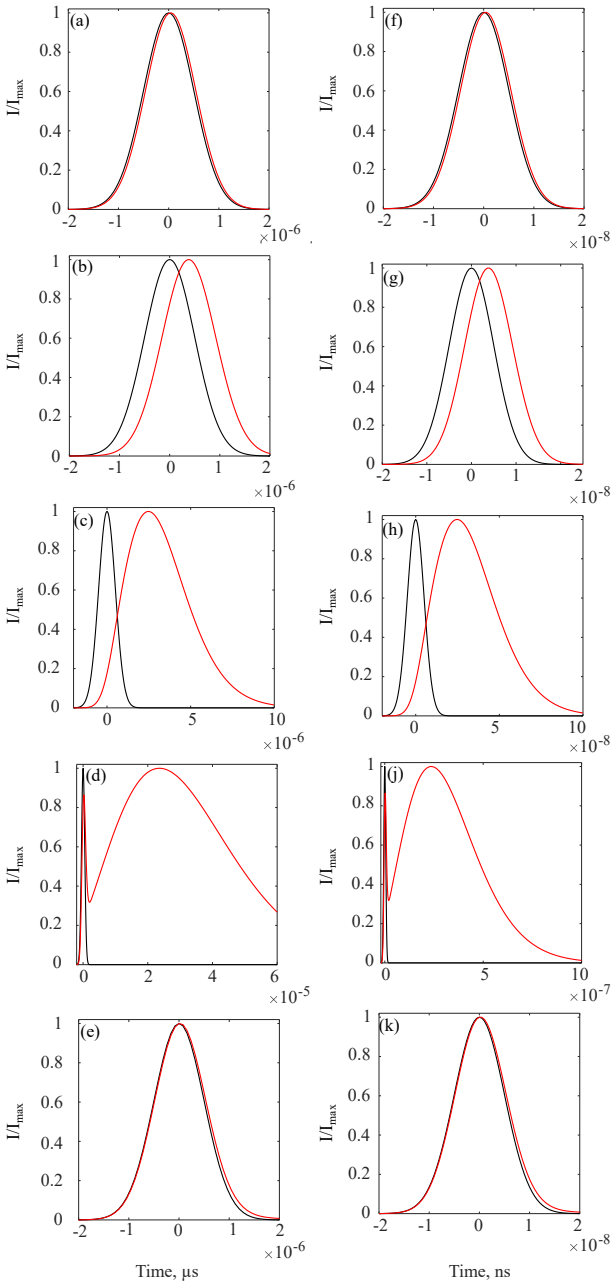

Figure 6.1: Results of slowdown of the $T_0 = 1\ \mu s$ and $T_0 = 10\ ns$ light pulses for frames (a)-(e) and (f)-(k) respectively, calculated using equation.3.14. For $T_0/\tau = 100$, $\Delta\tau = 0.01\ \mu s$ and $\Delta\tau = 0.5\ ns$ for (a) and (f) respectively. For $T_0/\tau = 10$, $\Delta\tau = 0.3\ \mu s$ and $\Delta\tau = 0.5\ ns$ for (b) and (g) respectively. For $T_0/\tau = 1$, $\Delta\tau = 2.4\ \mu s$ for (c) and (h) respectively. For $T_0/\tau = 0.01$, the output pulse has not a Gaussian shape for (d) and (j). For $T_0/\tau = 0.001$, $\Delta\tau = 0\ s$ for (e) and (f).

infrared ranges respectively. However, in this regime, the response time of the PR crystals are of the order of milliseconds to seconds. Hence, it is not obvious to use the PR effect

for very fast applications. The beam coupling at nanosecond or picosecond regimes has been however reported in different PR materials such as $BaTiO_3$[146], SBN and KNSBN [147].

The PR semi-conductors InP: Fe and CdTe: V crystals have also been used to study the beam coupling at the picosecond regime [149]. The pump and signal pulses are produced by mode-locked Nd: YAG laser at a wavelength of 1.06 μs. Figure 6.2 shows the photorefractive gain Γ, measured and calculated for CdTe: V, GaAs: EL2, and InP: Fe respectively. It is shown that the gain values vary from sample to sample. The largest values are measured in CdTe and the lowest in InP. Indeed, at a grating period of 1.7 μm and for fluences of 10 mJ/cm^2, gain values are 0.5 cm^{-1} for CdTe, 0.27 cm^{-1} for GaAs, and 0.13 cm^{-1} for InP. In 1991, Mark S. Petrovic et al, improved the gain value in the

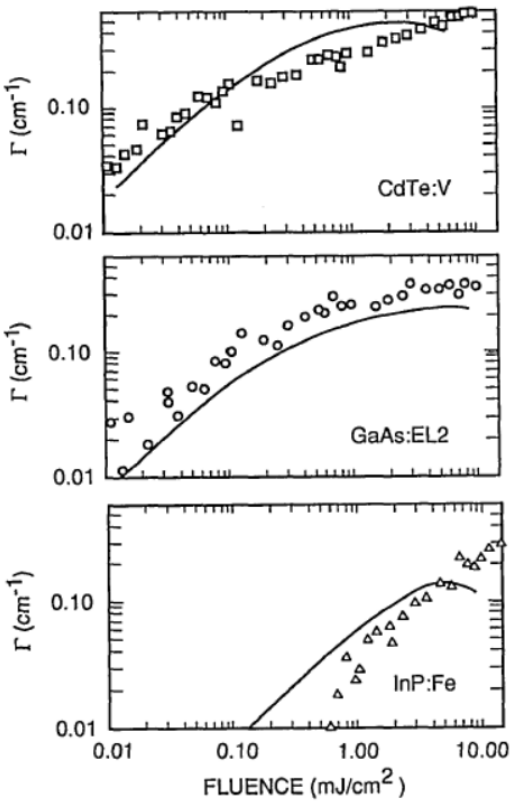

Figure 6.2: Photorefractive gain as a function of the fluence for three crystals. The solid curves are numerical calculations The squares, circles, and triangles indicate experimental results [149].

CdTe crystal to 2.3 cm^{-1} using the virtual-intermediate state, two-photon absorption (TPA) [150].

In 1987, Arthur L. Smirl et al. [146] have observed the photorefractive effect in 1.82-mm-thick $BaTiO_3$ crystal using pulses of 43 ps emitted by mode-locked Nd:YAG laser at 532 nm with fluences of 1 to 15 mJ/cm^2. A PR grating with a period of 0.48 μm is formed in less than 100 ps. After that, this crystal became one of the most interesting crystals at the pulsed regime. In 1996 [151], they demonstrated the photorefractive effect in $BaTiO_3$ crystal at 1.5 μm wavelength using two-photon absorption. They reported that when the crystal is illuminated by the high peak power of 250 mW, they can write refractive holograms in the sample for communication applications. Also, in 1997 [152], N. Huot et al. report a large photorefractive gain of 14.2 cm^{-1} in Rhodium-doped Barium Titanate ($BaTiO_3$:Rh) at 1.06 μm using TWM in the nanosecond regime. In their experience, they used the counterpropagating geometry shown in figure 6.3(a) which is performed by a Q-switched Nd: YAG laser that emits 10-ns light pulses with a repetition rate of 10 Hz.

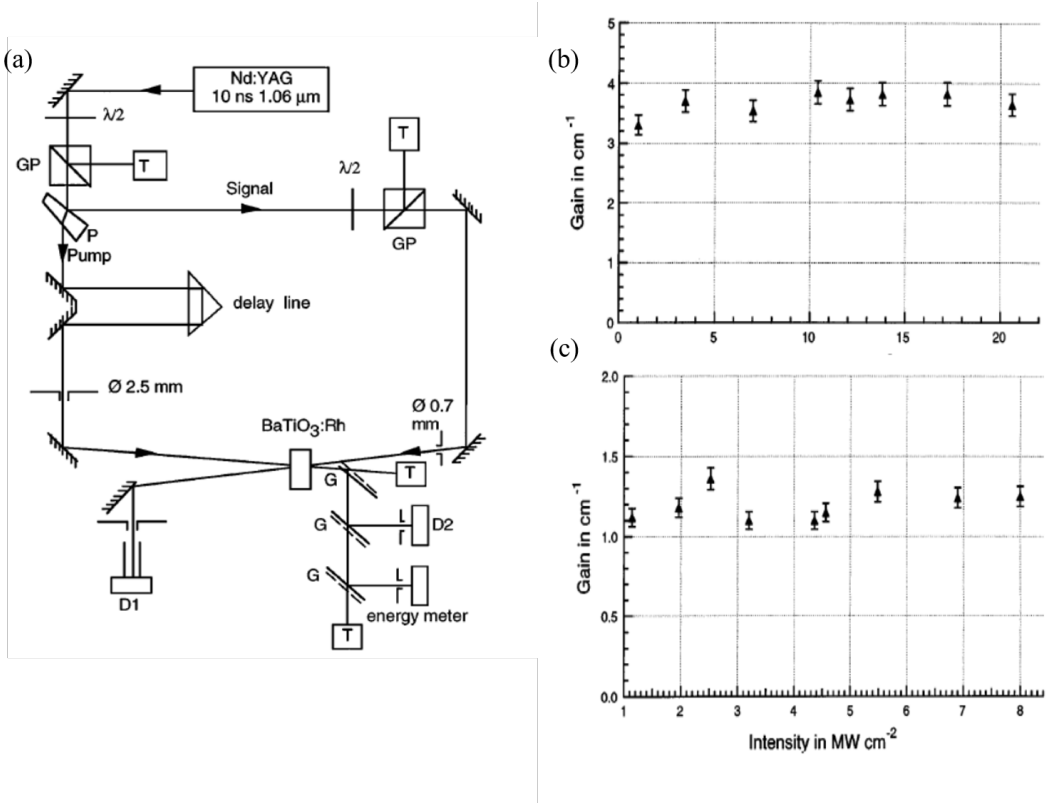

Figure 6.3: a) Experimental setup of the TWM in the counterpropagating geometry, GP are glan polarizers; G are the glass plates; T are light traps; $D_{1,2}$ are detectors and P is the prismatic glass plate. Exponential gain as a function of the intensity (a) with extraordinary polarized beams and (b) with ordinary polarized beams [152].

In 1996 [153], the PR SPS crystal was used in a holographic recording with 3-ns pulses at $\lambda = 1.64\ \mu m$. For this, they used a single-frequency $Nd3^{+}$: YAG laser with an energy of 35 mJ to write the holographic grating. While, a Helium-Neon laser at 632.8 nm of 20 mW has been used to read out the holographic. They have shown that the diffraction efficiency of holographic gratings increases with the input pulse energy (figure 6.4(a)). Also, it is reported that the diffraction efficiency depends on the orientation of the grating vector and its value decreases as a function of the polarization of the read-output laser beam (figure 6.4(b)).

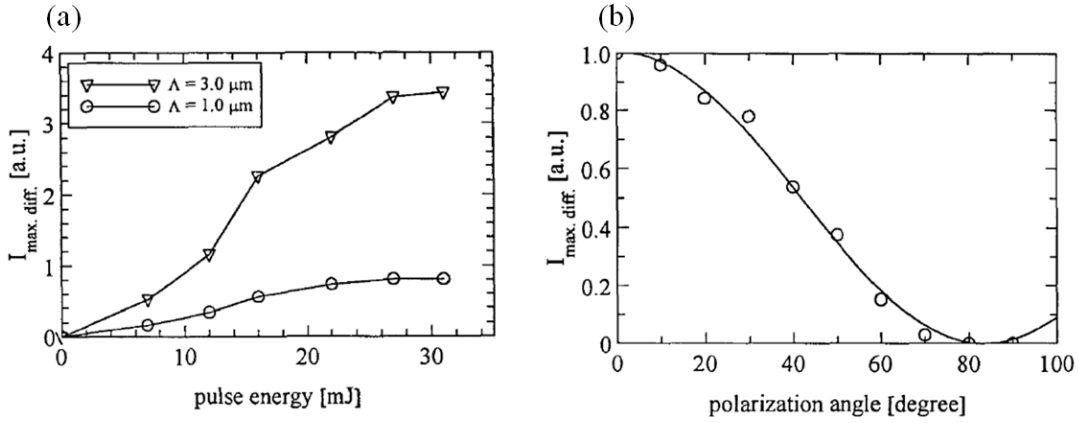

Figure 6.4: a) diffracted intensity as a function of pulse energy. b) diffracted intensity as a function of the polarization angle of the read-out beam [153].

6.2.2 Experimental setup

In this section, we will explain for the first time the practical realization of the two-wave mixing in a SPS crystal in the pulsed regime. We will evaluate the photorefractive gain as a function of polarization, input intensity, and grating period.

The scheme in figure 6.5 shows the experimental setup of TWM at the nano-regime. It is performed with Sb-doped SPS crystal with dimensions are 8.1×8×8.1 mm^3 along x-, y-, and z-axis and a laser from Quantel ULTRA BIG SKY LASER SERIES from at $\lambda = 1064\ nm$. The laser beam is split into two branches corresponding to the pump and signal pulses. The power distribution between the two beams is adjusted using a separator (BS). The power of the signal pulse can be controlled through the attenuator or the laser pulse duration. The two polarized light pulses enter inside the SPS sample with a certain

incidence angle θ. The intensity profiles of the input and output pulses are measured with two amplified photodetectors D_1 and D_2: New Focus Model 1611 IR 1 GHz Low Noise Photoreceiver.

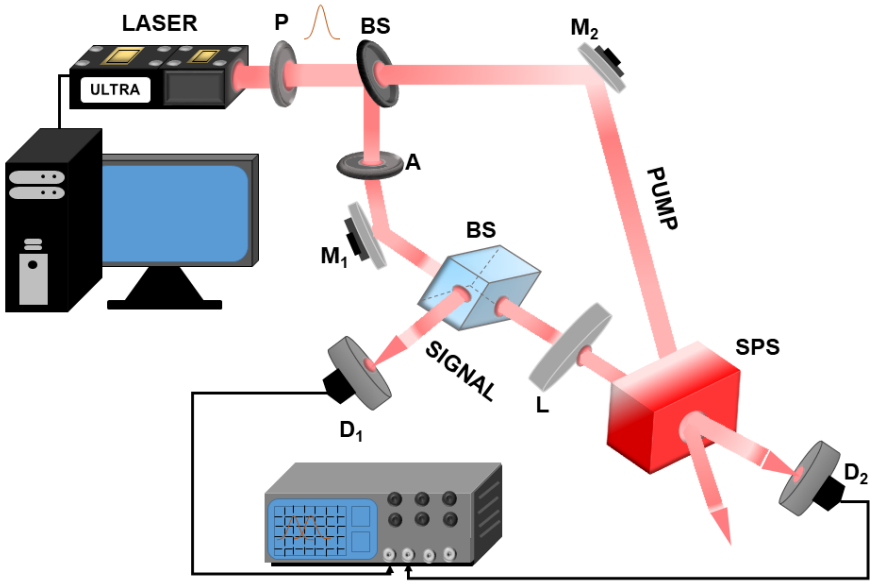

Figure 6.5: Experimental setup of slow light with two-wave mixing using a pulsed laser at 1064 nm; P is the polarizer, A is the attenuator, BS are the separator, $M_{1,2}$ are the mirrors, $D_{1,2}$ are the detectors and L is the lens.

The Quantel ULTRA BIG SKY LASER used in the experiment (figure 6.6) is a flashlamp-pumped Nd: YAG laser that can generate ns pulses from 7 ns to 100 ns with a pulse repetition rate of 20 Hz and a near field beam diameter of 2.6 mm. It can operate at two wavelengths: 1064 and 532 nm with a maximum energy of 17 and 30.9 mJ respectively.

A free terminal emulator program called "PuTTy" can be used for serial communication with the laser. From this platform, we can control the percentage of laser transmission, therefore the power and intensity emitted by the laser. Figures 6.7 (a,b) show the power and the intensity of the laser for a pulse with 7 ns duration. By changing the percentage of laser transmission from 10% to 100%, the laser power can vary from 55 to 300 mW.

The first beam splitter in the experiment splits the laser beam into two beams and adjusts the power between them ($P_signal = 0.1P_pump$). Figure 6.8, presents the power of the

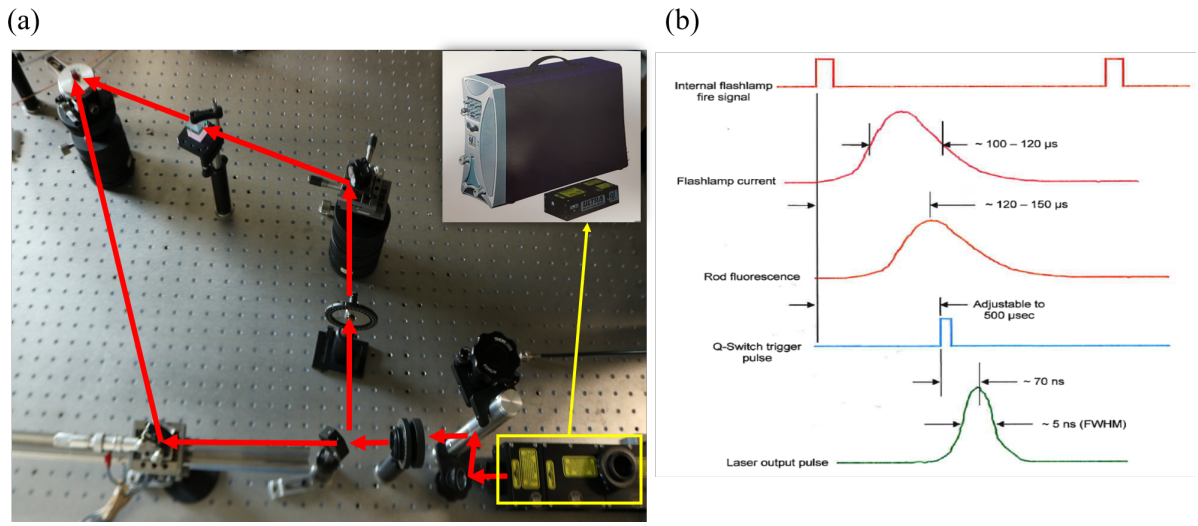

Figure 6.6: Photography of the experimental setup and the characteristics of the Ultra laser.

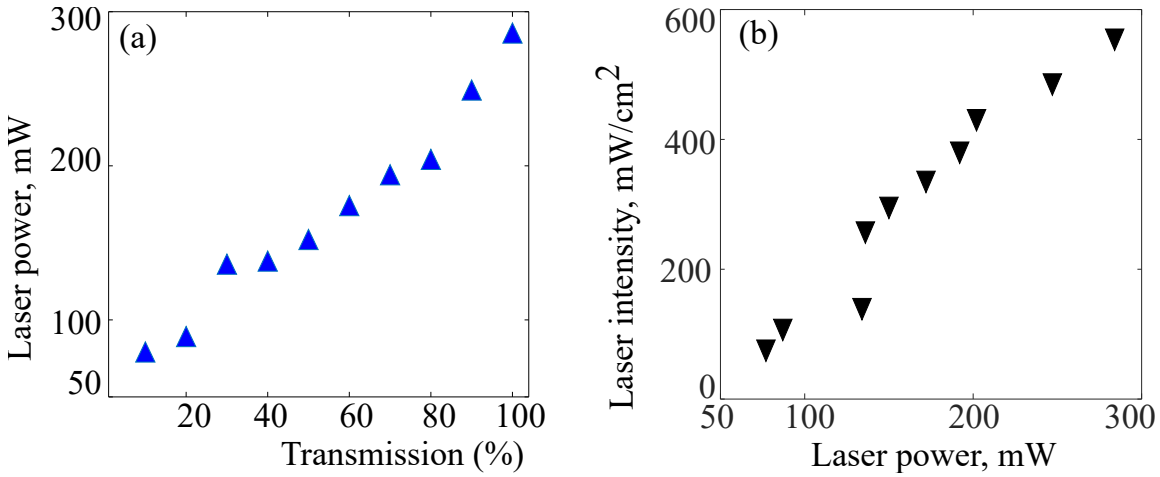

Figure 6.7: Laser characteristics for a pulse duration of 7 ns and a repetition rate of 20 Hz. a) Control of the laser power as a function of the transmission rate. b) Laser intensity as a function of the power

signal pulse as a function of its duration for a laser power $P_L = 0.05\ W$. As shown, for a fixed transmission rate, the power values of the signal decrease with the pulse duration which is controlled by the computer.

When we analyze the intensity profiles measured by the two photodetectors in this configuration, we observe that the output pulse is amplified. To determine if this amplification results from the two-wave mixing of the pump and the signal, we make a series of measurements of the photorefractive gain under different conditions. Note the value of the photorefractive gain depends both on the type of material, eventually its doping, the

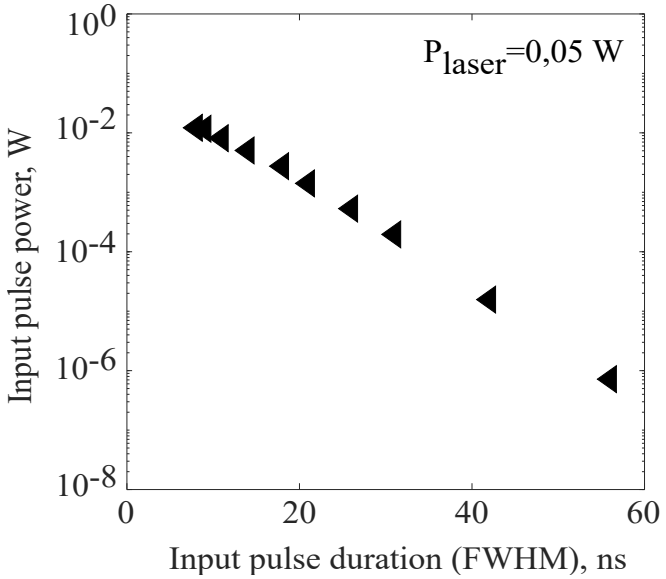

Figure 6.8: Input pulse power as a function of the input pulse duration for a laser power equal to 0.05 W.

optical wavelength and the photorefractive configuration. By configuration, we mean the incidence angle that is related to the grating period, the polarization of the input beams, the sample cross-section (the entrance faces, the direction of light propagation), and the application or not of an external electric field.

In the following, we will measure the power of the signal at the input P_{sin} and output P_{sout} of our SPS sample with thickness d (in the presence of the pump pulse) and calculate the amplification factor γ related to the photorefractive gain Γ in the case of the undepleted pump approximation.

6.2.3 Photorefractive gain as a function of the polarization

In this subsection, we measure the photorefractive gain versus the ratio between the pump and signal pulse powers for horizontal, vertical and azimuthal polarization. The resulting PR gains measured with a pulsed laser power $P_L = 150\ mW$ are compared to those achieved with a CW laser.

Figure 6.9 shows the evolution of the PR gain as a function of the ratio between the pump and the signal powers for different polarization. Figures 6.9 (a_1) and 6.9 (a_2) present the results of gain values measured with the two-wave mixing in the pulsed and continuous (CW) regimes respectively. By analyzing the resulting curves carefully, we can note that

in all cases (when the two beams have the same polarization), the gain increases with the ratio of input intensities. However, the photorefractive gain reaches optimal (higher) values when the pump and signal beams are horizontally polarized (or parallel to the crystal axis of the spontaneous polarization), which corresponds to the optimal configuration of the two-wave mixing mentioned in the literature. In all cases, the values of the gain achieved with the TWM at the nanosecond regime are more important than those of TWM with a continuous pump.

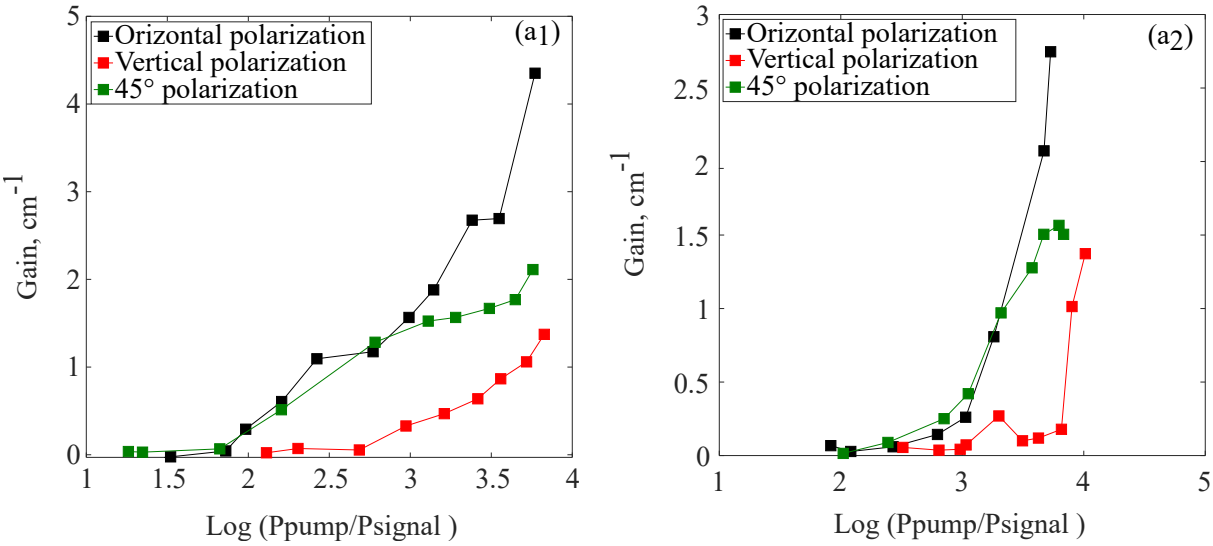

Figure 6.9: Photorefractive gain in SPS doped Sb as a function of the ratio between the pump and signal beams for Horizontal (parallel to the spontaneous polarization of the crystal), vertical and 45° azimuthal polarization. The incident angle between the two pulses is $\theta = 45°$. (a_1) and (a_2) results achieved with a pulsed laser and a CW laser respectively at $\lambda = 1064\ nm$.

6.2.4 Photorefractive gain as a function of the grating period

To check that nonlinear phenomenon, concerns the PR effect, we measure in figure 6.10 the dependence of the PR gain Γ on the grating spacing Λ measured with CW and pulsed laser. The curves show that the gain increases with the grating period until it reaches a maximum value at $\Lambda = 1.5\ \mu m$ then it decreases for $\Lambda > 1.5\ \mu m$. Also, the results show that the TWM at nanosecond regime leads to an increase in the maximum gain Γ up to 4.4 cm^{-1} as compared to 3.2 cm^{-1} with the TWM in the case of the continuous pump. On the other hand, we note that the curved behavior obtained in the pulsed regime is

similar to that achieved in the continuous regime, which means that the effect observed in our sample is a photorefractive one.

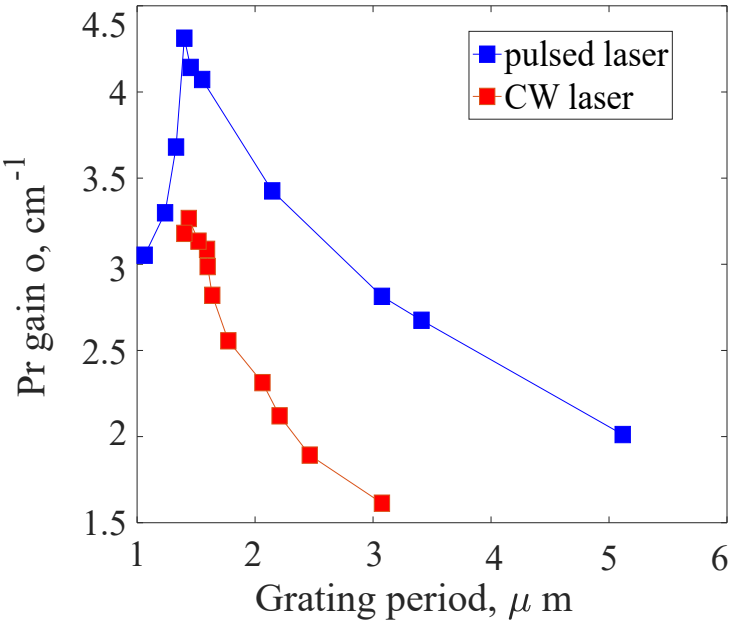

Figure 6.10: Photorefractive gain of the Sb-doped SPS crystal versus the grating period Λ for continuous (CW) and pulsed laser at $\Lambda = 1064$ nm with power 150 mW and 200 mW respectively. The input beam are polarized horizontally

6.3 Slowing down nanosecond light pulses in SPS doped Sb

From our theoretical study, we have shown that it seems very difficult to achieve the deceleration of shorter pulses but not impossible if we can reduce the crystal response time to the order of the applied pulse duration. Here, we will experimentally demonstrate for the first time the possibility to slowdown nanosecond light pulses in a photorefractive crystal at room temperature. Note that even if the TWM in two crystals (SPS doped Te and Sb) allows to have a large photorefractive gain, it turns out that only the Sb-doped SPS can slow down the light. The reasons for that remain unclear at this stage. Here the signal and the pump pulses interfere in the PR crystal x-face and propagate through the $y-$axis. As in the case of the CW laser, we study the slow light performances as a function of the photorefractive gain and the input pulse duration.

6.3.1 Output intensity evolution

We use an oscilloscope (4 GHz. 20 GSa/s) to analyze the pulse at the input and output of the SPS crystal when the pump pulse is switched off and on (without and with TMW). An example of an experimental result is shown in figure 6.11. If we turn off the pump pulse, we note that the output pulse propagates through the crystal without any delay (figure 6.11(a)). While, in the presence of TWM in the SPS crystal, the output pulse amplifies and its maximum is shifted by comparison to the input one (figure 6.11(b)).

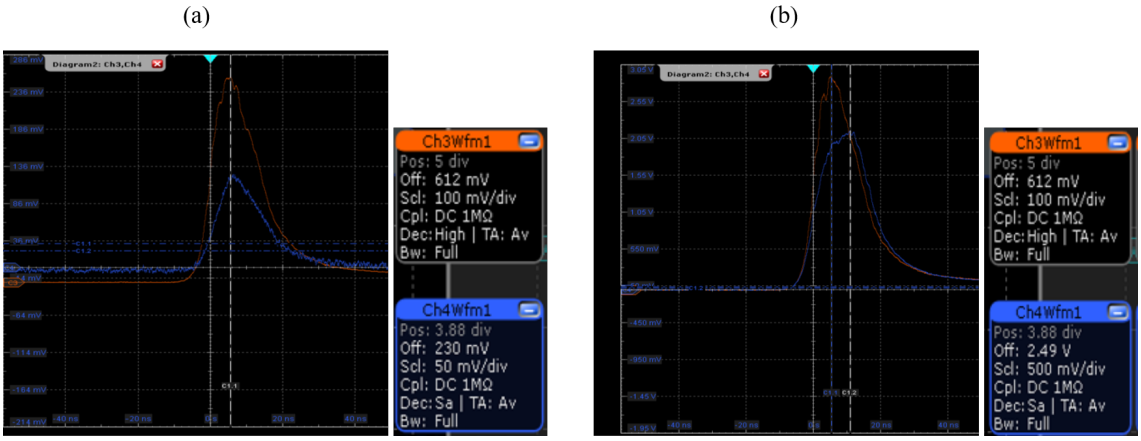

Figure 6.11: Experimental result measured using an oscilloscope (4 GHz. 20 GSa/s) of slowdown $10 - ns$ pulse in the SPS crystal. Evolution of the input (orange line) and output (blue line) intensities without (a) with the pump pulse (b).

Figure 6.12 shows the temporal envelopes of input (black line) and output (red line) pulses for six input pulse duration $t_0 = 8,\ 14,\ 28,\ 34,\ 42,\ 70\ ns$ for frames (a), (b), (c), (d), (e) and (f), respectively. We note that for $t_0 = 8\ ns$, no delay is observed but when increasing the input pulse duration, the maximum of the output pulse is shifted by comparison to the input pulse maximum. As in the case of ms pulses, the time shift between the maximum of the output and the input pulses defines the value of the time delay. More specifically, for pulse widths $t_0 = 14\ ns$, $28\ ns$, $34\ ns$, $42\ ns$ and $70\ ns$, we measure delays $\Delta\tau = 1.6\ ns$, $4\ ns$, $7.2\ ns$, $10\ ns$ and $17.4\ ns$ respectively. Note that as since the values of the delay are quite small, to translate these values into group velocity values, it is important to introduce the material contribution to the time delay $\Delta\tau$ as:

$$\Delta\tau = \frac{L}{v_g} - \frac{Ln}{c} \tag{6.1}$$

From this equation, we can write the group velocity as follows:

$$v_g = \frac{dc}{\Delta\tau c + nd} \tag{6.2}$$

where $L = d$ is propagation length (the thickness of the crystal), c is the celerity in the vacuum and n is the refractive index of the crystal. For time delay of the order of ms or s, we note that $\Delta\tau c >> nL$, so $\Delta\tau$ is equal to the group delay t_g and $v_g = L/\Delta\tau$ (section.3.2.3). In our case, as $\Delta\tau c \sim nL$, we use equation.6.2 to determine the velocity values. The corresponding group velocities to the time delays $\Delta\tau = 1.6\ ns$, $4\ ns$, $7.2\ ns$, $10\ ns$ and $17.4\ ns$ are respectively $v_g = 6000\ km/s$, $2500\ km/s$, $1400\ km/s$, $1000\ km/s$ and $500\ km/s$.

On the other hand, the results show also that the output pulse is broadened in all cases. However, the measured output pulse broadening is less than that observed in the case of millisecond light pulses deceleration in the visible range using a CW laser. This means that two-wave mixing with a pulsed laser allows decelerating shorter pulses and limits the distortion factor of the output pulse.

6.3.2 Slow light performances at nanosecond regime

In this subsection, we will analyze the slow light performances at the nanosecond regime as a function of the PR gain and the output pulse durations. Figure 6.13 shows the output pulse shape for pulse duration $t_0 = 32\ ns$ and three values of the photorefractive gain. These gain values $\Gamma = 5.9,\ 7.4,\ 7.9\ cm^{-1}$ are measured respectively, for the signal pulse power of $1,\ 0.4,\ 0.2\ mW$. As shown in Figure 6.13, the delay values vary with the photorefractive gain. Delay $\Delta\tau = 9.2,\ 10.4,\ 12.4\ ns$ are measured respectively, for $\Gamma = 5.9,\ 7.4,\ 7.9\ cm^{-1}$.

In addition to the slowdown of the transmitted pulse, we have observed in all cases that it broadens the pulse at the output of the PR crystal. This widening is due to the large photorefractive gain values (dispersion in the crystal). For $\Gamma = 7.9\ cm^{-1}$, the output pulse is delayed without much broadening in comparison with the other two cases (Figs. 6.13(a) and 6.13(b).

Figure 6.14, shows the curves of delay and fractional delay as a function of the photorefractive gain. The results are achieved for an input pulse duration of $t_0 = 32\ ns$. As

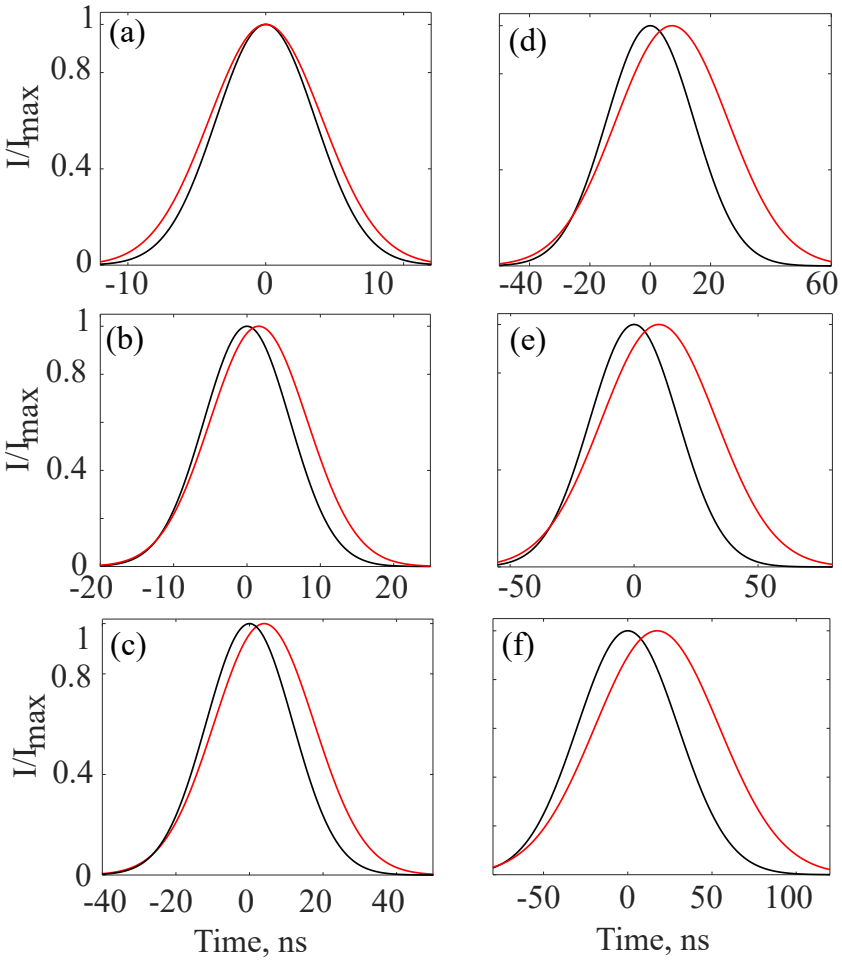

Figure 6.12: Temporal envelopes of the normalized input (black line) and output (red line) pulses as function of the time for $P_{laser} = 150$ mW. (a) Time delay $\Delta\tau = 0$ ns for $t_0 = 8$ ns, (b) $\Delta\tau = 1.6$ ns, for $t_0 = 14$ ns, (c) $\Delta\tau = 4$ ns, for $t_0 = 28$ ns, (d) $\Delta\tau = 7.2$ ns, for $t_0 = 34$ ns, (e) $\Delta\tau = 10$ ns, for $t_0 = 42$ ns and (f)$\Delta\tau = 17.4$ ns, for $t_0 = 70$ ns.

illustrated in figure 6.14(a), the delay time increases with Γ and its values vary from 9.2 to 12.4 ns. The resulting fractional delay of figure 6.14(b) increases with Γ. A maximum fractional delay of the order of 0.34 is measured for $\Gamma = 7.9$ cm^{-1}.

Now, we present the results of slowdown of nanosecond light pulses as a function of the input pulse durations. The results of figure 6.15 show that the light performances including, delay and input pulse duration increase with the pulse duration and the input laser power. From figure 6.15(a), we note that a maximum delay time $\Delta\tau = 25$ ns corresponding to a minimum group velocity $v_g = 400$ km/s is achieved for pulse duration $t_0 = 100$ ns and laser power $P_L = 200$ mW and $\Gamma = 6.9$ cm^{-1}. From figure 6.15(b), we note that the

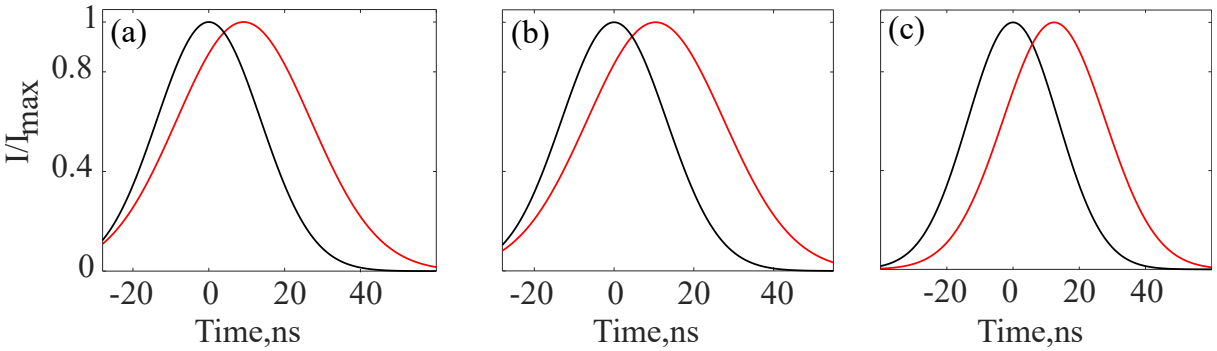

Figure 6.13: Temporal envelopes of the normalized input (black line) and output (red line) pulses as function of the time for input pulse duration $t_0 = 32\ ns$ for $\Gamma = 5.9\ cm^{-1}$, the delay is equal to 9.2 ns (a), $\Gamma = 7.4\ cm^{-1}$, the delay is equal to 10.4 ns (b) and $\Gamma = 7.9\ cm^{-1}$, the delay is equal to 12.4 ns (c).

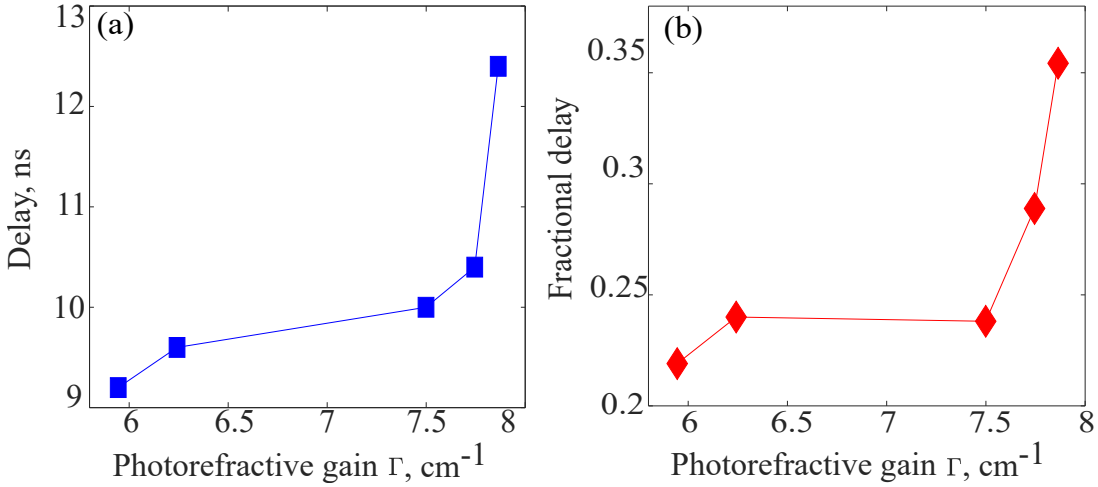

Figure 6.14: Performances of the slow light as a function of the photorefractive gain. (a), (b) and (c) are respectively: Time delay $\Delta\tau$, output pulse duration $t_{out(FHWM)}$ and fractional delay FD as a function of Γ.

output pulse broadening is less important for $P_L = 150\ mW$ for pulse duration $t_0 > 40\ ns$. It can be seen that despite the reduction of the output pulse widening, the delays remain small, which reduces the performance of the fractional delay. A maximum fractional delay value $FD = 0.29$ is measured for pulse width $t_0 = 16\ ns$ and $P_L = 200\ mW$ (figure 6.15(c)).

As we have seen above, when we change the input pulse duration, the pulse intensity changes and the gain changes as well. So the results of figure 6.15 are obtained for different input pulse durations and consequently for different values of the photorefractive gain.

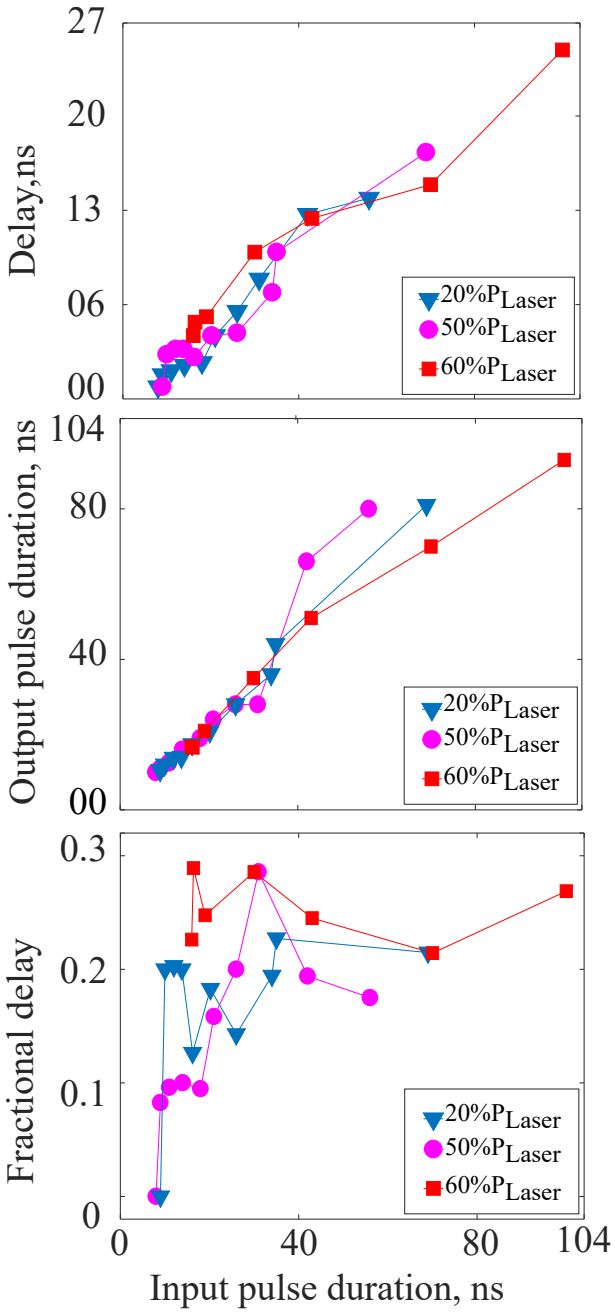

Figure 6.15: Performances of the slow dark pulses according to the input pulse duration t_0 for different input laser power. (a) Delay curve, (b) output pulse durations and (c) fractional delay. 20%,50%,60% P_{laser} correspond respectively to P_{laser} = 80,150, 200 mW

We, therefore, decide t_0 plot the same curves differently by keeping those pulse durations that correspond to approximately the same values of the PR gain. The results are shown in figure 6.16 for Γ of 6 cm^{-1}.

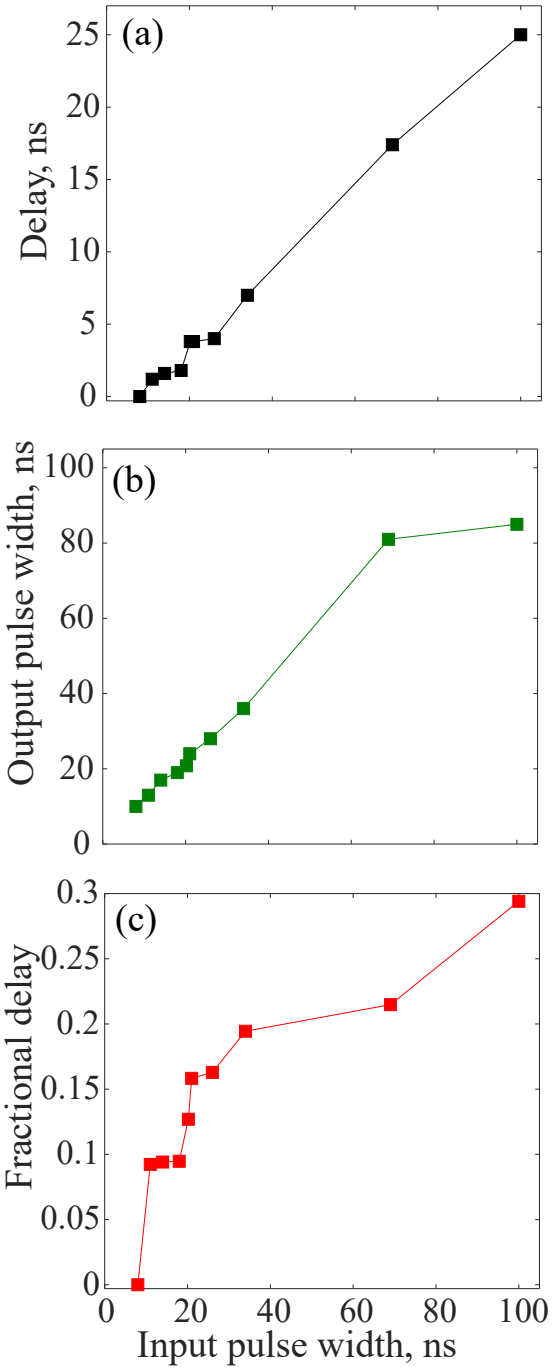

Figure 6.16: Performances of the slow dark pulses according to the input pulse duration t_0 for different input laser power. (a) Delay curve and (b) Fractional delay. 20%,50%,60% P_{laser} correspond respectively to P_{laser} = 80,150, 170 mW

6.4 Conclusion

To conclude, we proposed and experimentally demonstrated that the TWM in the nanosecond regime in the SPS photorefractive crystal can be used to slow down nanosecond pulses. First, we have given the PR conditions that allow us to have optical delays in the PR material. Indeed, we have theoretically shown that to slowdown ns light pulse, the response time of the PR crystal must be close to the pulse duration.

We then presented the setup of the two-wave mixing in the nanosecond regime. The photorefractive gain has been measured for different input pulse intensities, different grating period, different polarization of the pump and the probe pulses.

In the second part of the chapter, it is shown that SPS doped Sb can slowdown pulses in the range of 10 to 100 ns with respectively a delay which varies from 1.4 to 24 ns. The delay performances are similar to those reported in the optical fibers [2]. Using the stimulated Brillouin scattering process in a km-long optical fiber [2], they observe delay as large as 25 ns and fractional delay of 0.4 for a 63 ns pulse duration. In addition, and as in the case of the CW regime, we have shown that the slow light performances increase with the photorefractive gain and the input pulse duration.

7

Conclusions and perspectives

The research carried out during our thesis focused on theoretical and experimental studies of light deceleration based on different nonlinear processes such as the two-wave mixing or the beam fanning in photorefractive crystals. All the techniques applied in the work focus on the modification of the dispersion of the photorefractive crystal by changing the gain spectrum at room temperature. These studies have made it possible to improve the slow light performances obtained at wavelengths in the visible range and to develop new techniques that extend the performances in the infrared range.

We have started our thesis by giving the physical phenomena, allowing us to decelerate the light pulses in dispersive materials. In addition, we have presented some of the performance limitations of each method, the objectives of our work and why it focuses on the photorefractive slow light systems. We carried out a bibliographical study on the nonlinear photorefractive process. In particular, we have given the mechanisms at the origin of the slow light process and the different types of crystals that can be used to study the slow light.

The use of two-wave mixing in the visible range has allowed us to slowdown both bright and dark pulses. We have shown that the delay values vary with the duration of the pulse propagating through the crystal and the with photorefractive gain resulting from the TWM process. Furthermore, the optimization of the TWM configuration with bright pulses in the SPS crystal has allowed to reduce the group velocity down to 0.9 cm/s and to improve the fractional delay already reported in the literature by a factor of 2. On the other hand, the TWM between a dark pulse and a continuous beam allows us to get delays larger than the input pulse durations, i.e a result not reported yet in the system. Moreover, we have shown that the fractional delay can reach 1 for dark pulses with durations close to the crystal response time.

An alternative method simpler than the TWM has been also studied in this thesis based on photorefractive beam fanning. We have developed theoretical and experimental studies of the slow light, induced by this phenomenon in the visible and infrared range. We have obtained a simple expression of the output pulse intensity. This expression can be analytically solved, to calculate the optical delay and the fractional delay as a function of the input parameters. We have shown experimentally that the optical delay resulting from beam fanning is better for visible wavelengths where the depletion factor is larger.

Finally, we have demonstrated for the first time the slowing down of the nanosecond pulses

using the two-pulse mixing method. In the first part, the photorefractive gain has been measured according to several parameters such as the polarization, the grating period and the input intensity. The performances experimentally obtained from slow light were discussed at the end of the chapter.

7.0 Summary

Broadband performances

To summarize, the photorefractive crystal allows to slow down light pulses over a broadband range of wavelengths (from the visible to the infrared) using the TWM respectively at CW and nanosecond regime (figure 7.1). This is only possible if the pulse durations to be transmitted are of the order of the response time of the crystal.

Group velocity

For the same photorefractive crystal, we can generate a photorefractive gain at both visible and infrared wavelengths. The resulting gain can also increase the dispersion of the PR crystal and reduce the velocity of the output pulse. However, the corresponding group velocity (figure 7.1 (a)) is lower in the visible range ($v_g = 0.9\ cm/s$) compared to the one measured at nanosecond time scale ($v_g = 400\ km/s$) because the delay is important in the first case (figure 7.1 (b)). Therefore, for the nanosecond regime, the group velocity performances are limited both by the delay value and by the propagation distance d through the PR crystal.

Fractional delay

The performances of the fractional (figure 7.1 (c)) delay are better in the visible range because the photorefractive gain is twice as important in that case compared to the infrared wavelength. However, our FD performances ($FD = 0.3$) achieved with nanosecond pulses are similar to those achieved in the optical fibers [2]. Also, we note that the maximum of $FD = 0.8$ is measured for pulse durations close to the response time of the crystal. That situation is observed clearly for the visible range because the response time is almost independent of the input pulse width. However, in the case of the pulsed regime, the response time change with the pulse duration, hence the input pulse intensity, which

explains the behavior of the curve of FD (FD increase with increasing the input pulse duration).

Finally, to improve the performances of FD at the nanosecond regime and reach the maximum value achieved in the visible domain, it is important both to use a PR crystal with a nanosecond response time and a PR gain similar to the one obtained at the visible wavelength.

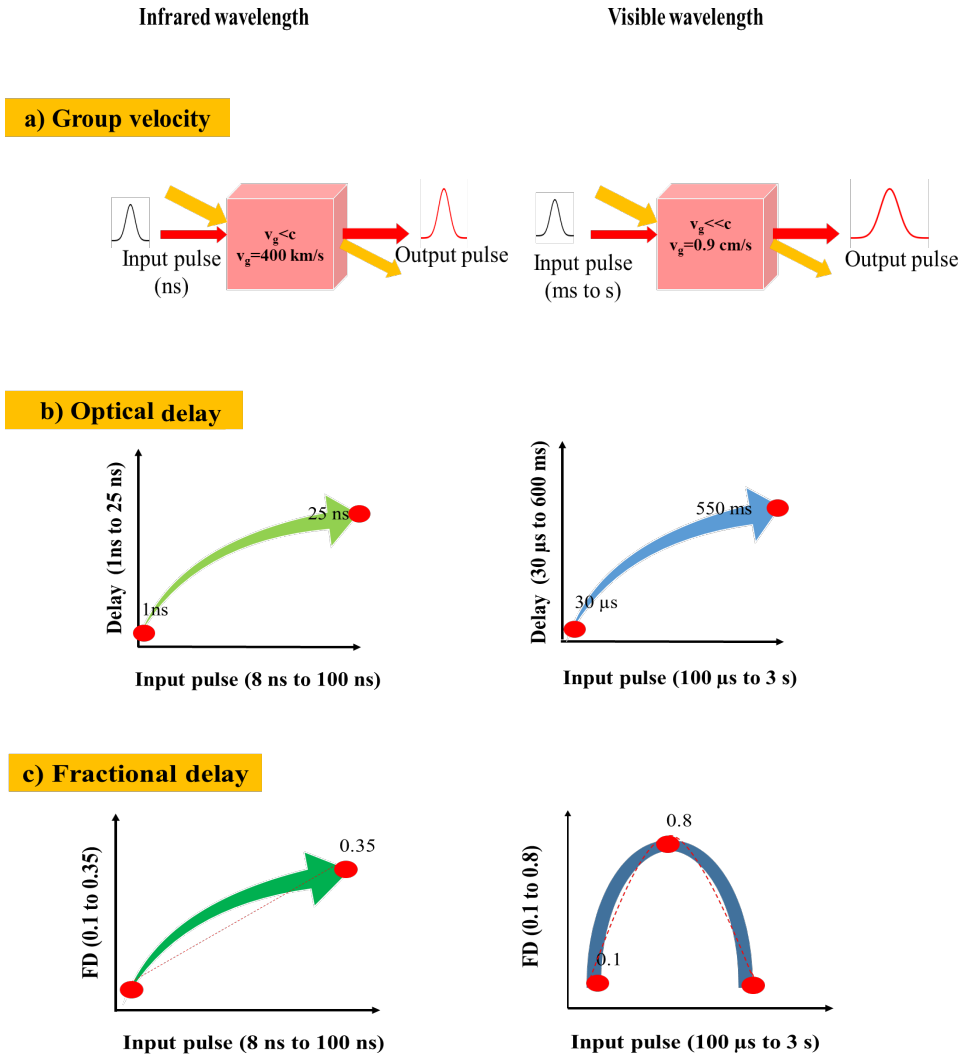

Figure 7.1: Summary of slow light performances at infrared and visible wavelengths using TWM respectively at CW and nanosecond regimes.

7.0 Perspectives

We are now in a position to consider several extensions to this thesis work. First, in order to investigate further the study of slowing down in the pulsed regime, it will be interesting to:

- develop the theory and an analytical model, enabling to discuss the physics of the TWM at the nanosecond regime and therefore to estimate the resulting optical delay. This model may be similar to the one developed by B.Sturman et al. [100]. This model allows calculating the output pulse intensity in the case where the pump is also a Gaussian pulse. Using this model, they estimate that the pulse velocity can vary from 10^{-4} to 10^{6} cm/s depending on the input light intensity and the input pulse duration. So, it is interesting to compare the behaviors of theoretical values to those obtained experimentally in this thesis and to examine the influence of the pump pulse duration on the optical delay.

- study the slow light with the photorefractive beam fanning at the pulsed regime and test other photorefractive crystals with fast response time like the PR semiconductors and $BaTiO_3$ crystal. This last one can be a good candidate for slowing down short pulses because it exhibits a photorefractive gain as large as 14 cm^{-1} in the nanosecond regime at 1.06 mm [152].

- study the dependence of the optical delay in that can be measured in a PR SPS crystal as a function of wavelengths. For this, it will be interesting to use a tunable laser such as an OPO (optical parametric oscillator) to analyze the tunability of the time delay over a wide range of wavelengths of telecommunication applications and the PR gain that can be generated in the crystal. This is important because the applications of slow light such as buffers require a degree of tunability. This study can be possible because of the large transparency window of the SPS crystal that can goes up to 8 μs [68].

Another perspective concerns the study of the phenomenon of slow photorefractive solitons at room temperature. Knowing that compared to the bright pulses, the photorefractive solitons have the ability to propagate without any deformation in a medium. Indeed, the use of the Bragg soliton in a periodic media [154] and in a fiber grating [103] allows the

slow light in these materials. It is reported in [103] that the soliton can propagate slowly in a fiber grating and without suffering from the output broadening. As shown in figure 7.2, the delay is tunable by varying the intensity and the mechanical strain on the grating for different detuning $\delta = 2\pi(\lambda^{-1} - \lambda_B^{-1})$ which is the normalized difference of the laser and the Bragg wavelengths λ and λ_B respectively.

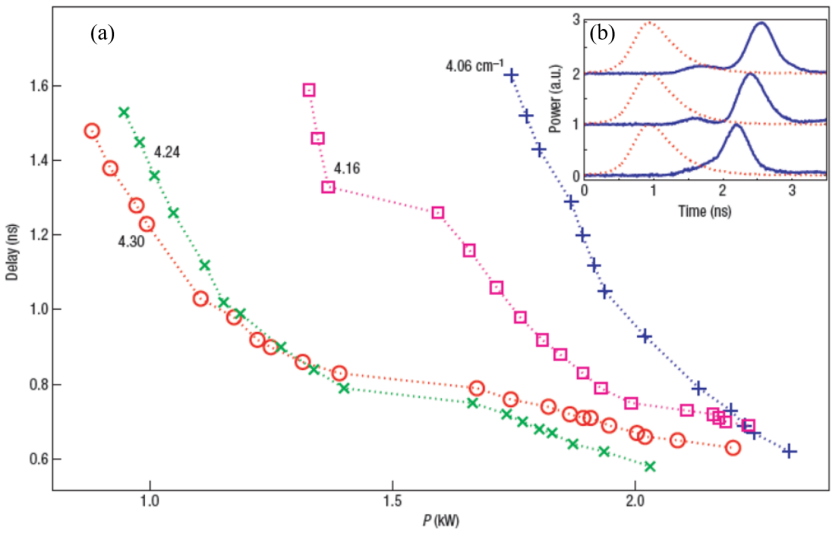

Figure 7.2: (a) Tunable delay of the transmitted pulses as a function of the input peak power P for the four values of detuning δ. (b) The input (Dotted lines) and the output (solid) solitons as a function of the time. Top: $\delta = 4.06\ cm^{-1}$ and $P = 1.75\ kW$. Middle: $\delta = 4.16\ cm^{-1}$ and $P = 1.35\ kW$. Bottom: $\delta = 4.24\ cm^{-1}$ and $P = 1.05\ kW$. The output pulse remains constant (of the order of 0.45 ns) when it propagates in the medium. [103].

So, the use of the temporal PR solitons may be interesting to limit the problem of output signal distortion and improve the fractional delay values already measured in photorefractive slow light systems.

8

Bibliography

1. Hau, L. V., Harris, S. E., Dutton, Z. & Behroozi, C. H. Light speed reduction to 17 metres per second in an ultracold atomic gas. *Nature* **397,** 594 (1999).
2. Okawachi, Y. *et al.* Tunable All-Optical Delays via Brillouin Slow Light in an Optical Fiber. *Phys. Rev. Lett.* **94,** 153902. `https://link.aps.org/doi/10.1103/PhysRevLett.94.153902` (15 Apr. 2005).
3. Baba, T., Kawasaki, T., Sasaki, H., Adachi, J. & Mori, D. Large delay-bandwidth product and tuning of slow light pulse in photonic crystal coupled waveguide. *Optics express* **16,** 9245–9253 (2008).
4. Podivilov, E., Sturman, B., Shumelyuk, A. & Odoulov, S. Light pulse slowing down up to 0.025 cm/s by photorefractive two-wave coupling. *Physical review letters* **91,** 083902 (2003).
5. Boller, K.-J., Imamoğlu, A. & Harris, S. E. Observation of electromagnetically induced transparency. *Physical Review Letters* **66,** 2593 (1991).
6. Harris, S. E., Yin, G., Kasapi, A., Jain, M. & Luo, Z. in *Coherence and Quantum Optics VII* 295–304 (Springer, 1996).
7. Dahan, D. & Eisenstein, G. Tunable all optical delay via slow and fast light propagation in a Raman assisted fiber optical parametric amplifier: a route to all optical buffering. *Optics Express* **13,** 6234–6249 (2005).
8. Residori, S., Bortolozzo, U. & Huignard, J. Slow and Fast Light in Liquid Crystal Light Valves. *Physical review letters* **100,** 203603 (May 2008).
9. Horn, W., v Bassewitz, J. & Denz, C. Slow and fast light in photorefractive SBN: 60. *Journal of Optics* **12,** 104011 (2010).
10. Mathey, P., Gadret, G. & Shcherbin, K. Slow light with photorefractive four-wave mixing. *Phys. Rev. A* **84,** 063802. `https://link.aps.org/doi/10.1103/PhysRevA.84.063802` (6 Dec. 2011).

11. Bouldja, N., Wolfersberger, D. & Sciamanna, M. *Ultraslow Light Pulse in a SPS Photorefractive Crystal at Room Temperature* in *2018 European Conference on Optical Communication (ECOC)* (2018), 1–3.

12. Bouldja, N., Sciamanna, M. & Wolfersberger, D. Improved slow light performances using photorefractive two-wave mixing. *Optics letters* **44,** 1496–1499 (2019).

13. Bouldja, N., Sciamanna, M. & Wolfersberger, D. *Slow light using photorefractive beam fanning* in *The European Conference on Lasers and Electro-Optics* (2019), cd_p_33.

14. Bouldja, N., Sciamanna, M. & Wolfersberger, D. Slow light with photorefractive beam fanning. *Optics Express* **28,** 5860–5865 (2020).

15. Bouldja, N., Sciamanna, M. & Wolfersberger, D. *Slow light using photorefractive nonlinear optics* in *Nonlinear Optics and its Applications 2020* **11358** (2020), 113580I.

16. Bouldja, N., Grabar, A., Sciamanna, M. & Wolfersberger, D. Slow light of dark pulses in a photorefractive crystal. *Phys. Rev. Research* **2,** 032022. `https://link.aps.org/doi/10.1103/PhysRevResearch.2.032022` (3 July 2020).

17. Chin, S. H. *Governing the speed of a light signal in optical fibers* tech. rep. (EPFL, 2009).

18. Shi, Z. *Fundamentals and applications of slow light* (University of Rochester, 2010).

19. Hamilton, W. R. *Researches respecting vibration, connected with the theory of light* in *Proc. Roy. Irish Acad* **1** (1839), 341–349.

20. Gehring, G. M., Boyd, R. W., Gaeta, A. L., Gauthier, D. J. & Willner, A. E. Fiber-based slow-light technologies. *Journal of Lightwave Technology* **26,** 3752–3762 (2008).

21. Boyd, R. W. Material slow light and structural slow light: similarities and differences for nonlinear optics. *JOSA B* **28,** A38–A44 (2011).

22. Harris, S. E., Field, J. E. & Kasapi, A. Dispersive properties of electromagnetically induced transparency. *Phys. Rev. A* **46,** R29–R32. `https://link.aps.org/doi/10.1103/PhysRevA.46.R29` (1 July 1992).

23. Boyd, R. W. Material slow light and structural slow light: similarities and differences for nonlinear optics

Invited

. *J. Opt. Soc. Am. B* **28,** A38–A44. http://josab.osa.org/abstract.cfm?URI=josab-28-12-A38 (Dec. 2011).

24. Baba, T. Slow light in photonic crystals. *Nature photonics* **2,** 465 (2008).

25. Li, J., White, T. P., O'Faolain, L., Gomez-Iglesias, A. & Krauss, T. F. Systematic design of flat band slow light in photonic crystal waveguides. *Optics express* **16,** 6227–6232 (2008).

26. Krauss, T. F. Slow light in photonic crystal waveguides. *Journal of Physics D: Applied Physics* **40,** 2666 (2007).

27. Zhang, Y., Fan, B., Yuan, P. & Ma, Z. Observation of slow light propagation in solid state material. **24,** 1688–1690 (Dec. 2004).

28. Herráez, M. G., Song, K. Y. & Thévenaz, L. Arbitrary-bandwidth Brillouin slow light in optical fibers. *Optics express* **14,** 1395–1400 (2006).

29. Sharping, J. E., Okawachi, Y. & Gaeta, A. L. Wide bandwidth slow light using a Raman fiber amplifier. *Optics Express* **13,** 6092–6098 (2005).

30. Harris, S. E., Field, J. E. & Imamo ğlu, A. Nonlinear optical processes using electromagnetically induced transparency. *Phys. Rev. Lett.* **64,** 1107–1110. https://link.aps.org/doi/10.1103/PhysRevLett.64.1107 (10 Mar. 1990).

31. Phillips, D. F., Fleischhauer, A., Mair, A., Walsworth, R. L. & Lukin, M. D. Storage of Light in Atomic Vapor. *Phys. Rev. Lett.* **86,** 783–786. https://link.aps.org/doi/10.1103/PhysRevLett.86.783 (5 Jan. 2001).

32. Turukhin, A. V. *et al.* Observation of Ultraslow and Stored Light Pulses in a Solid. *Phys. Rev. Lett.* **88,** 023602. https://link.aps.org/doi/10.1103/PhysRevLett.88.023602 (2 Dec. 2001).

33. Patnaik, A. K., Liang, J. Q. & Hakuta, K. Slow light propagation in a thin optical fiber via electromagnetically induced transparency. *Phys. Rev. A* **66,** 063808. https://link.aps.org/doi/10.1103/PhysRevA.66.063808 (6 Dec. 2002).

34. Scalora, M. *et al.* Ultrashort pulse propagation at the photonic band edge: Large tunable group delay with minimal distortion and loss. *Physical review. E, Statistical physics, plasmas, fluids, and related interdisciplinary topics* **54,** R1078–R1081 (Sept. 1996).

35. Yanik, M. & Fan, S. Dynamic Photonic Structures: Stopping, Storage, and Time Reversal of Light. *Studies in Applied Mathematics* **115,** 233–253 (Aug. 2005).

36. Yanik, M. & Fan, S. Stopping and storing light coherently. *Physical Review. A* **71** (Jan. 2005).

37. Wang, Y., Zhang, W., Huang, Y. & Peng, J. *SBS Slow Light in High Nonlinearity Photonic Crystal Fiber* in (Apr. 2007), 1–3. ISBN: 1-55752-831-4.

38. Settle, M. *et al.* Flatband slow light in photonic crystals featuring spatial pulse compression and terahertz bandwidth. *Optics express* **15,** 219–26 (Feb. 2007).

39. Okawachi, Y., Sharping, J. E., Xu, C. & Gaeta, A. L. Large tunable optical delays via self-phase modulation and dispersion. *Opt. Express* **14,** 12022–12027. http://www.opticsexpress.org/abstract.cfm?URI=oe-14-25-12022 (Dec. 2006).

40. Thévenaz, L. Slow and fast light in optical fibres. *Nature photonics* **2,** 474 (2008).

41. Song, K. Y., Herráez, M. G. & Thévenaz, L. Observation of pulse delaying and advancement in optical fibers using stimulated Brillouin scattering. *Optics Express* **13,** 82–88 (2005).

42. Boyd, R. Nonlinear Optics 2nd edn (Amsterdam: Academic) (2003).

43. Zhu, Z., Dawes, A. M. C., Gauthier, D. J., Zhang, L. & Willner, A. E. Broadband SBS Slow Light in an Optical Fiber. *J. Lightwave Technol.* **25,** 201–206. http://jlt.osa.org/abstract.cfm?URI=jlt-25-1-201 (Jan. 2007).

44. Thévenaz, L. Ralentir la lumière pour des transmissions plus rapides. *Bulletin des SEV VSE Including Jahresheft* **102,** 32 (2011).

45. Tucker, R. S., Pei-Cheng Ku & Chang-Hasnain, C. J. *Fundamental limitations of slow-light optical buffers* in *OFC/NFOEC Technical Digest. Optical Fiber Communication Conference, 2005.* **3** (Mar. 2005), 3 pp. Vol. 3-.

46. Boyd, R. W., Gauthier, D. J. & Gaeta, A. L. Applications of slow light in telecommunications. *Optics and Photonics News* **17,** 18–23 (2006).

47. Krauss, T. F. Why do we need slow light? *Nature Photonics* **2,** 448 (2008).

48. Hamachi, Y., Kubo, S. & Baba, T. Slow light with low dispersion and nonlinear enhancement in a lattice-shifted photonic crystal waveguide. *Opt. Lett.* **34,** 1072–1074. http://ol.osa.org/abstract.cfm?URI=ol-34-7-1072 (Apr. 2009).

49. Monat, C. *et al. Green light emission in silicon through slow light enhanced third-harmonic generation in photonic crystal waveguides* in *Conference on Lasers and Electro-Optics/International Quantum Electronics Conference* (Optical Society of America, 2009), JTuF5. http://www.osapublishing.org/abstract.cfm?URI=CLEO-2009-JTuF5.

50. Solntsev, A. *Frequency conversion in nonlinear optical waveguides: from classical to quantum applications* (Mar. 2015).

51. Lay, O. *et al.* MSTAR: a submicrometer absolute metrology system. *Optics Letters* **28,** 890–892 (2003).

52. Soljačić, M. *et al.* Photonic-crystal slow-light enhancement of nonlinear phase sensitivity. *JOSA B* **19,** 2052–2059 (2002).

53. Shi, Z. & Boyd, R. W. Slow-light interferometry: practical limitations to spectroscopic performance. *JOSA B* **25,** C136–C143 (2008).

54. Chamanzar, M., Momeni, B. & Adibi, A. Compact on-chip interferometers with high spectral sensitivity. *Optics letters* **34,** 220–222 (2009).

55. Shi, Z. & Boyd, R. W. *Slow-light enhanced spectrometers on chip* in *Photonics North 2011* **8007** (2011), 80071D.

56. Shi, Z., Boyd, R. W., Gauthier, D. J. & Dudley, C. C. Enhancing the spectral sensitivity of interferometers using slow-light media. *Opt. Lett.* **32,** 915–917. http://ol.osa.org/abstract.cfm?URI=ol-32-8-915 (Apr. 2007).

57. Shi, Z., Boyd, R. W., Camacho, R. M., Vudyasetu, P. K. & Howell, J. C. Slow-light Fourier transform interferometer. *Physical Review Letters* **99,** 240801 (2007).

58. Tucker, R. S., Ku, P.-C. & Chang-Hasnain, C. J. Delay-bandwidth product and storage density in slow-light optical buffers. *Electronics Letters* **41,** 208–209 (2005).

59. Ashkin, A. *et al.* Optically-induced refractive index inhomogeneities in LiNbO3 and LiTaO3. *Applied Physics Letters* **9,** 72–74 (1966).

60. Günter, P. Holography, coherent light amplification and optical phase conjugation with photorefractive materials. *Physics Reports* **93,** 199–299 (1982).

61. Yariv, A. Phase conjugate optics and real-time holography. *IEEE Journal of Quantum Electronics* **14,** 650–660 (1978).

62. Krätzig, E. & Buse, K. in *Infrared Holography for Optical Communications* 23–40 (Springer, 2003).

63. Buse, K. Light-induced charge transport processes in photorefractive crystals I: Models and experimental methods. *Applied Physics B: Lasers & Optics* **64** (1997).

64. Durant, C. Etude expérimentale de la propagation d'un faisceau fin dans les matériaux photoréfractifs: application à la limitation optique (2002).

65. Haertle, D. *et al.* Electro-optical properties of Sn2P2S6. *Optics Communications* **215,** 333–343 (2003).

66. Feinberg, J. & MacDonald, K. R. in *Photorefractive Materials and their applications II* 151–203 (Springer, 1989).

67. Kukhtarev, N., Markov, V., Odulov, S., Soskin, M. & Vinetskii, V. in *Landmark Papers On Photorefractive Nonlinear Optics* 37–48 (World Scientific, 1995).

68. Mosimann, R. *Photorefractive effects in Sn_2 P_2 S_6 at near bandgap and telecommunication wavelengths* PhD thesis (ETH Zurich, 2008).

69. Cronin-Golomb, M. & Klein, M. Photorefractive Materials and Devices. *Handbook of Optics/ed. by M. Bass,* 39–1 (1995).

70. Günter, P., Huignard, J.-P. & Glass, A. M. *Photorefractive materials and their applications* (Springer, 1988).

71. West, D. *Physics of photorefraction in polymers* (CRC press, 2004).

72. Meerholz, K., Volodin, B., Kippelen, B., Peyghambarian, N., *et al.* A photorefractive polymer with high optical gain and diffraction efficiency near 100%. *Nature* **371,** 497–500 (1994).

73. Rudenko, E. & Sukhov, A. Photoinduced electrical conductivity and photorefraction in a nematic liquid crystal. *JETP Letters* **59,** 142–146 (1994).

74. Fisher, R. A. *Optical phase conjugation* (Academic Press, 2012).

75. Yariv, A. & Yeh, P. *Optical waves in crystals* (Wiley New York, 1984).

76. Feinberg, J. Phase conjugation with photorefractive materials. *Optics and Photonics News* **1,** 30–33 (1990).

77. Kogelnik, H. BSTJ briefs: Holographic image projection through inhomogeneous media. *The Bell System Technical Journal* **44,** 2451–2455 (1965).

78. Joseph, J., Pillai, P. & Singh, K. High-gain, low-noise signal beam amplification in photorefractive BaTiO 3. *Applied optics* **30,** 3315–3318 (1991).

79. Fainman, Y., Klancnik, E. & Lee, S. H. Optimal coherent image amplification by two-wave coupling in photorefractive BaTiO3. *Optical Engineering* **25,** 252228 (1986).

80. Picoli, G., Gravey, P., Ozkul, C. & Vieux, V. Theory of two-wave mixing gain enhancement in photorefractive InP: Fe: A new mechanism of resonance. *Journal of Applied Physics* **66,** 3798–3813 (1989).

81. Mosimann, R. *et al.* High-speed photorefraction at telecommunication wavelength 1.55 μm in Sn 2 P 2 S 6: Te. *Optics letters* **32,** 3230–3232 (2007).

82. Solymar, L., Webb, D. J. & Grunnet-Jepsen, A. *The physics and applications of photorefractive materials* (Clarendon Press, 1996).

83. Vazquez, R. A., Neurgaonkar, R. R. & Ewbank, M. D. Photorefractive properties of SBN:60 systematically doped with rhodium. *J. Opt. Soc. Am. B* **9,** 1416–1427. `http://josab.osa.org/abstract.cfm?URI=josab-9-8-1416` (Aug. 1992).

84. Odoulov, S. G. *et al.* Photorefraction in tin hypothiodiphosphate in the near infrared. *JOSA B* **13,** 2352–2360 (1996).

85. Bach, T. *et al.* Tailoring of infrared photorefractive properties of Sn 2 P 2 S 6 crystals by Te and Sb doping. *JOSA B* **24,** 1535–1541 (2007).

86. Kedyk, I. V. *et al.* Investigation of the dielectric, optical and photorefractive properties of Sb-doped Sn 2 P 2 S 6 crystals. *Applied Physics B* **92,** 549–554 (2008).

87. Grabar, A. A. *et al.* in *Photorefractive Materials and Their Applications 2* 327–362 (Springer, 2007).

88. Grabar, A., Muzhikash, R., Kostyuk, A. & Vysochanskii, Y. M. Investigation of the switching processes in the domain structure of ferroelectric Sn2P2S6 by the dynamic holography method. *Soviet physics. Solid state* **33,** 1314–1316 (1991).

89. Carpentier, C. & Nitsche, R. Vapour growth and crystal data of the thio (seleno)-hypodiphosphates Sn2P2S6, Sn2P2Se6, Pb2P2Se6 and their mixed crystals. *Materials Research Bulletin* **9,** 401–410 (1974).

90. Farahi, S. *Méthodes holographiques et spectroscopiques appliquées à l'imagerie acousto-optique de milieux diffusants épais* PhD thesis (2011).

91. Haertle, D., Guarino, A., Hajfler, J., Montemezzani, G. & Günter, P. Refractive indices of Sn 2 P 2 S 6 at visible and infrared wavelengths. *Optics Express* **13,** 2047–2057 (2005).

92. Odoulov, S. G., Shumelyuk, A. N., Brost, G. A. & Magde, K. M. Enhancement of beam coupling in the near infrared for tin hypothiodiphosphate. *Applied physics letters* **69,** 3665–3667 (1996).

93. Sturman, B., Mathey, P. & Jauslin, H.-R. Slowdown and speedup of light pulses using the self-compensating photorefractive response. *JOSA B* **28,** 347–351 (2011).

94. Shumelyuk, A. & Odoulov, S. Light pulse manipulation in Sn2P2S6. *Journal of Optics* **12,** 104015 (2010).

95. Shumelyuk, A. *et al.* Slowing down of light in photorefractive crystals with beam intensity coupling reduced to zero. *Physical review letters* **93,** 243604 (2004).

96. Shcherbin, K., Gadret, G., Jauslin, H. R., Kamshilin, A. & Mathey, P. Slowing down of light pulses using backward-wave four-wave mixing with local response. *J. Opt. Soc. Am. B* **32,** 2536–2547. `http://josab.osa.org/abstract.cfm?URI=josab-32-12-2536` (Dec. 2015).

97. Horn, W., Bassewitz, J. & Denz, C. Slow- and Fast Light in Photorefractive SBN:60. *JOURNAL OF OPTICS J. Opt* **20318,** 104011–4 (Oct. 2010).

98. Zhang, G., Dong, R., Bo, F. & Xu, J. Slowdown of group velocity of light by means of phase coupling in photorefractive two-wave mixing. *Applied optics* **43,** 1167–1173 (2004).

99. Deng, Z. *et al.* Time-bandwidth problem in room temperature slow light. *Physical review letters* **96,** 023602 (2006).

100. Sturman, B., Podivilov, E. & Gorkunov, M. Photorefractive deceleration of light pulses. *Journal of Experimental and Theoretical Physics* **106,** 668–677 (Apr. 2008).

101. Sturman, B., Podivilov, E. & Gorkunov, M. Photorefractive manipulation of light pulses. *Physical Review A* **77,** 063808 (2008).

102. Shumelyuk, A. & Odoulov, S. Light pulse manipulation in Sn2P2S6. *Journal of Optics* **12,** 104015 (Sept. 2010).

103. Mok, J., Sterke, C., Littler, I. & Eggleton, B. Dispersionless slow light using gap solitons. *Nature Physics* **2,** 775–780 (Oct. 2006).

104. Kivshar, Y. S. & Luther-Davies, B. Dark optical solitons: physics and applications. *Phys. Rep.* **298,** 81–197 (1998).

105. Krökel, D., Halas, N. J., Giuliani, G. & Grischkowsky, D. Dark-pulse propagation in optical fibers. *Phys. Rev. Lett.* **60,** 29 (1988).

106. Cao, W.-h., Li, S. & Chan, K.-t. Generation of dark pulse trains from continuous-wave light using cross-phase modulation in optical fibers. *Appl. Phys. Lett.* **74,** 510–512 (1999).

107. Emplit, P., Hamaide, J.-P., Reynaud, F., Froehly, C. & Barthelemy, A. Picosecond steps and dark pulses through nonlinear single mode fibers. *Optics communications* **62,** 374–379 (1987).

108. Weiner, A. *et al.* Experimental observation of the fundamental dark soliton in optical fibers. *Physical review letters* **61,** 2445 (1988).

109. Emplit, P., Haelterman, M., Kashyap, R. & De Lathouwer, M. Fiber Bragg grating for optical dark soliton generation. *IEEE Photonics Technology Letters* **9,** 1122–1124 (1997).

110. Weiner, A. *et al.* Temporal and spectral self-shifts of dark optical solitons. *Optics letters* **14,** 868–870 (1989).

111. Zimmermann, J. *et al.* Dark pulse formation in a quantum-dot laser. *Applied Physics Letters* **79,** 18–20 (2001).

112. Zhao, W. & Bourkoff, E. Generation, propagation, and amplification of dark solitons. *JOSA B* **9,** 1134–1144 (1992).

113. Nakazawa, M. & Suzuki, K. Generation of a pseudorandom dark soliton data train and its coherent detection by one-bit-shifting with a Mach-Zehnder interferometer. *Electronics Letters* **31,** 1084–1085 (1995).

114. Okhotnikov, O. & Araujo, F. Pulse generation through optical switching in phase driven loop mirror. *Electronics Letters* **31,** 2197–2198 (1995).

115. Zhao, W. & Bourkoff, E. Generation of dark solitons under a cw background using waveguide electro-optic modulators. *Optics letters* **15,** 405–407 (1990).

116. Frantzeskakis, D. Dark solitons in atomic Bose–Einstein condensates: from theory to experiments. *J. Phys. A: Math. Theor.* **43,** 213001 (2010).

117. Schoenlein, R. *et al.* Generation of femtosecond pulses of synchrotron radiation. *J. Sci.* **287,** 2237–2240 (2000).

118. Meshulach, D. & Silberberg, Y. Coherent quantum control of two-photon transitions by a femtosecond laser pulse. *Nature* **396,** 239 (1998).

119. Xue, X. *et al.* Mode-locked dark pulse Kerr combs in normal-dispersion microresonators. *Nat. Photonics* **9,** 594 (2015).

120. Farina, D. & Bulanov, S. Slow electromagnetic solitons in electron-ion plasmas. *Plasma Phys. Rep.* **27,** 641–651 (2001).

121. Fitrakis, E., Kamalakis, T. & Sphicopoulos, T. Slow-light dark solitons in insulator–insulator–metal plasmonic waveguides. *J. Opt. Soc. Am. B* **27,** 1701–1706 (2010).

122. Tsuzuki, T. Nonlinear waves in the Pitaevskii-Gross equation. *Journal of Low Temperature Physics* **4,** 441–457 (1971).

123. Hasegawa, A. & Tappert, F. Transmission of stationary nonlinear optical pulses in dispersive dielectric fibers. I. Anomalous dispersion. *Applied Physics Letters* **23,** 142–144 (1973).

124. Kamchatnov, A., Kraenkel, R. A. & Umarov, B. Asymptotic soliton train solutions of the defocusing nonlinear Schrödinger equation. *Physical Review E* **66,** 036609 (2002).

125. Emplit, P., Haelterman, M. & Hamaide, J.-P. Picosecond dark soliton over a 1-km fiber at 850 nm. *Optics letters* **18,** 1047–1049 (1993).

126. Residori, S., Ramazza, P. & Zhao, M. Dynamics of beam fanning in Cu-doped KNSBN. *Optics communications* **102,** 100–104 (1993).

127. Grabar, A., Mathey, P. & Gadret, G. Manipulation of fast light using photorefractive beam fanning. *JOSA B* **31,** 980–986 (2014).

128. Feinberg, J. Asymmetric self-defocusing of an optical beam from the photorefractive effect. *JOSA* **72,** 46–51 (1982).

129. Magnusson, R. & Gaylord, T. K. Laser Scattering Induced Holograms in Lithium Niobate. *Appl. Opt.* **13,** 1545–1548. `http://ao.osa.org/abstract.cfm?URI=ao-13-7-1545_1` (July ts).

130. Voronov, V. V., Dorosh, I., Kuz'minov, Y. S. & Tkachenko, N. in *Landmark Papers On Photorefractive Nonlinear Optics* 79–82 (World Scientific, 1995).

131. Temple, D. A. & Warde, C. Anisotropic scattering in photorefractive crystals. *J. Opt. Soc. Am. B* **3,** 337–341. `http://josab.osa.org/abstract.cfm?URI=josab-3-2-337` (Feb. ts).

132. Segev, M., Ophir, Y. & Fischer, B. Nonlinear multi two-wave mixing, the fanning process and its bleaching in photorefractive media. *Optics Communications* **77,** 265–274 (1990).

133. Pati, G., Tripathi, R. & Singh, K. Intensity-dependent beam-fanning in high-gain photorefractive barium titanate crystal. *Journal of Modern Optics* **48,** 1791–1801 (2001).

134. Hong, Y.-H. *et al.* Fanning effects in photorefractive crystals. *Optics letters* **18,** 772–774 (1993).

135. Segev, M., Engin, D., Yariv, A. & Valley, G. C. Temporal evolution of fanning in photorefractive materials. *Optics letters* **18,** 956–958 (1993).

136. Montemezzani, G. *et al.* Origin of the lobe structure in photorefractive beam fanning. *Physical Review A* **52,** 1791 (1995).

137. Zhang, G. *et al. Study of resistance against photorefractive light-induced scattering in LiNbO3: Fe, Mg crystals* in *Photorefractive Fiber and Crystal Devices: Materials, Optical Properties, and Applications* **2529** (1995), 14–17.

138. Grabar, A., Gurzan, M., Kedyk, I., Stoika, I. & Vysochanskii, Y. M. Optical properties and applications of photorefractive Sn2P2S6. *Ferroelectrics* **257,** 245–254 (2001).

139. Miller, M., Wood, G. & Salamo, G. Photorefractive beam fanning optical limiter. *MRS Online Proceedings Library Archive* **479** (1997).

140. Rehn, H., Kowarschik, R. & Ringhofer, K. H. Beam-fanning novelty filter with enhanced dynamic phase resolution. *Applied optics* **34,** 4907–4911 (1995).

141. Salamo, G., Miller, M. J., Clark III, W. W., Wood, G. L. & Sharp, E. J. Strontium barium niobate as a self-pumped phase conjugator. *Optics communications* **59,** 417–422 (1986).

142. Zhang, J., Wang, H., Yoshikado, S. & Aruga, T. Incoherent-to-coherent conversion by use of the photorefractive fanning effect. *Optics letters* **22,** 1612–1614 (1997).

143. Cronin-Golomb, M. & Yariv, A. Optical limiters using photorefractive nonlinearities. *Journal of applied physics* **57,** 4906–4910 (1985).

144. Anderson, D. Z. & Feinberg, J. Optical novelty filters. *IEEE Journal of Quantum Electronics* **25,** 635–647 (1989).

145. Cronin-Golomb, M., Biernacki, A. M., Lin, C. & Kong, H. Photorefractive time differentiation of coherent optical images. *Optics letters* **12,** 1029–1031 (1987).

146. Smirl, A. L. *et al.* Picosecond photorefractive effect in BaTiO 3. *Optics letters* **12,** 501–503 (1987).

147. She, W., Wu, Q., Li, Q., Yu, Z. & Mo, D. Picosecond light pulse shaping in photorefractive crystal by two-wave coupling. *Optics communications* **101,** 65–68 (1993).

148. Huot, N., Jonathan, J., Pauliat, G., Rytz, D. & Roosen, G. Characterization of a photorefractive rhodium doped barium titanate at 1.06 μm. *Optics communications* **135,** 133–137 (1997).

149. Valley, G. C., Dubard, J., Smirl, A. L. & Glass, A. M. Picosecond photorefractive response of GaAs: EL2, InP: FE, and CdTe: V. *Optics letters* **14,** 961–963 (1989).

150. Petrovic, M. S., Suchocki, A., Powell, R. C., Valley, G. C. & Cantwell, G. Picosecond two-beam coupling and polarization rotation by scalar gratings in undoped cadmium telluride at 1.064 μm. *Physical Review B* **43,** 2228 (1991).

151. Horowitz, M., Fischer, B., Barad, Y. & Silberberg, Y. Photorefractive effect in a BaTiO 3 crystal at the 1.5-μm wavelength regime by two-photon absorption. *Optics letters* **21,** 1120–1122 (1996).

152. Huot, N., Jonathan, J., Roosen, G. & Rytz, D. Two-wave mixing in photorefractive BaTiO 3: Rh at 1.06 μm in the nanosecond regime. *Optics letters* **22,** 976–978 (1997).

153. Von Bally, G., Rickermann, F., Odoulov, S. & Shumelyuk, A. Near-infrared holographic recording in Sn2P2S6 with nanosecond pulses. *physica status solidi (a)* **157,** 199–204 (1996).

154. Christodoulides, D. N. & Joseph, R. I. Slow Bragg solitons in nonlinear periodic structures. *Phys. Rev. Lett.* **62,** 1746–1749. `https://link.aps.org/doi/10.1103/PhysRevLett.62.1746` (15 Apr. 1989).